Single Chip Dynamic Nuclear Polarization Microsystems

Nergiz SAHIN SOLMAZ

École
polytechnique
fédérale
de Lausanne

2023

Hayatta en hakiki mürşit ilimdir, fendir.
M.K. Atatürk

to Cem

Abstract

Nuclear magnetic resonance (NMR) methods are powerful tools employed in many fields, including physics, chemistry, material science, biology, and medicine. The use of NMR methodologies in an even wider range of applications is often hindered by the relatively large number of resonating spins needed to achieve a sufficiently large signal-to-noise ratio (SNR) in the available experimental time. An efficient approach to increase the SNR is hyperpolarization where the nuclear spin polarization is increased, e.g., by microwave, optical, and chemistry-based methodologies.

Dynamic nuclear polarization (DNP) is one of the most powerful and versatile hyperpolarization methods. Microwave DNP employs a microwave magnetic field to excite the unpaired electrons in the sample under investigation into electron spin resonance (ESR). The ESR excitation of the electrons increases the polarization of the nearby nuclear spins well above the thermal equilibrium value, producing an increase in the SNR up to 660 for ^{1}H nuclei. A major drawback of DNP is the cost and complexity of the required microwave hardware, especially at high magnetic fields and low temperatures. To overcome this drawback and with the focus on the study of nanoliter and subnanoliter samples, this thesis demonstrates single chip DNP microsystems where the microwave excitation and detection are performed locally on chip without the need of external microwave generators and transmission lines.

During the last two decades, the separate integration on a single chip of the front-end electronics of NMR and ESR spectrometers has been demonstrated. In this thesis, the co-integration on a single chip of the front-end electronics of NMR and ESR detectors is presented for the first time. This combination of sensors allows to perform DNP experiments using a single chip having an area of about 2 mm^2.

Firstly, a DNP microsystem operating at 10.7 GHz(ESR)/16 MHz(NMR) is integrated into a single CMOS chip. The ESR detector is an oscillator that generates microwave magnetic fields B_{1e} up to 70 μT. The NMR detector is a broadband transceiver operating up to 1 GHz. ^{1}H DNP-enhanced NMR experiments on liquid and solid samples having a volume of about 1 nL are performed. Overhauser enhancements up to 50 are achieved on TEMPOL/H$_2$O solutions and solid effect enhancements up to 20 are achieved on BDPA:SEBS at room temperature.

Secondly, a DNP microsystem operating at 200 GHz(ESR)/300 MHz(NMR) is integrated into a

Abstract

single SiGe:BiCMOS chip. The ESR detector is a voltage controlled oscillator (VCO) operating at 200 GHz with a tuning range of 8 GHz which generates a B_{1e} up to a few G. The NMR detector is a broadband receiver operating up to 1 GHz. [1]H DNP experiments on BDPA:PS samples having a volume of 2 nL and 125 pL show solid effect enhancements up to 50 and 10 at 15 K and 100 K, respectively. A single chip DNP array is also demonstrated. The array has four frequency locked 200 GHz VCOs which interrogates a sample volume an order of magnitude larger compared to the single VCO. Measurements on BDPA:PS samples having a volume of 1 nL show solid effect enhancements up to 20 at 200 K.

Finally, a $In_{0.7}Ga_{0.3}As$ high electron mobility transistor (HEMT) technology is investigated for the possible integration of low power single chip DNP microsystems that might be able to operate down to 1 K and below. HEMT transistors and ultra low power oscillators operating at 11 GHz and 35 GHz are investigated down to 1.4 K.

Keywords: Dynamic nuclear polarization, DNP, nuclear magnetic resonance, NMR, electron spin resonance, ESR, magnetic resonance spectroscopy, LC oscillator, voltage controlled oscillator, VCO, receiver, transceiver, CMOS, SiGe, BiCMOS, HEMT, microwave, cryogenic, low power.

Résumé

Les méthodes de résonance magnétique nucléaire (RMN) sont des outils puissants utilisés dans de nombreux domaines, notamment la physique, la chimie, la science des matériaux, la biologie et la médecine. L'utilisation de l'RMN dans une gamme encore plus large d'applications est souvent entravée par le nombre relativement important de spins résonnants nécessaires pour obtenir un rapport signal/bruit (RSB) suffisamment élevé dans le temps expérimental disponible. Une approche efficace pour augmenter le RSB est l'hyperpolarisation, où la polarisation de spin nucléaire est augmentée, par exemple par des méthodologies basées sur les micro-ondes, l'optique et la chimie.

La polarisation dynamique nucléaire (PDN) est l'une des méthodes d'hyperpolarisation les plus puissantes et versatile. La PDN micro-ondes utilise un champ magnétique micro-ondes pour exciter les électrons non appariés de l'échantillon étudié en résonance de spin électronique (RSE). L'excitation RSE des électrons augmente la polarisation des spins nucléaires proches bien au-delà de la valeur d'équilibre thermique, produisant une augmentation du RSB jusqu'à 660 pour les noyaux ^{1}H. L'un des principaux inconvénients de la PDN est le coût et la complexité de l'instrumentation micro-ondes nécessaire, en particulier à des champs magnétiques élevés et à des températures basses. Pour surmonter cet inconvénient et en se concentrant sur l'étude d'échantillons nanolitres et subnanolitres, cette thèse démontre des microsystèmes PDN à puce unique où l'excitation et la détection des micro-ondes sont effectuées localement sur la puce sans avoir besoin de générateurs de micro-ondes externes et de lignes de transmission.

Au cours des deux dernières décennies, l'intégration séparée sur une seule puce de l'électronique frontale des spectromètres RMN et RSE a été démontrée. Dans cette thèse, la co-intégration sur une seule puce de l'électronique frontale des détecteurs RMN et RSE est présentée pour la première fois. Cette combinaison de capteurs permet de réaliser des expériences PDN en utilisant une seule puce d'une surface d'environ 2 mm^2.

Tout d'abord, un microsystème PDN fonctionnant à 10,7 GHz (RSE) / 16 MHz (RMN) est intégré dans une seule puce CMOS. Le détecteur RSE est un oscillateur qui génère des champs magnétiques micro-ondes B_{1e} jusqu'à 70 μT. Le détecteur RMN est un émetteur-récepteur à large bande fonctionnant jusqu'à 1 GHz. Des expériences ^{1}H RMN améliorée par le PDN sont réalisées sur des échantillons liquides et solides ayant un volume d'environ 1 nL. Des

Résumé

améliorations par effet Overhauser allant jusqu'à 50 sont obtenues sur TEMPOL/H_2O et des améliorations par effet solide allant jusqu'à 20 sont obtenues sur BDPA :SEBS à température ambiante.

Deuxièmement, un microsystème PDN fonctionnant à 200 GHz (RSE)/300 MHz (RMN) est intégré dans une seule puce SiGe :BiCMOS. Le détecteur RSE est un oscillateur commandé en tension (VCO) fonctionnant à 200 GHz accordable jusqu'à 8 GHz qui génère un B_{1e} jusqu'à quelques G. Le détecteur RMN est un récepteur à large bande fonctionnant jusqu'à 1 GHz. Des expériences ^{1}H RMN-PDN sur des échantillons de BDPA :PS ayant un volume de 2 nL et 125 pL montrent des améliorations par effet solide jusqu'à 50 et 10 à 15 K et 100 K, respectivement. Un réseau PDN à puce unique est également présenté. Le réseau comporte quatre VCO de 200 GHz verrouillés en fréquence qui interrogent un volume d'échantillon d'un ordre de grandeur supérieur à celui d'un seul VCO. Des mesures effectuées sur des échantillons de BDPA :PS d'un volume de 1 nL montrent des améliorations par effet solide allant jusqu'à 20 à 200 K.

Enfin, une technologie de transistor à haute mobilité électronique (HEMT) $In_{0.7}Ga_{0.3}As$ est étudiée pour l'intégration éventuelle de microsystèmes PDN à puce unique de faible puissance qui pourraient fonctionner jusqu'à 1 K et moins. Des transistors HEMT et des oscillateurs à très faible puissance fonctionnant à 11 GHz et 35 GHz sont étudiés jusqu'à 1.4 K.

Mots-clés : Polarisation dynamique nucléaire, PDN, résonance magnétique nucléaire, RMN, résonance de spin électronique, RSE, spectroscopie par résonance magnétique, LC oscillateur, oscillateur commandé en tension, VCO, récepteur, émetteur-récepteur, CMOS, SiGe, BiCMOS, HEMT, micro-ondes, cryogénique, efaible consommation de puissance.

Contents

Contents

List of Figures

List of Tables

1 Introduction

1.1 Importance of dynamic nuclear polarization

The nature of electrons and nuclei which causes them to interact with their surroundings provides a very rich spectroscopic information. Harvesting this knowledge by magnetic resonance (MR) has attracted a growing interest and supplied a great advantage to many research area in the last century. Due to the high versatility of nuclear magnetic resonance (NMR), methods developed according to its principles are powerful and non-invasive tools employed in many research fields including physics, chemistry, material science, biology, and medicine. Pioneering research in NMR has been recognized with five Nobel prizes. In 1944 and 1953 given to Rabi, Purcell and Bloch in physics, in 1991 and 2002 given to Ernst and Wütrich in chemistry and lastly in 2003 given to Mansfield and Lauterbur in medicine.

Applications of NMR span from structural information of chemical compounds to material properties research [3], analyzing protein structure, interaction and dynamics at atomic level [4], drug discovery [5], to medical imaging affecting millions of people today [6]. The use of NMR methodologies for an even wider range of studies is often hindered by the low signal-to-noise ratio (SNR) achievable in the available experimental time. This low sensitivity problem has led to development of several signal enhancement methods which is gathered under the term of hyperpolarization. In Fig. 1.1 polarization of ^{1}H, ^{13}C and electron spins are shown at 7 T and 300 K. The figure illustrates the inherently low sensitivity of NMR by showing the low polarization of the nuclear spins (25 ppm at 7 T and 300 K for ^{1}H nuclei) compared to electron spins (1.6% at 7 T and 300 K) and the possibility to hyperpolarize the nuclear spins to the level of the electron spins.

The development of hyperpolarization methods, which allows for signal enhancement of several orders of magnitude, has been a growing research field since the discovery of NMR. Several different techniques have been proposed for hyperpolarization which utilizes the power of different subjects that span from chemistry and optics to microwaves engineering [7]. One of these hyperpolarization methods is dynamic nuclear polarization (DNP) where the polarization of electrons is transfered to the nuclei. While most of the hyperpolarization
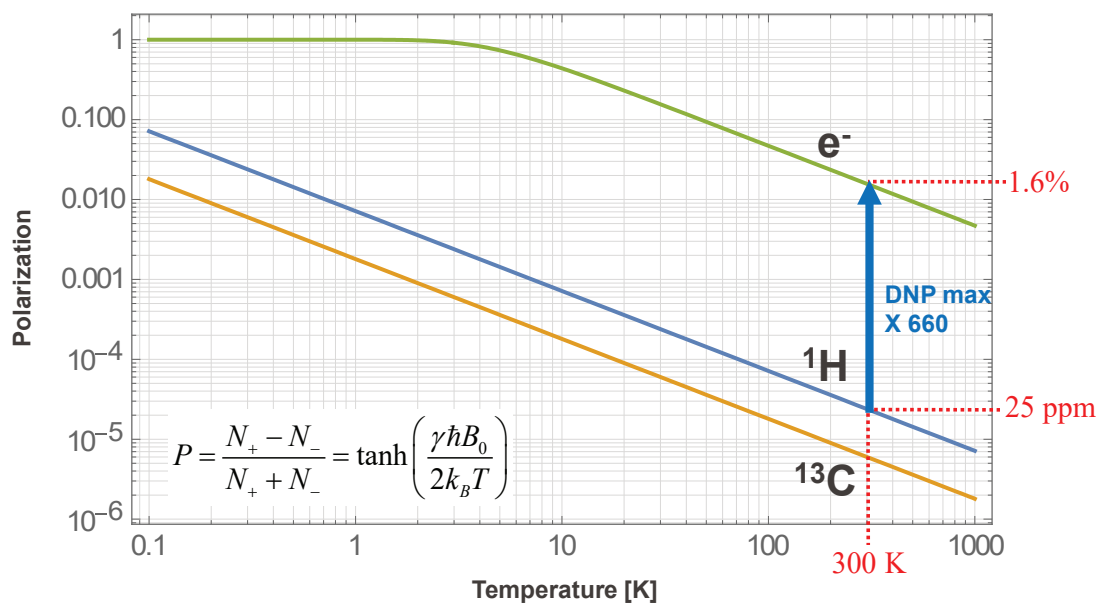
Figure 1.1: **Spin polarization at 7 T.** It is calculated as in the equation given on the left bottom corner of the figure. Spin polarization at 7 T and 300 K for ^{1}H and electron is 25 ppm and 1.6%, respectively. Increasing spin polarization of ^{1}H to the level of electron would result in maximum DNP enhancement of 660.

techniques are limited to a small class of molecules, DNP requires only unpaired electrons (added or, rarely, naturally present) in the sample which enables broad range of applications [8]. A microwave magnetic field is necessary to excite the electrons, which eventually allows for the transfer of electron polarization to the nearby nuclei. As a result, the NMR signal is enhanced up to the level of the ratio of the two gyromagnetic ratios of electron and the affected nuclei (see Fig. 1.2 for the graphical illustration of the DNP technique). The maximum enhancement is $\varepsilon = \gamma_e / \gamma_{^1H} = 660$ for ^{1}H nuclei. The measurement time is reduced by the square of the signal enhancement, which amplifies the effect of DNP. The increase of SNR by a factor of 10 reduces the measurement time by a factor of 100, e.g. an NMR measurement of 24 hours would take less than 15 minutes by the DNP enhancement. This sensitivity enhancement by DNP enables NMR spectroscopy experiments that are otherwise not feasible. The study of biological solids including peptides, nanocrystals and membrane proteins are not possible using solid state NMR alone [9].

Excitation of electrons through microwave magnetic field results in electron spin resonance (ESR), which is another magnetic resonance spectroscopy tool that provides rich information about the interaction of electrons with their surroundings. ESR spectroscopy provides useful information about distances between paramagnetic centers in enzymes, the dynamics of proteins, oxygen concentration in tissues and helps to measure the radiation absorbed in certain materials. It is chosen to understand pathological conditions related to existing free-radicals in vivo. ESR studies of materials such as single crystals and polymers give detailed
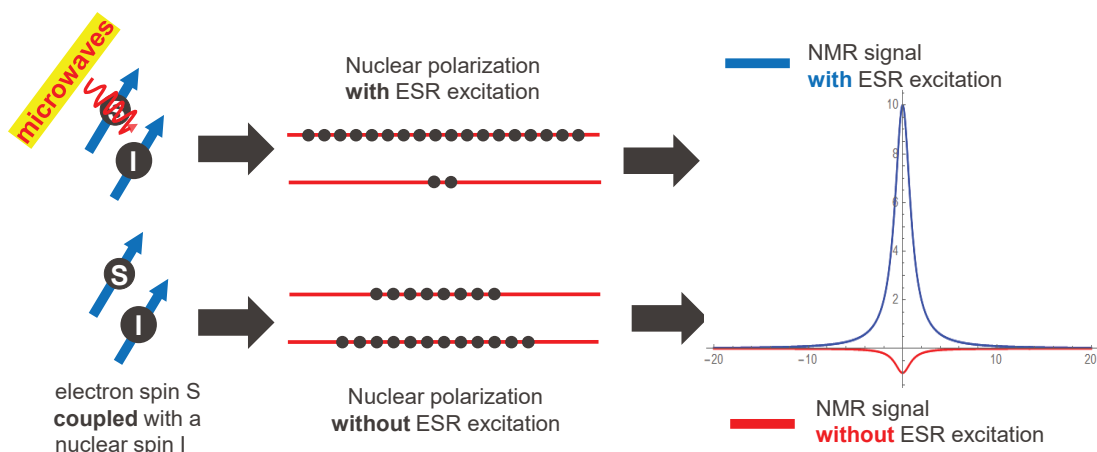
Figure 1.2: **Graphical illustration of microwave driven DNP technique.** This figure is not quantitative.

information on the local structures of such systems which might not be available with other methods.

DNP has not yet reach its full potential due to incomplete knowledge of the electron-nuclear spin system. ESR detection together with DNP-enhanced NMR spectroscopy enables the study and understanding of the DNP mechanism, and possibly, the methods to enhance it efficiently [10].

1.2   Miniaturization of magnetic resonance sensors

In most of the situations studied by NMR spectroscopy the samples are concentration limited. In these conditions, the largest SNR is obtained with the largest possible sample volume compatible with the high homogeneity region of the magnet, at the strongest possible magnetic field. However, there are also situations where the sample is volume limited. For volume limited samples, the use of an inductive detector having a sensitive volume matched to the volume of the sample under investigation results in a significant improvement of the SNR [11–22].

Many scientifically and industrially relevant samples have typical dimensions and/or spatial variations of their properties of interest in the subnanoliter range. These include small agglomerates of biological cells (with and, possibly also without, spin labels), tiny organisms such as C. elegans (which are ideal small systems for metabolomic studies), microelectronics devices (with paramagnetic entities such as defects, impurities, and dopants), and small single crystals (which are difficult to grow and/or have anisotropic ESR spectra and, hence, are hardly measurable in powder form). Due to this broad range of potential applications, the improvement of conventional inductive techniques and the development of new detection methods for high sensitivity spectroscopy is, nowadays, an important research topic (see, e.g., Ref. [23–27]).
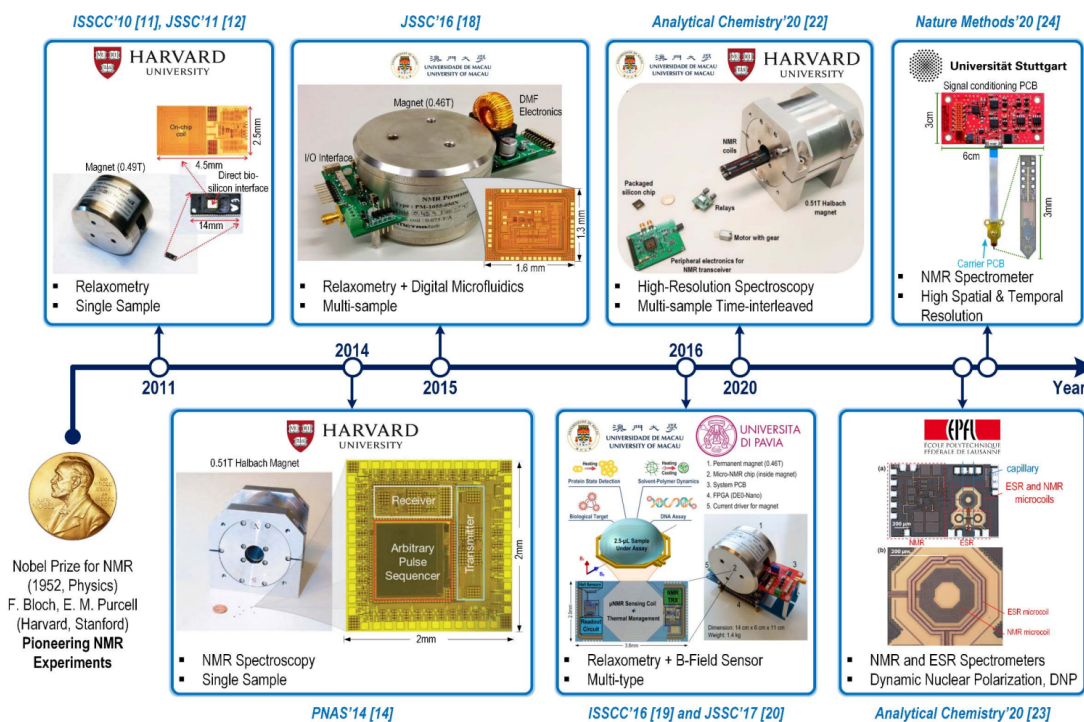
Figure 1.3: **The timeline of the development of miniaturized NMR systems [1].**

Matching the sensitive volume of the inductive detector to the sample volume, optimizes the signal and noise generated on the inductor and ensures the largest SNR. Microcoils have been used for samples at the nanoliter and subnanoliter scale [11, 28–30]. There are several advantages of miniaturization of magnetic resonance sensors [31, 32]. It is an interesting approach not only to achieve better SNR for small samples but possibly also for the reduction of the cost and complexity. Miniaturization allows improved excitation by the reduction of power needed for optimal excitation. It is also advantageous for the high field hyperpolarization as the microwave excitation depth gets thinner with the increase of the frequency. Sample size reduction enables higher magic angle spinning (MAS) frequency. Resolution achieved by NMR experiments are improved by the increase of MAS frequency.

The equipments generally used in NMR and ESR experiments can be listed as a magnet, excitation and detection coils, excitation signal generator, transmitter, receiver, data digitalization and recording electronics. The equipment with the largest footprint in NMR and ESR experiments is the magnet. Benchtop systems with permanent magnets up to 3 T are available today [33–35]. Most of the times, increasing the magnetic field increases the footprint of the magnets. The highest steady magnetic field reported to date is about 45 T [36] and NMR experiments at fields up to 40 T have been performed [37]. Even though these magnets have large sizes, the volume of homogeneous field in those magnets are generally the limiting factor in probe sizes. Thus, even though the total size cannot be minimized at high fields, the probe sizes have to be minimized. This is another supporting factor towards miniaturization of

magnetic resonance sensors.

A large community of researchers is working in the miniaturization of NMR systems. Wu et al. has presented an RF microcoil for nanoliter samples in 1994 [28]. Olson et al. has reported a high-resolution microcoil for mass limited, nanoliter volume samples in 1995 [11]. The NMR mouse has been introduced in 1996 [38] as a surface NMR system supported with permanent magnets. In medicine, lab-on-a-chip miniaturized NMR platforms are used in detection and profiling of circulating tumor cells [39]. A single-board NMR spectrometer has been introduced based on a software defined radio architecture as a low cost miniature system [40].

Figure 1.3 shows the timeline of the development of miniaturized NMR systems as suggested in Ref. [1]. While some of these work include the miniaturization of the complete system, some of them focuses only on the electronics. A palm-NMR system has been introduced in 2011 [34] and a scalable NMR spectroscopy tool is proposed in 2014 [41]. In 2015, a multi-nuclear μNMR system which is supported with a digital microfluidic device has been introduced [42]. A hand held micro-NMR platform with B-filed stabilization [43] and a portable NMR system with parallelism [44] are published in 2016 and 2020, respectively. Probing brain physiology with high spatial and temporal resolution using a CMOS NMR needle has been proposed in 2020 [45]. Finally, the first single chip DNP microsystem with integrated ESR and NMR electronics has been shown in 2020 [46]. Details of the last work, which is a part of this thesis, are reported in chapter 2.

1.3   Integrated circuits for magnetic resonance

Over the years silicon technology has proven its influence in enabling the access of electronics to masses. By the power of silicon technology, today almost everyone around the world have their own computers in their pockets. Once the prototype of any chip is proven to be successful, the cost of each silicon chip is reduced dramatically because of mass production.

1.3.1   Integrated circuits for single chip NMR

As it is discussed in section 1.2, miniaturization of magnetic resonance sensors is of interest for several important reasons. For SNR maximization, the coil size of inductive sensors should match the sample size. Microcoils are introduced for this purpose [11, 28, 30]. As the size of the coil shrinks, it gets more critical to amplify the signal before the SNR is degraded in the connections between the microcoil and the first amplification stage, typically an RF low noise amplifier (LNA). For sizes in the tens of micrometers to few hundred micrometers, integration of the amplifier in the same chip as the microcoil is advantageous because it minimizes the connection length from the microcoil to low noise amplifier (LNA) to a few micrometers. A step forward for SNR optimization is the on-chip down-conversion of the RF signal. This provides low frequency output signal which can be further amplified on-chip

for better protection of the signal from interferences and noise coupling and easier signal handling, which is especially important for arrays of NMR sensors. This leads to an increase in the integration level of electronics for the interest of not only low cost but also high SNR.

Single chip magnetic resonance sensors are especially promising for volume limited samples. Single chip NMR and ESR sensors have been shown in the past 20 years. The first integrated NMR probe has been reported in 2001, where a receiver is integrated for NMR magnetometry [47]. Since then, array of NMR receivers [44, 48], fully integrated IQ receivers [49], transceivers [34, 50] and sophisticated NMR chips [41, 42, 51–57] have been reported. As predicted by many review papers [1, 31, 32, 58] more will come in the integrated circuit approach of NMR. Integrated circuit approach in MR sensor design is one of the miniaturization techniques. Fig. 1.3 presents miniaturized systems which also include integrated circuits of different integration levels.

1.3.2 Integrated circuits for single chip ESR

At frequencies above 1 GHz, ESR measurements are usually performed using either relatively large cavities (sensitive volumes of milliliter to microliter) or miniaturized conducting [27, 59–65] and superconducting [24–26, 66–71] resonators (sensitive volumes of microliter to subpicoliter). Miniaturized resonators are adopted for the maximization of the SNR in ESR experiments with small samples. Inductive methods based on microresonators have sensitivities at the level of 10^7–10^{11} spins/Hz$^{1/2}$ at room temperature [63, 65, 72–74] and of 10^2–10^6 spins/Hz$^{1/2}$ at low temperature [24, 25, 27, 70, 71, 73], mainly depending on the sample relaxation times, the sensitive volume of the microresonator, the operating frequency, and the adopted normalization criteria. Non-inductive techniques can achieve single electron spin sensitivity [75–77] but are generally considered as less versatile than those based on the more conventional inductive approach [23, 25, 27].

Single chip ESR detectors contain a miniaturized LC-resonator but, in contrast to conventional miniaturized resonators, they also include the microwave source and the most critical part of the detection electronics in a small chip of less than 1 mm^2. In the single chip approach all elements which influence the spin sensitivity are located at less than 1 mm from the detection coil, de-facto eliminating all concerns about SNR degradation in the connections. This is particularly important at frequencies exceeding 100 GHz, where conventional approaches require expensive technologies to limit the degradation of the SNR. Deep submicrometer technologies allows for the design of integrated oscillators exceeding 300 GHz in CMOS [78] and SiGe technologies [79–90], and 500 GHz in HEMT technologies [91], with possible extension to the THz region in the near future [92]. This means that the single chip approach is well suited for ESR spectroscopy up to the largest magnetic fields currently available. At frequencies exceeding 100 GHz conventional approaches require expensive quasi-optical technologies. Furthermore, the small size of each chip and the on-chip frequency downconversion of the ESR signal into a robust low frequency signal might allow one to create dense arrays of independent detectors
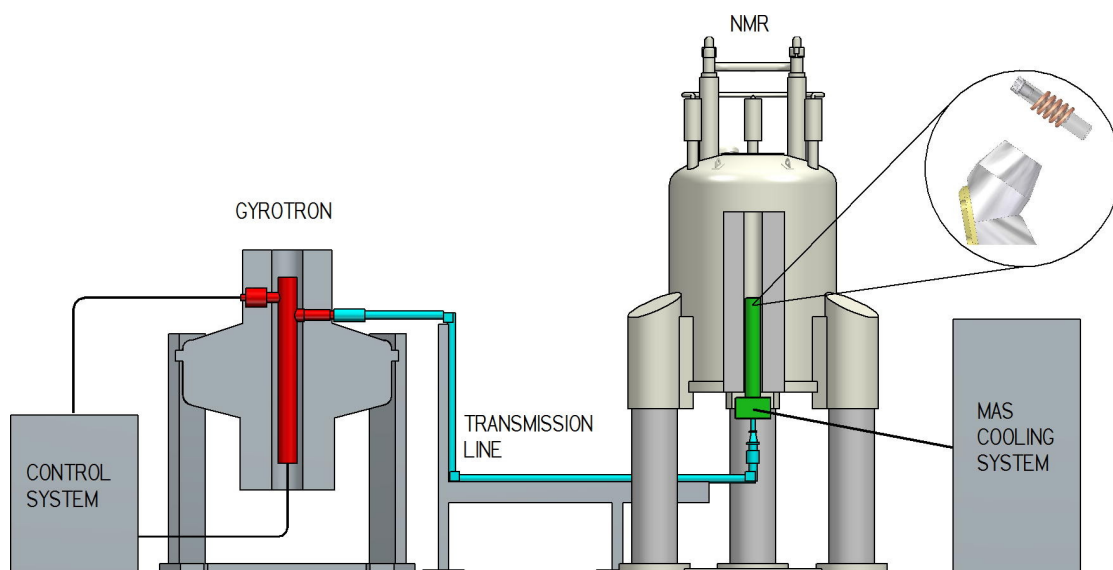
Figure 1.4: **Schematics of a solid-state DNP NMR system [2].** Gyrotron microwave source with gyrotron tube shown in red, microwave transmission line is shown in cyan and low-temperature NMR probe is shown in green. Single chip DNP microsystem that we develop doesn't require the gyrotron and microwave transmission lines.

that can be placed in the same magnet for simultaneous measurements on several samples ("parallel spectroscopy"). The absence of microwave input/output connections might allow the use of single chip ESR detectors also inside human/animal cavities (e.g., for local oximetry measurements) using small diameter low frequency cables or an entirely wireless approach.

In 2008, the first single chip ESR detector was demonstrated [72]. It consisted of an integrated CMOS LC oscillator and was used for continuous wave experiments. This system worked at 9 GHz and achieved a spin sensitivity of $N_{min} \cong 10^{10}$spins/Hz$^{1/2}$. Since then, several integrated oscillator based ESR sensors are proposed reaching operating frequency up to 263 GHz and achieving spin sensivity down to $N_{min} \cong 10^7$spins/Hz$^{1/2}$ [72–74, 93–96]. Some of these integrated ESR detectors have been working from 300 K down to 1.4 K [73, 94]. Arrays of such ESR detectors are proposed for parallel spectroscopy and increased concentration sensitivity [96–99]. These approaches are suitable, e.g., for the miniaturization of the probe, for the reduction of the losses and complexity of the connections, and for the realization of dense arrays of detectors.

1.3.3   Integrated circuits for single chip DNP

An approach to increase the SNR in NMR spectroscopy, applicable to samples of any volume, is to increase the nuclear spin polarization, e.g., by microwave, optical, and chemistry-based methodologies [100–110]. In the microwave dynamic nuclear polarization (DNP) approach, the sample under investigation contains unpaired electron spins which are excited into elec-

tron spin resonance as also explained in section 1.1. The electron spin excitation allows to enhance the nuclear magnetization of several orders of magnitude above its thermal value, improving the SNR in the NMR experiment by the same factor and reducing the required experimental time as the square of this factor. Recently, a microfluidic Overhauser DNP chip is proposed for signal-enhanced compact NMR experiments [111]. Overhauser enhancements up to 60 have been shown. This system is composed of a microfuidic chip with RF coils and microwave resonators. It does not integrate a microwave generator, so it does not remove the need of microwave generator and waveguides. Integrated circuits for single chip DNP studies where ESR and NMR detectors are combined in an integrated single chip has not been reported before this thesis work [46].

1.4 Thesis motivation

Extensive research efforts have been performed in the integration of NMR and ESR sensors for the reasons that have been described in the previous discussion. The strong motivation to improve the NMR sensitivity has resulted in a wide range of hyperpolarization research. Increasing the sensitivity of NMR by hyperpolarization usually requires costly equipments and a high level of expertise, and are generally applicable to a limited class of samples [8].

Even though DNP enhanced NMR is such a powerful method, the advancement in the field was relatively slow because of technical challenges. Microwave driven DNP was limited to the static field level of 1.5 T until the so-called "renaissance of DNP" [112]. In 1995, Griffin and coworkers have presented high field DNP experiments by the introduction of a high power high frequency generator, commonly called gyrotron, to the setup [113]. This opened the doors to high field DNP studies, which resulted in commercially available products today [114]. However, the field could advance at faster pace if these systems would be easily accessible by more researchers around the world. Even though commercial products exist, they are rather costly and complex. Fig. 1.4 shows the schematics of a solid-state DNP NMR system which consists of an NMR magnet, a gyrotron, a gyrotron control system, transmission line for microwaves and a MAS cooling system. The generation of the microwave magnetic field is not the only complexity of such systems, but also the way to carry the microwaves to the magnet and direct those microwaves to the sample region effectively introduces other complexities.

The main goal of this thesis is to demonstrate that it is possible to integrate ESR and NMR detectors in a single chip, removing the need of external microwave generators and transmission lines/waveguides for signal transfer. With this purpose, we have realized two single chip DNP microsystems that work at 10 GHz and 200 GHz ESR excitation frequencies. The studies aiming at the reduction of the magnet size, integration of all the electronics from the pulse sequencer to the analog-to-digital converters (ADC) and the use of commercially available discrete devices in complete MR systems such as FPGAs for software defined radios are definitely important in view of the complete miniaturization of NMR systems. However, the main focus of this work lies in the integration of the sensitivity relevant electronics of the
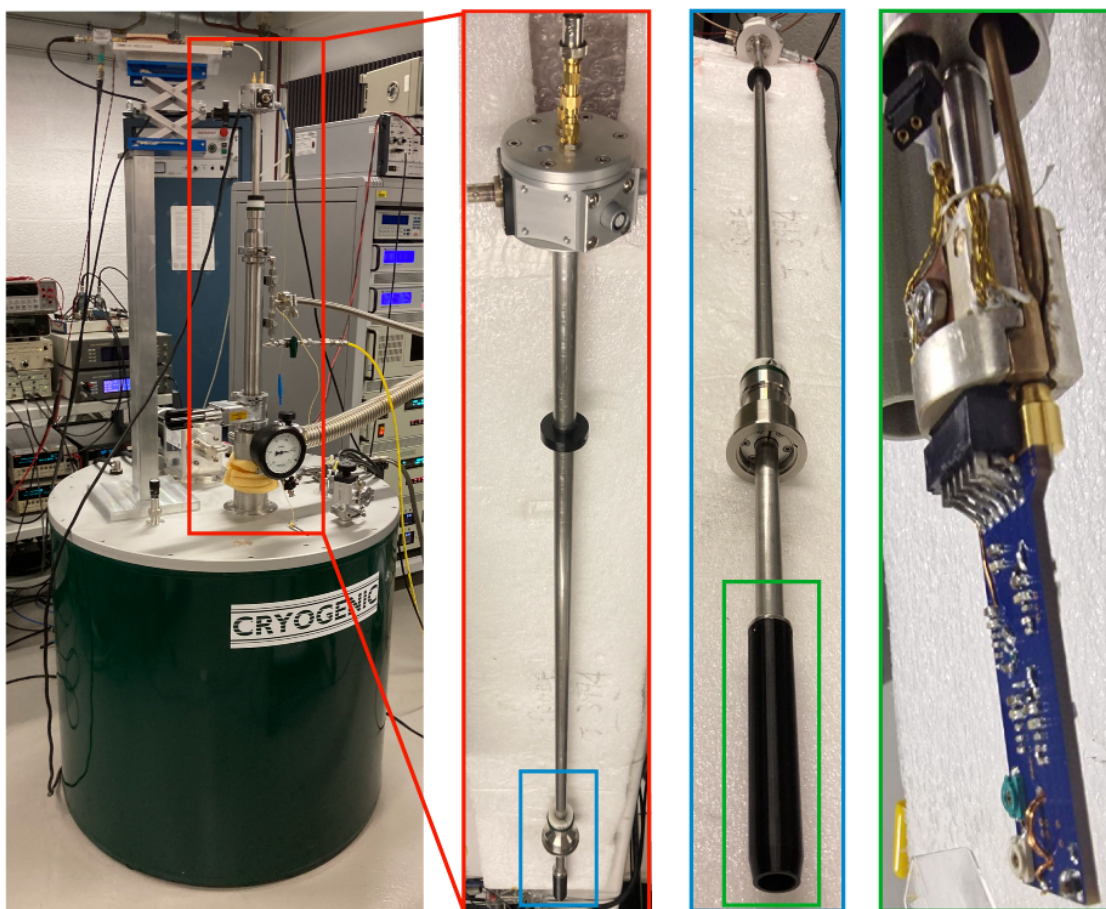
Figure 1.5: **Photograph of the magnet and the probe used in the experiments.** The programmable superconducting magnet with variable temperature insert (1.4-300 K, 0-9.4 T, Cryogenic Ltd) is in the left. The single chip DNP microsystem PCB is in the green rectangle. The PCB is connected to the probe which has two coaxial cables and twelve twisted pair wires along the metallic rod shown in the blue and the red rectangles. Other electronic equipments used in the experiments are reported in Chapters 2, 3 and 4.

ESR and NMR detectors.

We propose single chip dynamic nuclear polarization microsystems to reduce the cost and complexity of DNP experiments such that it will be available to researchers from a potentially wide range of fields: physics and chemistry to study the DNP mechanism, biology to study cells and metabolism, medicine and pharmacology for the detection of illnesses, for the understanding of evaluation of different kind of illnesses, and for drug development.

There are still a lot of unknowns in the DNP mechanism and theory is being build up upon the experimental data. To unravel the details of how DNP works and how it can be improved, it is necessary to study ESR and NMR at the same time. Single chip DNP microsystems that consists of integrated ESR and NMR detectors are potentially powerful tools for this mission. We believe that the low cost single chip DNP microsystem will be accessible to more researchers and empower DNP studies.

The power consumption of single chip DNP microsystems are not negligible for cryogenic temperature operation. At temperatures below 1 K, the effective cooling power available with ^{3}He and ^{3}He^{4}He dilution refrigerators is typically below 1 mW [115]. Special integrated circuit design is necessary to reduce the power consumption of the integrated electronics for operation temperatures below 1 K. For this purpose, we have investigated the possibility of integrated high electron mobility transistor (HEMT) oscillators as ESR detectors. The characterization of the HEMT ESR detectors provides information for the possible future integration of single chip DNP microsystems in HEMT technology.

Finally, arrays of DNP microsystems integrated on a single chip will facilitate the parallelism of DNP experiments and increase the sample volume of study. Integrated arrays of NMR detectors [44, 48] as well as ESR detectors [96–99] has been reported. In this work, we propose and demonstrate a DNP array system which consists of four frequency locked oscillators.

1.5   Outline

This thesis is composed of five chapters. In chapter 1, we introduce the integrated single chip approach for dynamic nuclear polarization experiments. In chapter 2, the first single chip DNP microsystem that works at ESR excitation frequency of 10 GHz is introduced. Overhauser and solid effect DNP enhancements at room temperature and ESR experiments down to 15 K are reported.

In chapter 3, a single chip 200 GHz DNP microsystem and solid effect DNP experiments at 100 K and 15 K are reported. This chapter also includes a single chip DNP array microsystem which is used in solid effect DNP experiments at 300 K and 200 K.

In chapter 4, low power HEMT oscillators for possible extension to cryogenic single chip DNP microsystems are investigated. Single chip ESR detectors based on a 10 GHz and a 35 GHz oscillator are realized with HEMT technology are presented along with HEMT transistor

characterization from 300 K down to 1.4 K.

Lastly, in chapter 5, we summarize the main results of this thesis and suggest possible future activities in the single chip DNP microsystems area.

2 Single chip 10 GHz DNP microsystem

This chapter is a modified version of the article "Single Chip Dynamic Nuclear Polarization Microsystem, N. Sahin Solmaz, M. Grisi, A.V. Matheoud, G. Gualco, G. Boero, *Analytical Chemistry 91(14)*, 2020." [46]. In particular, additional measurement results are reported and discussed. I have contributed to the chip design, measurements, simulations, data analysis and paper writing of this work.

2.1   Introduction

Nuclear magnetic resonance (NMR) spectroscopy is a powerful tool employed in research, industry, and medicine. The use of NMR methodologies in an even wider range of applications is often hindered by the relatively large minimum number of resonating spins needed to achieve a sufficiently large signal-to-noise ratio (SNR) in the available experimental time. In most of the situations studied by NMR spectroscopy the samples are concentration-limited. In these conditions, the largest SNR is obtained with the largest possible sample volume compatible with the high homogeneity region of the magnet, at the strongest possible magnetic field. However, there are also situations where the sample is volume limited. For volume limited samples, the use of an inductive detector having a sensitive volume matched to the volume of the sample under investigation results in a significant improvement of the SNR [11–22]. For samples in the nanoliter and subnanoliter range, non-inductive detection methods have been also proposed, such those based on nitrogen-vacancies in diamond [116–119] and magnetic resonance force microscopy [120–124]. Another approach to increase the SNR, applicable to samples of any volume, is to increase the nuclear spin polarization, e.g., by microwave, optical, and chemistry-based methodologies [100–110, 125, 126]. In the microwave dynamic nuclear polarization (DNP) approach, the sample under investigation contains unpaired electron spins which are excited into electron spin resonance (ESR). The electron spin excitation allows to enhance the nuclear magnetization of several orders of magnitude above its thermal value, improving the SNR in the NMR experiment by the same factor and reducing the required experimental time as the square of this factor.

Figure 2.1: Schematics of the single chip ESR detector based on a differential Colpitts topology implemented using a CMOS technology (TSMC 180 nm, MS/RF) [94].

During the last two decades, the separate integration on a single chip of the front-end electronics of inductive NMR spectrometers [34, 41, 42, 44, 47–57] as well as ESR spectrometers [72–74, 93–95] have been demonstrated. These approaches are suitable, e.g., for the miniaturization of the probe, for the reduction of the losses and complexity of the connections, and for the realization of dense arrays of detectors. In this work we demonstrate the co-integration on a single silicon chip of the front-end electronics of an NMR and an ESR detector. The excitation/detection planar spiral microcoils of the NMR and ESR detectors are concentric and interrogate the same sample volume. This combination of sensors allows to perform dynamic nuclear polarization (DNP) experiments using a single chip integrated DNP microsystem having an area of about 2 mm^2.

In this chapter, the design and characterization of a 10 GHz single chip DNP microsystem is explained. ^{1}H DNP-enhanced NMR experiments on liquid samples as well as solid samples having a volume of about 1 nL performed at 10.7 GHz(ESR)/16 MHz(NMR) are reported. NMR enhancements as large as 50 are achieved for TEMPOL/H$_2$O solutions and as large as 20 are achieved for a solid sample of 2% BDPA:SEBS at room temperature.

The single chip DNP microsystem is composed of two parts, the ESR and the NMR detectors. The ESR and NMR integrated electronic circuits are similar to those described throughly in Refs. [50, 94]. The chip has a size of 1.1×1.6 mm^2 and it is fabricated using a standard silicon complementary metal oxide semiconductor (CMOS) technology (TSMC 180 nm, MS/RF).

2.2 ESR detector

The ESR detector is a differential Colpitts LC oscillator operating at 10.7 GHz. In Fig.2.1, the schematic of the ESR detector is shown. The oscillation frequency of the oscillator is

determined by the inductor L and the capacitors C_1 and C_2. The oscillations are sustained by the amplifier formed with transistors and a biasing inductor L_{bias}. The ratio between C_1 and C_2 capacitors sets the positive feedback that is necessary for the oscillation condition to be met. The oscillator is powered from a V_{DD} pad, and it has two outputs (V_{O+} and V_{O-}) which are differential. The output can be taken as differential and/or single ended by terminating one of the outputs with 50 Ω. In this work, one of the outputs of the ESR oscillator is terminated by a 100 pF capacitor and a 50 Ω resistor to ground (see Fig. 2.2).

The ESR microcoil (inductor L in Fig.2.1) has two turns and an external diameter of 270 μm, a wire width of 12 μm, a wire thickness of 2.3 μm, and a spacing of 2 μm between turns. The ESR detector is a slightly modified version of the one reported in Ref. [94], where the bonding pads are distanced to facilitate the placement of a capillary containing the liquid sample under investigation. The DC power consumption of the ESR circuit is 90 mW at the maximum supply voltage of the oscillator of 2 V, and 5 mW at the minimum supply voltage of the oscillator of 0.85 V.

2.3 NMR detector

The NMR detector consist of a broadband (10 MHz to 1 GHz) transmit/receive electronic circuit directly connected (i.e., without tuning and matching capacitors) to an excitation/detection microcoil [50]. The NMR microcoil has 10 turns, an external diameter of 191 μm, a wire width of 3 μm, a wire thickness 2.3 μm, and a spacing of 2 μm between turns. Resulting inductance and series resistance are simulated as 17 nH and 28 Ω at 16 MHz, respectively.

The NMR transceiver consists of a transmitter and a receiver as shown in Fig. 2.2. The NMR transmitter consists of cascaded inverter amplifiers and switches (see transmitter part of the NMR circuit in Fig. 2.2). The excitation signal is provided from V_{TX} pad and is switched with the control signal V_{SW}. Using the switches at the input of the transmitter rather than at the output is favorable for the maximum output current transfer to the excitation/detection coil. Fig. 2.2 shows the switches in the transmit mode. When the integrated switch is in the transmit mode, a peak-to-peak RF voltage of about 2.5 V and a peak-to-peak RF current of about 90 mA is delivered to the NMR microcoil and the dissipated power in the NMR microcoil is 28 mW. In the receive mode, the switches are connected to the supply nodes (V_{DD} and GND) and the inverters do not consume any power.

The NMR receiver consists of a broadband LNA (10 MHz to 1 GHz), a double balanced mixer (Gilbert cell) and a low frequency amplifier (see receiver part of NMR circuit in Fig. 2.2). The LNA provides the high gain and low noise needed to maximize the signal-to-noise (SNR) ratio. After amplification, the signal is down converted to kHz range with the mixer using a local oscillator (LO) signal provided from outside by the V_{LO} pad. The LO signal is made differential using inverter chains similarly to the transmit signal V_{TX} (see Fig. 2.2). The difference in the V_{TX} signal path are the switches, which are not used in the V_{LO} signal path. The down-converted signal is further amplified and converted from differential to single ended for easier
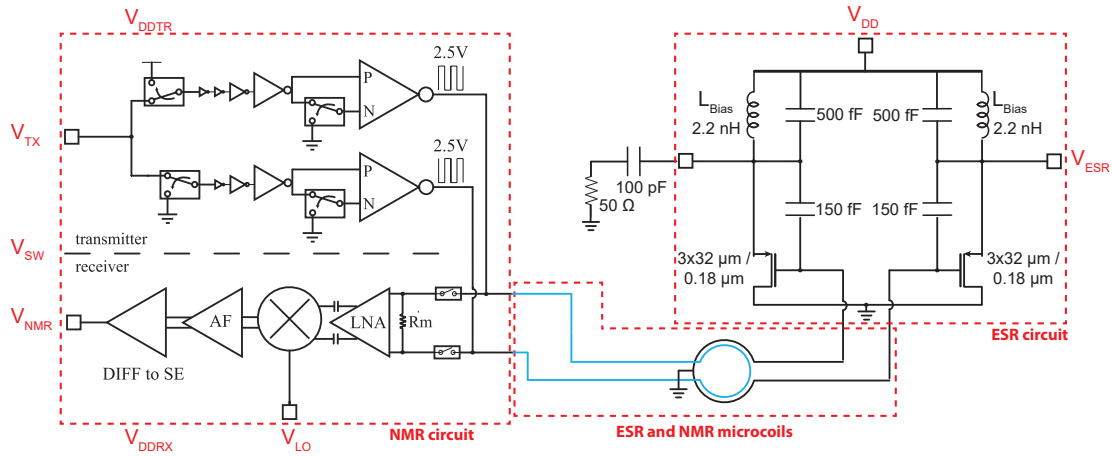
Figure 2.2: **Schematic of the 10 GHz single chip DNP microsystem.** The dashed red lines indicate the NMR/ESR circuits and the concentric NMR/ESR microcoils. Black squares next to the port names represent the bonding pads. V_{DDTR}, V_{DDRX}, and V_{SW} ports are connected to several nets and their connections are not shown in the schematic for simplicity. V_{DDTR} and V_{DDRX} are the supply voltages of all the blocks in the transmitter and receiver of the NMR circuit, respectively. V_{SW} is the control signal that is connected to all the switches in both transmitter and receiver of the NMR circuit.

manipulation afterwards and reduced number of connections. At the output of the NMR receiver, the signal is at kHz frequencies. After this point, the NMR signal is immune to high frequency interferences and noise couplings. The NMR receiver is connected to the integrated NMR microcoil (shown in blue in Fig.2.2) via switches that are controlled with the same V_{SW} signal. The DC power consumption of the NMR system is 70 mW in the transmit mode and 40 mW in the receive mode.

2.4 Co-integration of ESR and NMR detectors

The NMR microcoil is concentrically placed inside the ESR microcoil (see Fig. 2.2, Fig. 2.3(b) and Fig.2.4). The two coupled concentric microcoils are simulated using a full wave electromagnetic simulator (Advanced Design System ADS, Keysight Technologies). The obtained S-parameter files are used in an integrated circuits simulator (Cadence, Cadence Design Systems Inc.) to simulate both the ESR and the NMR integrated detectors. In these simulations it is found that an NMR coil with more than 15 turns significantly reduces the quality factor of the ESR coil and quenches the oscillation of the ESR circuitry. This is qualitatively explained by the losses caused by the induced currents in the NMR coil. To keep a safety margin, the implemented NMR coil has 10 turns.

Electromagnetic and electrical simulation of the integrated microwave oscillator, performed with ADS and Cadence, show that the maximum achievable microwave current I_{mw} in the

Figure 2.3: **Photograph of the 10 GHz single chip DNP microsystem.** (a) Chip photograph showing in red dashed lines: the NMR circuit, the ESR circuit, and the co-integrated ESR and NMR microcoils. (b) The co-integrated ESR and NMR microcoils.

ESR microcoil is of 74 mA, obtained with an oscillator supply voltage of 2 V. Figure 2.4 shows the result of a COMSOL simulation performed with a microwave current I_{mw} =74 mA in the ESR microcoil. The indicated magnetic field (B_{1e}) is half of the magnitude of the componen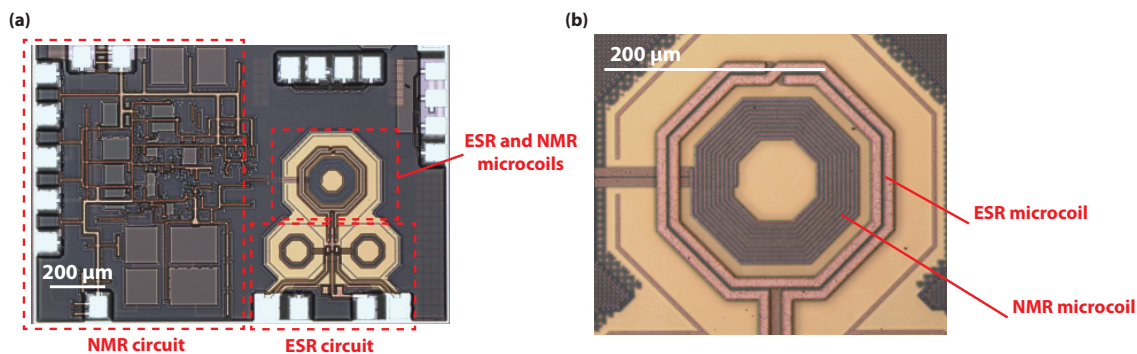t of the microwave magnetic field perpendicular to the static magnetic field in two orthogonal cross-sections of the capillary where the sample is confined. The microwave magnetic field B_{1e} in the center of the coil is about 100 μT. The obtained microwave magnetic field is the result of the superposition of the microwave magnetic field created by the ESR coil and the microwave magnetic field caused by the induced microwave currents in the NMR microcoil. Moving vertically from the chip (and coils) surface into the sample region, the total microwave magnetic field first decreases, cancels out in the dark blue region, then increases, and finally decrease again further away from the chip surface. This is the expected magnetic field produced by two concentric coils of different diameter carrying currents flowing in opposite directions. Simulations of the microwave magnetic field produced by the ESR microcoil with the NMR microcoil terminated with a high impedance (or without the NMR microcoil) show that the average microwave magnetic field in the sample region could be increased by almost one order of magnitude (and, as expected, in the center of the coil would be approximately given by $B_{1e} = \mu_0 I_{mw}/d \cong 400$ μT).

To cross-check these simulation results, we performed experiments with a single crystal of 1:1 α,γ-bisdiphenylene-β-phenylallyl (BDPA/benzene, 152560, Sigma-Aldrich) having a size of about 70×70×5 μm^3 placed in the center of the ESR microcoil (Fig. 2.4d). At room temperature, BDPA has relaxation times $T_1 \cong T_2 \cong 100$ ns [128]. The linewidth depends only on B_{1e} and the relaxation times as in the equation $\Delta B_{0,zc} = (2/\gamma T_2)(1 + \gamma^2 B_1^2 T_1 T_2)^{1/2}$ [127], where $\Delta B_{0,zc}$ is the field difference between the two zero-crossing of the ESR signal and it corresponds to the peak-to-peak linewidth of the dispersion signal measurable without magnetic field modulation. The knowledge of the relaxation times and the measurement of the linewidth allows to estimate value of B_{1e}. From the measured ESR signals reported in Fig. 2.4d, the extracted value of B_{1e} in the center of the ESR microcoil is about 70 μT at the maximum supply
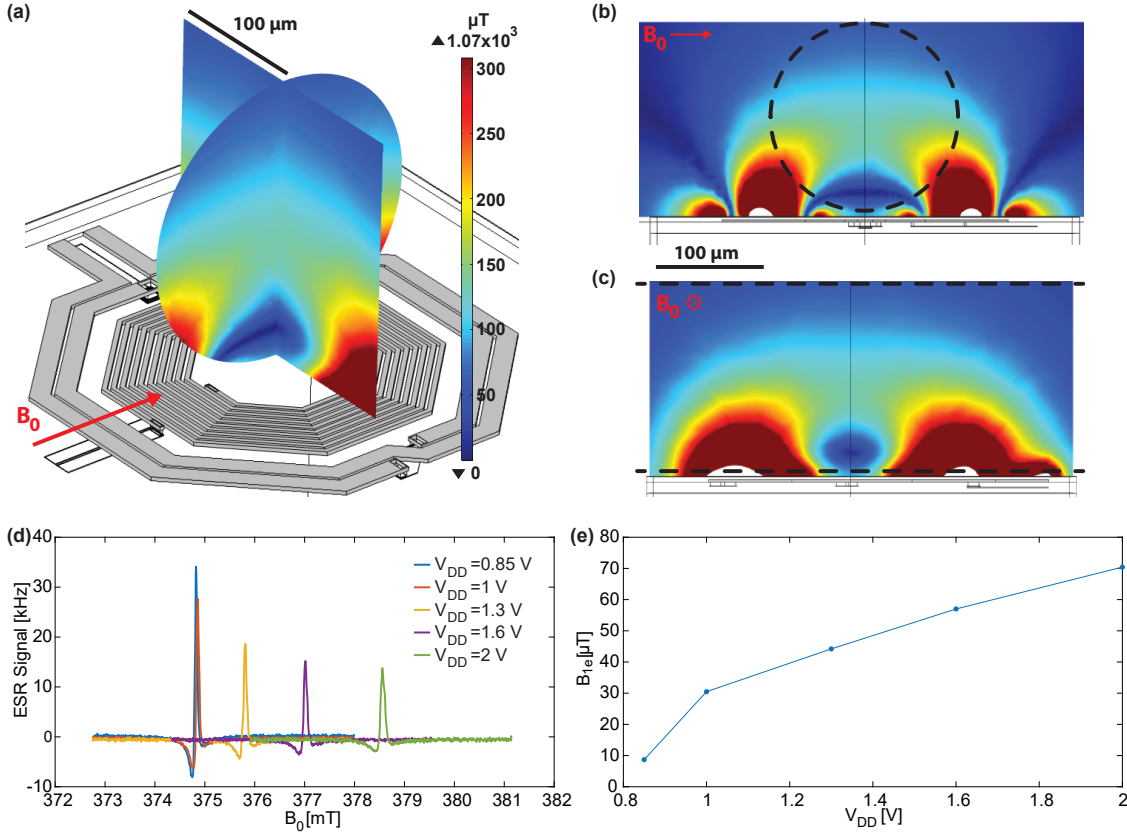
Figure 2.4: **Simulations and experiments for the characterization of the microwave magnetic field produced by the ESR microcoil. (a)** Three dimensional representation of the ESR and NMR microcoils together with the map of the microwave magnetic field B_{1e}, defined as half of the component perpendicular to the static magnetic field B_0 (indicated by the red arrow) of the microwave magnetic field produced by the microwave current into the ESR microcoil. In **(a)**, the two perpendicular cross-sections correspond to the region occupied by the water solution inside the capillary. In **(b)** and **(c)** are reported the maps of B_{1e} in two larger regions. The black dashed lines indicate the region occupied by the water solution inside the capillary. The simulation are performed using COMSOL Multiphysics (COMSOL Inc.). The amplitude of the microwave current in the ESR microcoil is set to 74 mA, according to the combined results of simulations of the ESR/NMR integrated electronics performed with Advanced Design System (ADS, Keysight Technologies) and Cadence (Cadence Design Systems Inc.). **(d)** ESR spectra of a sample of BDPA placed in the center of the ESR microcoil for different ESR oscillator supply voltages V_{DD}. The increase of the resonance static magnetic field is due to the increase of the oscillator frequency with the oscillator supply voltage V_{DD}. **(e)** Microwave magnetic field B_{1e} in the center of the ESR coil extracted from the measurement of the linewidth of the ESR signals shown in **(d)** according to the equation $\Delta B_{0,zc} = (2/\gamma T_2)(1 + \gamma^2 B_1^2 T_1 T_2)^{1/2}$ [127]. Experimental conditions: $f_{mw} \cong 10.7$ GHz, modulation frequency: $f_m = 16.7$ kHz, modulation magnetic field: $B_m \cong 6$ μT.

voltage of the oscillator of 2 V (Fig. 2.4e), corresponding to the simulated maximum current in the ESR coil of 74 mA. As discussed above, the full wave COMSOL simulation gives a B_{1e} in the center of the ESR microcoil of about 100 μT, in good agreement with the 70 μT estimated from these BDPA measurements.

2.5 Overhauser DNP at room temperature

Overhauser DNP experiments are performed on TEMPOL/H_2O solutions to characterize the 10 GHz single chip DNP microsystem using liquid samples.

2.5.1 Measurement setup

The complete setup for the characterization of the single chip DNP microsystem is shown in Fig. 2.5. The frequency-to-voltage conversion of the ESR detector output is performed by a delay-line-discriminator (DLD) whose central frequency is 200 MHz. The DLD is designed in home with discrete devices according to basic delay line/mixer frequency discriminator method [129]. In order to match the DLD central frequency and improve the spectral purity, the signal at the output of the detector is amplified, mixed with an external reference, filtered, and shaped through a divide-by-1 frequency divider. The DC coupled output of the DLD is amplified and digitized by an analog-to-digital converter (ADC). This signal is used to monitor the ESR oscillator frequency. The AC coupled output of the DLD is amplified and sent to a lock-in amplifier for further amplification and synchronous demodulation. The lock-in amplifier also generates the reference signal which is used for the magnetic field modulation.

An NMR magnetometer is used to track the variations of the magnetic field produced by the electromagnet in which the DNP experiments are performed. The frequency-lock with the NMR magnetometer is necessary due to the relatively large drift (about 1 ppm/h) of the electromagnet. The NMR frequency measured by the magnetometer is used to set the frequency of the RF generator connected to integrated transmitter V_{TX} and to the local oscillator V_{LO} of the integrated receiver. In particular, the RF generator frequency is set 20 kHz below the frequency measured by the NMR magnetometer. This allows to obtain an NMR signal above the $1/f$-noise corner frequency of the integrated NMR receiver. A switch signal V_{SW} determines the pulse width of the NMR excitation. The output of the integrated NMR receiver V_{NMR} is amplified, digitized, and digitally processed. The maximum NMR signal amplitude is obtained with a radiofrequency pulse length $\tau_{rf} \cong 5$ μs. The maximum microwave magnetic field B_{1e} at the center of the ESR coil is about 70 μT, as estimated from measurements performed on a BDPA sample (see 2.4).

The samples are contained into borosilicate glass capillaries (BGCT 0.2, Capillary Tube Supply Ltd) of 0.2 mm outer diameter (OD) and 0.18 mm inner diameter (ID). The capillary are sealed with a torch (Microtorch, Prodont Holliger). The non-degassed solutions of pure water (H_2O)(W3500, Sigma-Aldrich) and 4-hydroxy-2,2,6,6-tetramethylpiperidine 1-oxyl (TEM-
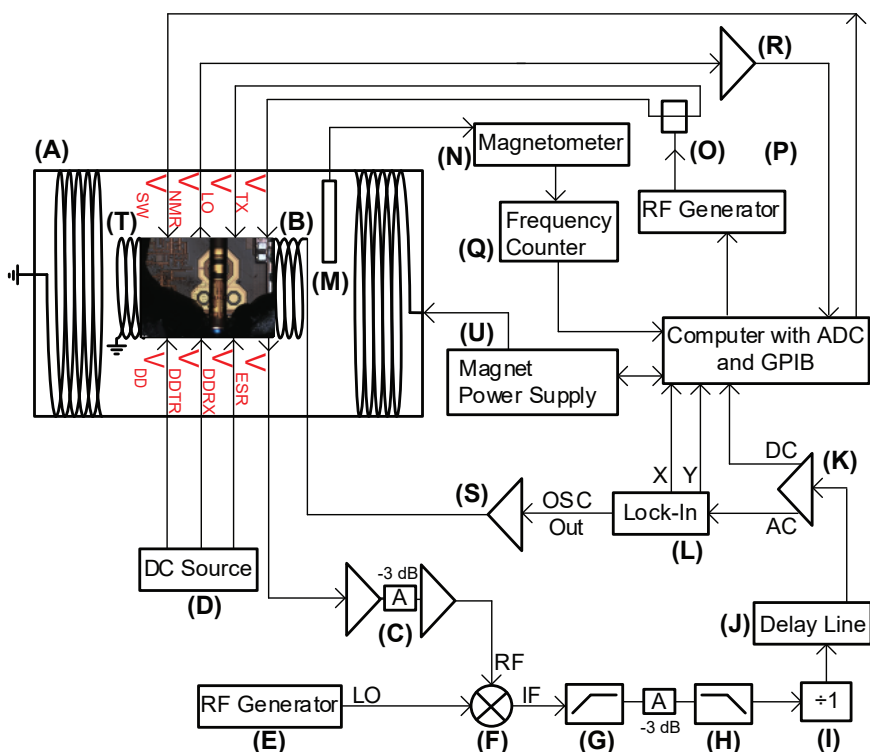
Figure 2.5: **Block diagram of the complete setup for the characterization of the 10 GHz single chip DNP microsystem with liquid samples:** (A) Electromagnet (Bruker, 0 to 2.2 T); (B) Home-made modulation coil (0.33 mT/A); (C) RF amplification stage composed of two RF amplifiers (Analog Devices HMC-C001) and a 3 dB attenuator; (D) Three DC power supplies (Keithley 2400); (E) RF generator (Rohde&Schwartz SMR-20) ; (F) Mixer (Mini-Circuits ZX05-153-S+); (G) 100 MHz high-pass filter (Crystek CHPFL-0100); (H) 300 MHz low-pass filter (Crystek CLPFL-0300); (I) Frequency divider (Valon Technology 3010); (J) Homemade delay-line-discriminator (200 MHz central frequency, 1 MHz detection range, 5 MHz FM bandwidth); (K) Amplifier (Stanford Research Systems SR560); (L) Lock-in amplifier (EG&G 7265); (M) NMR magnetometer probe (Metrolab Instruments SA 1062 probe 3); (N) NMR magnetometer main electronic unit (Metrolab Instruments SA PT2025); (O) RF splitter (Mini-Circuits ZFSC-2-11); (P) RF generator (Stanford Research Systems SG384); (Q) Frequency counter (Fluke PM6681); (R) Amplifier (EG&G 5113); (S) power amplifier (Rohrer PA508); (T) Photograph of the single chip DNP-NMR microsystem with the capillary containing the sample placed on the microcoils and the bonding wires protected by glob-top (the black material covering the bottom part of the chip); (U) Magnet power supply (Bruker, 0 to 150 A).
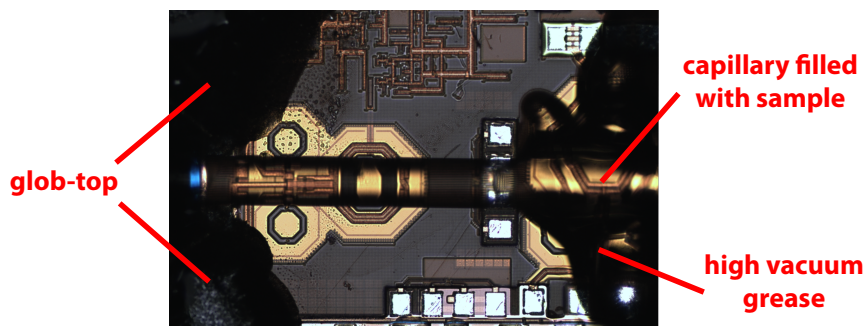
Figure 2.6: **Picture of the chip together with the sample filled in a capillary container.** The TEMPOL/H_2O solution in a borosilicate capillary is placed on top of the chip using high vacuum grease outside of the excitation/detection coils. Glob-top epoxy (EPO-TEK H20E) is used to protect the bondwires during the sample manipulation.

POL)(176141, Sigma-Aldrich) are obtained by dilution at room temperature in air starting from a 1 M solution. The degassed solutions are prepared as follows. The degassing of water is performed by bubbling with a nitrogen flow for about 1 h. A 200 mL glass vial, with inlet/outlet pipes for the nitrogen flow, is filled with pure water heated to 70 °C by a hot plate. A pipette is used to transfer the degassed water into a 2 mL glass vial containing the appropriate amount of TEMPOL molecules to produce a 100 mM solution. The 10 mM and 1 mM solutions are prepared into 2 mL glass vials by subsequent dilution in degassed water. The preparation of the solutions and the filling/sealing of the capillaries is performed in a few seconds to minimize the absorption of O_2 in contact with air (the diffusion length of O_2 in water in 1 s is about 60 μm).

2.5.2 Measurement results

The capillary encapsulated samples of TEMPOL/H_2O solutions are fixed on top of the single chip DNP microsystem with a small drop of vacuum grease (high vacuum grease, Dow Corning) as seen in Fig. 2.6. As shown in the left side of Fig. 2.7, at concentrations of 1 mM and 10 mM the ESR spectra consist of three hyperfine lines due the ^{15}N nucleus ($I = 1$). At concentrations of 100 mM and 1 M a single line is observed, as also reported by Gafurov et al. [130]. After obtaining the ESR spectrum, the B_0 magnetic field is set to one of the three maxima for concentrations of 1 mM and 10 mM and to the single maximum for the 100 mM and 1 M concentrations. For all NMR spectra shown in the right side of Fig.2.7, the RF pulse length is $\tau_{rf} = 5$ μs, the acquisition time is $T_{daq} = 400$ ms, and the pulse repetition time is $T_r = 500$ ms. The non-enhanced NMR spectra are the average of $N_{avg} = 100000$ spectra obtained in about 14 hours. The DNP-enhanced NMR spectra are the average of $N_{avg} = 1000$ spectra obtained in about 9 minutes. In the DNP-enhanced NMR measurements, the microwave excitation is present also during the NMR detection. The frequency shift between the non-enhanced and
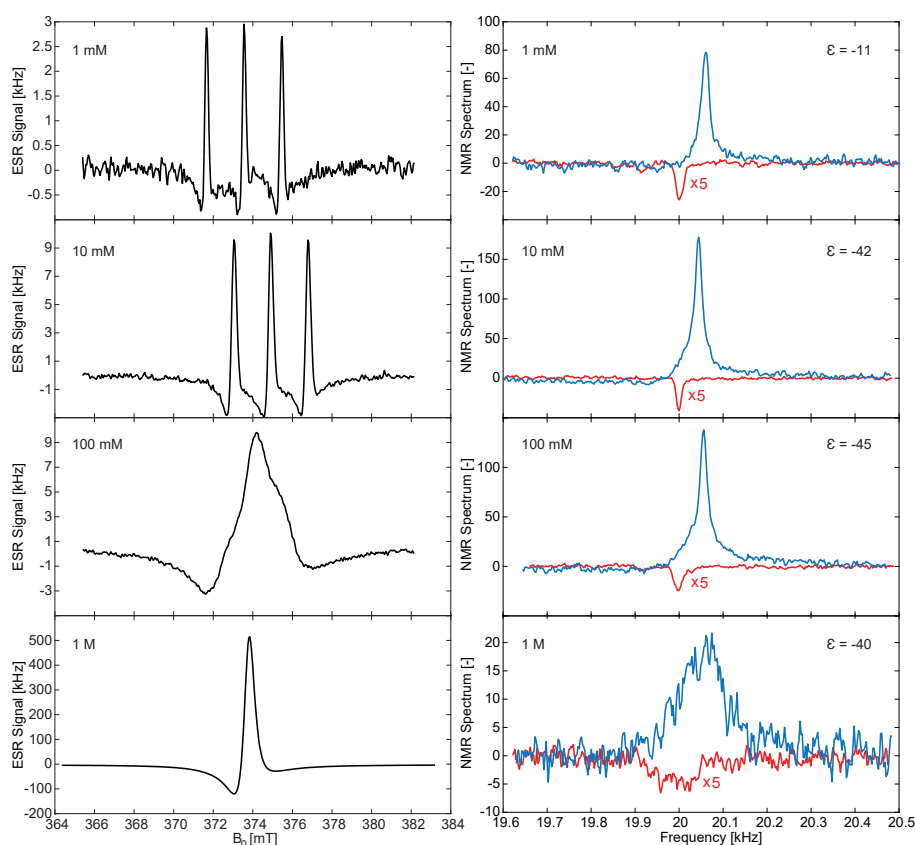
Figure 2.7: **ESR (left column) and NMR (right column) spectra of TEMPOL/H$_2$O solutions for different concentrations (1mM , 10 mM, 100 mM, and 1 M).** In the NMR spectra, the red curves are the non-enhanced ($B_{1e} = 0$) NMR spectra enlarged 5 times whereas the blue curves are the DNP-enhanced NMR spectra ($B_{1e} \cong 60$ μT). The DNP enhancement ε values for each spectra is given on the top-right corner. . The ESR measurements are performed in the following conditions: modulation frequency $f_m = 16.7$ kHz, modulation magnetic field $B_m \cong 6$ μT, microwave frequency $f_{mw} \cong 10.7$ GHz, microwave magnetic field $B_{1e} \cong 60$ μT. The NMR measurements are performed in the following conditions: $f_{rf} \cong 16$ MHz, pulse length $\tau_{rf} = 5$ μs, pulse repetition time $T_r = 500$ ms, time-domain match filter time constant $T_m = 100$ ms, acquisition time $T_{daq} = 400$ ms, number of averaging $N_{avg} = 100000$ (for the non-enhanced signal) and $N_{avg} = 1000$ for the enhanced signal.
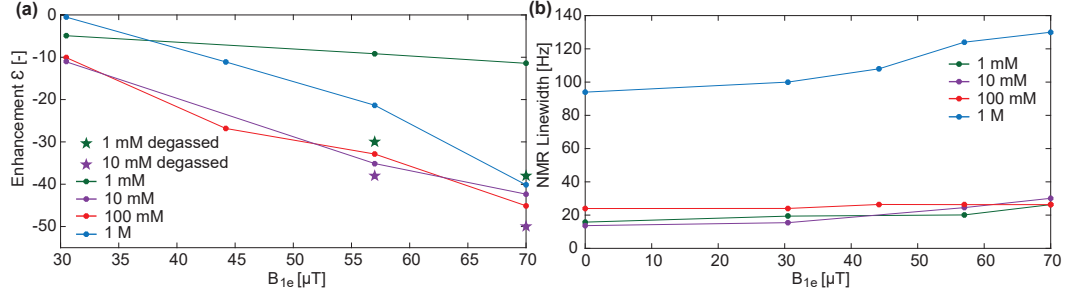
Figure 2.8: **DNP enhancement and NMR linewidth.** (a) Enhancement ε and (b) NMR linewidth of TEMPOL/H_2O solutions with different concentrations (1mM, 10 mM, 100 mM, and 1 M) at different microwave magnetic field B_{1e}. The enhancement is defined as the ratio of the integrals of the enhanced and non-enhanced NMR signals in the frequency domain. The NMR linewidth is defined as the full width at half maximum of the NMR signal in the frequency domain. At the operating frequency of 16 MHz, a linewidth of 20 Hz corresponds to 1.25 ppm.

enhanced NMR spectra is most probably caused by the DC current flowing in the ESR circuit. Even though the circuit is designed to be symmetric, it is not completely symmetric around the path of V_{DD} connection. The shift between the NMR spectra, which is around 60 Hz, can be caused by a magnetic field of around 1.5 μT. DC current of 45 μA in the V_{DD} connection can create a DC magnetic field of a few μT at the distance of half a millimeter. The observed shift (up to 4 ppm) is much larger than the one attributable to temperature effects. Since the temperature induced frequency shift for the ^{1}H nucleus in water is about 0.01 ppm/°C [131], the observed shift would correspond to a temperature increase of 400 °C, which is obviously impossible for a liquid water sample.

In all Overhauser effect measurements, the enhancement ε is defined as the ratio of the integrals of the enhanced and non-enhanced NMR signals in the frequency domain (see Eq. 2.1). We use the integral of the signal instead of the signal amplitude because the enhanced signal has a broader linewidth (see Fig. 2.7).

$$\varepsilon = \frac{\int (NMR_{MWON})\,df}{\int (NMR_{MWOFF})\,df} \tag{2.1}$$

Fig. 2.8 reports the DNP enhancements (Fig. 2.8a) and the NMR linewidths (Fig. 2.8b) obtained with TEMPOL/H_2O solutions having different concentrations. A maximum enhancement of about -50 is obtained with the largest B_{1e} (i.e., about 70 μT) with a 10 mM degassed solution. Enhancements in the order of -100 have been previously reported at 0.3 T [132–138]. In particular, Höfer et al. reported an enhancement of -100 for a 10 mM solution of TEMPOL/H_2O at room temperature (i.e., with the same test sample and experimental conditions of this work) [132]. The lower enhancement measured in our work is probably due to the lower average B_{1e} which, as shown in Fig. 2.8a, is insufficient to reach the saturation region. This is caused by the NMR coil inside the ESR coil, which reduces significantly the

microwave magnetic field B_{1e} produced by the ESR coil as explained in the description of the system.

Figure 2.8 shows also that the degassing of water increases the enhancement, especially for low radical concentrations. The enhancement of the NMR signal for the 1 mM degassed solution is almost three times larger than the one measured with the non-degassed solution. For the 10 mM sample, the enhancement increase caused by the degassing is much lower, probably due to the negligible additional relaxation induced by the presence of the O_2 molecules (0.2 mM at room temperature) with respect to the relaxation due to 10 mM TEMPOL molecules. As shown in Fig. 2.8b, for 1 mM to 100 mM concentrations, the NMR linewidth is about 20 Hz (i.e., 1 ppm), mainly limited by the lack of shim coils in the electromagnet (a very similar chip operated in a 7 T magnet equipped with shimming coils shows spectral resolutions down to about 2 Hz [55]). The NMR linewidth of the 1 M solution is about 90 Hz, presumably due to the large concentration of TEMPOL which significantly reduces the T_2 value [132, 139].

2.6   Solid effect DNP at room temperature

In addition to DNP experiments with liquid samples where the dominant DNP mechanism is the Overhauser effect, we performed experiments also with solid samples where the main DNP mechanism is the differential solid effect [140]. Solid effect DNP experiments are performed with 2% BDPA in styrene-ethylene-butylene-styrene (2% BDPA:SEBS), 10 mM BDPA:cis-polyisoprene and 2% BDPA in polystyrene (2% BDPA:PS) polymers to exemplify the use of the 10 GHz single chip DNP microsystem also with solid samples.

2.6.1   Measurement setup

To measure solid samples with short transverse relaxation time T_2, a different setup is used as shown in Fig. 2.9. In this setup, two different RF signal generators are used for excitation (V_{TX}) and down-conversion (V_{LO}) signals. Excitation signal V_{TX} is sent at the resonance frequency, whereas the down-conversion signal V_{LO} is at 125 kHz on the side to move the NMR signal to a spectral region where the $1/f$ noise and the distortions related to dead-time are avoided. However, this approach introduces a coherence problem. Even though we use two sources that are frequency locked, phase locking is not guaranteed. Since the phase difference between excitation and detection always changes, the signal would be lost during averaging. A second channel in ADC board is used to track the phase difference between those RF signals. The phase is corrected for each measurement before averaging in the digital signal processing performed by an home-made Labview^{TM} program.
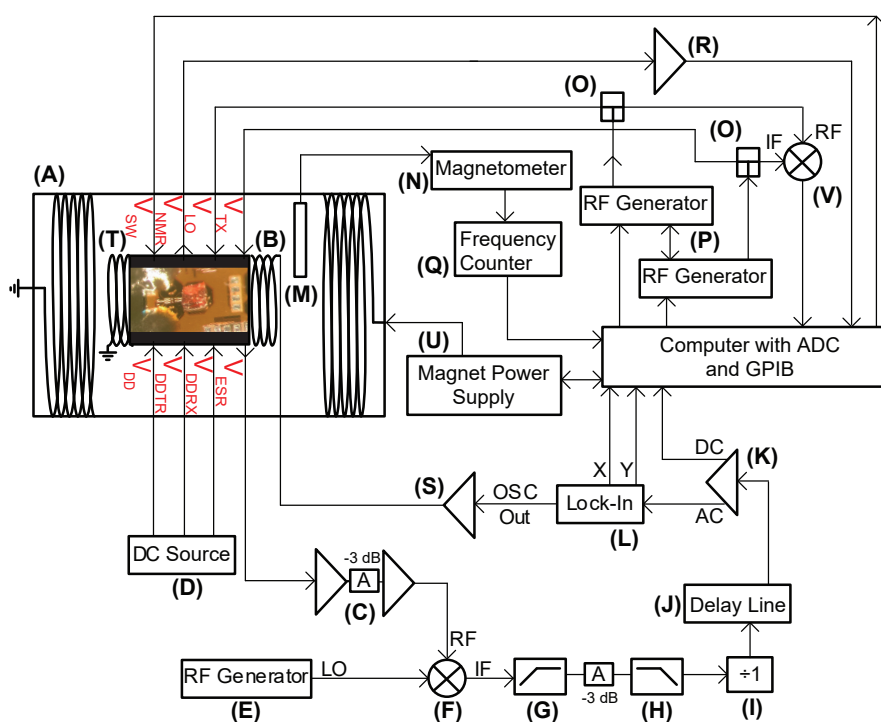
Figure 2.9: **Block diagram of the complete setup for the characterization of the 10 GHz single chip DNP microsystem with solid samples.** (A) Electromagnet (Bruker, 0 to 2.2 T); (B) Homemade modulation coil (0.33 mT/A); (C) RF amplification stage composed of two RF amplifiers (Analog Devices HMC-C001) and a 3 dB attenuator; (D) DC power supplies (Keithley 2400); (E) RF generator (Rohde&Schwartz SMR-20) ; (F) Mixer (Mini-Circuits ZX05-153-S+); (G) 100 MHz high-pass filter (Crystek CHPFL-0100); (H) 300 MHz low-pass filter (Crystek CLPFL-0300); (I) Frequency divider (Valon Technology 3010); (J) Homemade delay-line-discriminator (200 MHz central frequency, 1 MHz detection range, 5 MHz FM bandwidth); (K) Amplifier (Stanford Research Systems SR560); (L) Lock-in amplifier (EG&G 7265); (M) NMR magnetometer probe (Metrolab Instruments 1062 probe 3); (N) NMR magnetometer main electronic unit (Metrolab Instruments SA PT2025); (O) RF splitter (Mini-Circuits ZFSC-2-11); (P) RF generators (Stanford Research Systems SG384); (Q) Frequency counter (Fluke PM6681); (R) Amplifier (EG&G 5113); (S) power amplifier (Rohrer PA508); (T) Photograph of the single chip DNP-NMR microsystem with the 2% BDPA:SEBS sample placed on the microcoils and the bonding wires protected by glob-top (the black material covering the left part of the chip); (U) Magnet power supply (Bruker, 0 to 150 A).

Figure 2.10: **Picture of the chip together with the 2%BDPA:SEBS sample placed on top of the concentric ESR and NMR microcoils.**

2.6.2 Measurement results

BDPA doped polymers are measured to demonstrate the possibility to measure also solid samples with the single chip DNP microsystem. A common polymer that is used in DNP studies is polystyrene (PS). T_2 of PS is around 10 μs which makes it more challenging to measure compared to liquid samples which have longer T_2. As an intermediate form between solid and liquid samples, we have used also elastomers such as cis-polyisoprene and SEBS. Three solid samples are used in the measurements performed with our single chip DNP microsystem: 2%BDPA:SEBS, 2%BDPA:PS, and 10 mM BDPA:cis-polyisoprene.

The samples of 2% BDPA:SEBS, 2% BDPA:PS and 10 mM BDPA:cis-polyisoprene are prepared by dissolving SEBS (Kraton Corporation) and BDPA (152560, Sigma-Aldrich) in toluene, PS (331651, MW 35000, Sigma-Aldrich) and BDPA in chloroform, and cis-polyisoprene (182141, Sigma-Aldrich) and BDPA in toluene, respectively. The mixture is then drop casted on a glass plate and dried overnight inside a fumehood with a glass cover to reduce the speed of evaporation. If the evaporation is too fast the top surface of the sample becomes very irregular. The amount of chloroform and toluene determines the thickness of the resulting dried sample. Once the solvent completely evaporates, the dried sample is cut by a ceramic blade to a size of 200 μm x 200 μm x 100 μm. After samples are formed in the desired shape, they are picked up by toothpicks that are sharpened by a cutter. The samples are attached to the chip surface by Van der Waals forces (i.e. no glue required). The placement of a 2% BDPA:SEBS sample of size approximately of 200 μm x 200 μm x 100 μm is shown in Fig. 2.10 as an example.

In all solid effect measurements, the enhancement ε is calculated as the ratio of the NMR signal amplitude values in the frequency domain when microwaves are on and off. For these solid samples, the linewidth of the non-enhanced NMR signal is the same as the one of the enhanced signal, so the integration in Eq. 2.1 is not necessary.

Figure 2.11: **ESR spectrum of 2%BDPA:SEBS.** The oscillator is supplied with V_{DD} = 1.8 V and I_{DD} = 40 mA. Experimental conditions: modulation frequency f_m =1.234 kHz, modulation magnetic field $B_m \cong$ 1.8 mT, microwave frequency $f_{mw} \cong$ 10.4 GHz, microwave magnetic field $B_{1e} \cong$ 60 μT.

Figure 2.12: **NMR spectra of 2%BDPA:SEBS with and without microwaves.** When microwaves are applied on the right side of the ESR peak ($\omega_{OS} + \omega_{OI}$) the enhancement is 20 (red curve), whereas it is -15 when the microwaves are applied on the left side of the ESR peak ($\omega_{OS} - \omega_{OI}$) (pink curve). The NMR measurements are performed in the following conditions: $f_{rf} \cong$ 16 MHz, pulse length τ_{rf} = 5 μs, pulse repetition time T_r = 100 ms, time-domain match filter time constant T_m = 1 ms, acquisition time T_{daq} = 15 ms, number of averaging N_{avg} = 400000 for the non-enhanced signal and N_{avg} = 4000 for the enhanced signal.

Figure 2.13: **DNP enhancement of 2% BDPA:SEBS with respect to the magnetic field.** The oscillator is supplied with $V_{DD} = 1.8$ V and $I_{DD} = 40$ mA. The microwave excitation is always on during this measurement. The center of the ESR spectra is approximately at 370.25 mT. Measurements are performed in the following conditions: The RF excitation frequency f_{rf} is swept from 15.742 MHz to 15.828 MHz, the B_0 field is swept from 0.36975 T to 0.37175 T, pulse length $\tau_{rf} = 5$ μs, pulse repetition time $T_r = 100$ ms, time-domain match filter time constant $T_m = 1$ ms, acquisition time $T_{daq} = 15$ ms, number of averagings $N_{avg} = 4000$.

In all solid effect enhanced NMR measurements, the 10 GHz oscillator is biased at $V_{DD} = 1.8$ V and $I_{DD} = 40$ mA and it is kept on during the NMR acquisition. For the non-enhanced NMR spectra the oscillator (ESR excitation) is turned off. The magnetic field B_0, the NMR excitation (V_{TX}) and down-conversion (V_{LO}) frequencies are swept and the ESR frequency (microwave excitation) kept the same for both of the DNP enhancement curves shown in Fig. 2.13 and Fig. 2.18.

The ESR spectrum of 2% BDPA:SEBS is shown in Fig. 2.11. The oscillator is biased with $V_{DD} = 1.8$ V and $I_{DD} = 40$ mA. At this supply, the microwave magnetic field B_{1e} is around 60 μT which is strong enough to saturate the sample and causes broadening of the ESR linewidth up to around 23 G. At lower bias voltage of $V_{DD} = 0.85$ V the measured ESR linewidth is 16 G. Non-enhanced NMR and enhanced NMR spectra for the same sample are shown in Fig. 2.12. When microwaves are applied on the right side of the ESR peak ($\omega_{OS} + \omega_{OI}$) the enhancement is 20 (red curve), whereas it is -15 when the microwaves are applied on the left side of the ESR peak ($\omega_{OS} - \omega_{OI}$) (pink curve). While the non-enhanced NMR spectra are the average of $N_{avg} = 400000$ spectra obtained in 11 hours, the DNP-enhanced NMR spectra are the average of $N_{avg} = 4000$ spectra obtained in 6 minutes. The DNP enhancement curve is shown in Fig. 2.13.

The ESR spectrum of 10 mM BDPA:cis-polyisoprene is shown in Fig. 2.14. The oscillator
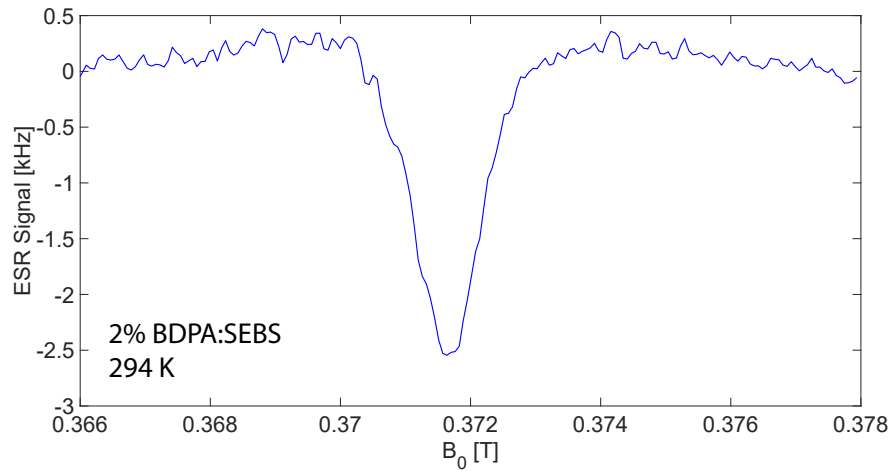
28

Figure 2.14: **ESR spectrum of 10 mM BDPA:cis-polyisoprene.** The oscillator is supplied with $V_{DD} = 1.8$ V and $I_{DD} = 40$ mA. Experimental conditions: modulation frequency $f_m = 16.789$ kHz, modulation magnetic field $B_m \cong 1.8$ mT, microwave frequency $f_{mw} \cong 10.4$ GHz, microwave magnetic field $B_{1e} \cong 60$ μT.
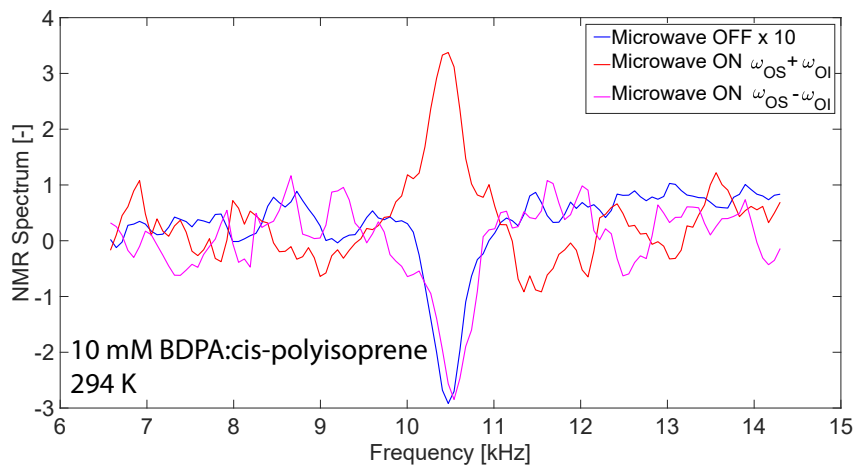
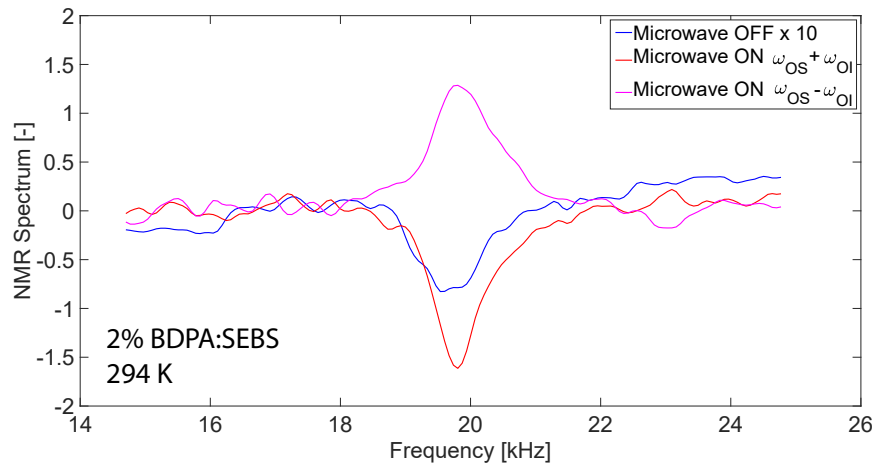
Figure 2.15: **NMR spectra of 10 mM BDPA:cis-polyisoprene.** When microwaves are applied on the right side of the ESR peak ($\omega_{OS} + \omega_{OI}$) the enhancement is 10 (red curve), whereas it is 12 when the microwaves are applied on the left side of the ESR peak ($\omega_{OS} - \omega_{OI}$) (pink curve). The NMR measurements are performed in the following conditions: $f_{rf} \cong 16$ MHz, pulse length $\tau_{rf} = 5$ μs, pulse repetition time $T_r = 500$ ms, time-domain match filter time constant $T_m = 2$ ms, acquisition time $T_{daq} = 15$ ms, number of averaging $N_{avg} = 100000$ for the non-enhanced signal and $N_{avg} = 300$ for the enhanced signal.
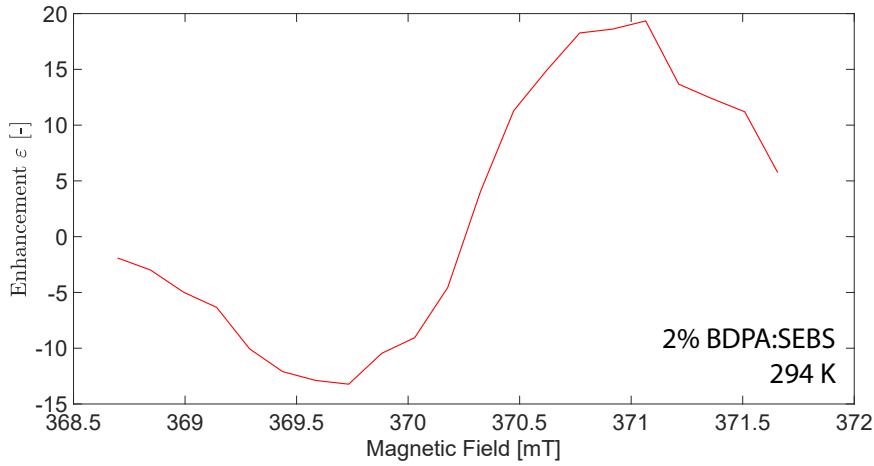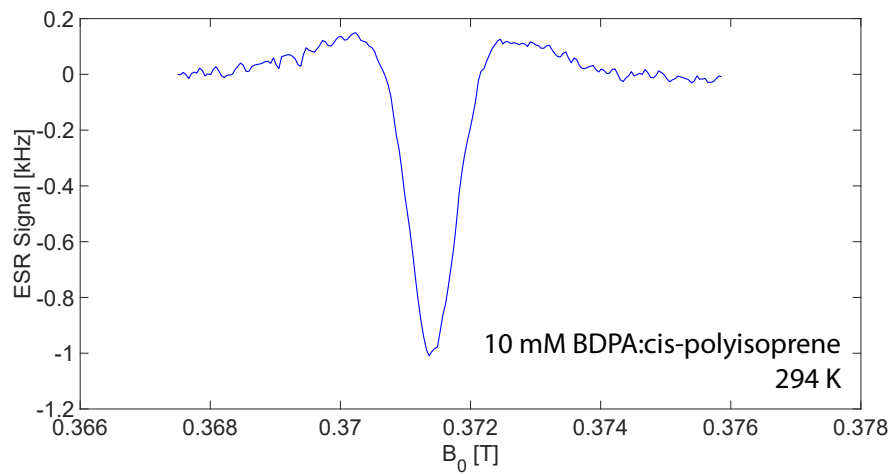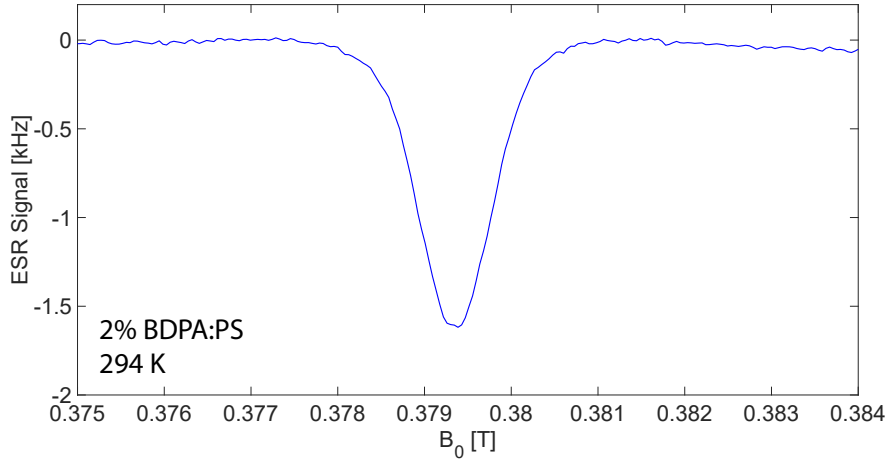
Figure 2.16: **ESR spectrum of 2% BDPA:PS.** The oscillator is supplied with V_{DD} = 1.8 V and I_{DD} = 40 mA. Experimental conditions: modulation frequency f_m =16.789 kHz, modulation magnetic field $B_m \cong$1.1 mT, microwave frequency $f_{mw} \cong$10.4 GHz, and microwave magnetic field $B_{1e} \cong$60 μT.

is biased as in the 2% BDPA:SEBS measurements. The ESR linewidth is around 14 G. Non-enhanced NMR and enhanced NMR spectra for the same sample are shown in Fig. 2.15. When microwaves are applied on the right side of the ESR peak ($\omega_{OS} + \omega_{OI}$) the enhancement is 10 (red curve), whereas it is 12 when the microwaves are applied on the left side of the ESR peak ($\omega_{OS} - \omega_{OI}$) (pink curve). While the non-enhanced NMR spectra are the average of N_{avg} = 100000 spectra obtained in 14 hours, the DNP-enhanced NMR spectra are the average of N_{avg} = 300 spectra obtained in 2.5 minutes.

At first, all the samples were doped with 2% BDPA (approximately 50 mM) and showed a linewidth of about 1.5 kHz. Even though all the samples were doped with the same concentration, significant broadening of the NMR linewidth (compared to their non-doped counterparts) is observed only in cis-polyisoprene sample at 2% concentration because it has narrower linewidth (compared to SEBS and PS) of about 300 Hz when undoped. Thus, cis-polyisoprene sample was diluted 5 times to have a final 10 mM concentration of BDPA and a linewidth of about 500 Hz.

The ESR spectrum of 2% BDPA:PS is shown in Fig. 2.16. The enhanced NMR spectra for the same sample are shown in Fig. 2.17. The NMR signal when the microwaves are off is not measured as it would need at least 40 hours of averaging to reach an SNR of 1 according to calculations of the expected signal amplitude and the measured noise. The expected signal is calculated based on the Bloch equations as explained in Ref. [30] considering the geometry of the excitation and detection coils and the sample volume. Experimentally we have
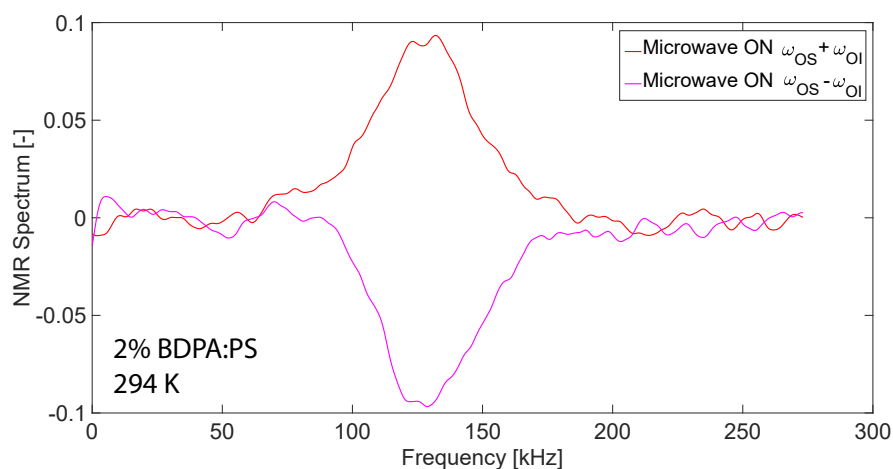
Figure 2.17: **NMR spectra of 2% BDPA:PS with microwaves.** When microwaves are applied enhancement is at least 6. The NMR signal when the microwaves are off is not measured as it needs at least 40 hours of averaging to reach an SNR of 1 according to calculations of expected signal amplitude and the measured noise. Experimentally we have observed that after 200000 averagings (i.e., 5.5 hours), the non-enhanced NMR signal is still not visible. Enhanced NMR measurements are the results of 25000 avergagings. The NMR measurements are performed in the following conditions: The RF excitation frequency $f_{rf} \cong 15.94$ MHz for the left side of the ESR peak ($\omega_{OS} - \omega_{OI}$) and $f_{rf} \cong 15.98$ MHz for the right side of the ESR peak ($\omega_{OS} + \omega_{OI}$), pulse length $\tau_{rf} = 3$ μs, pulse repetition time $T_r = 100$ ms, time-domain match filter time constant $T_m = 50$ μs, acquisition time $T_{daq} = 15$ ms, number of averaging $N_{avg} = 4000$ for the enhanced signal.
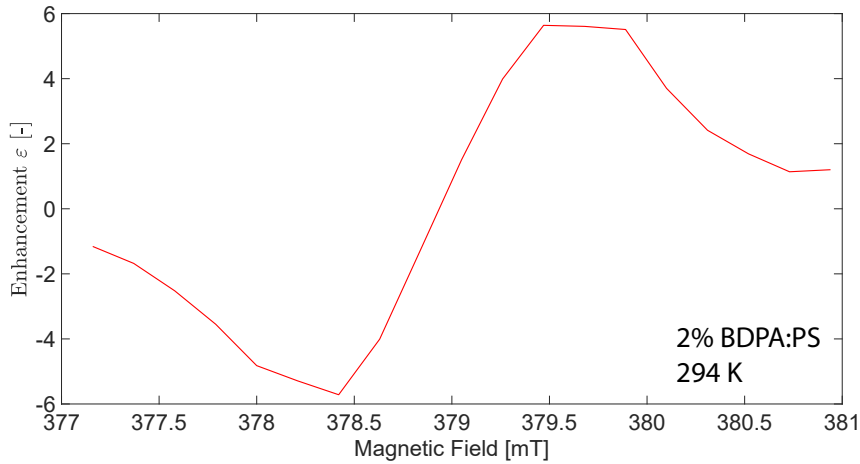
Figure 2.18: **DNP enhancement of 2% BDPA:PS with respect to the magnetic field.** The oscillator is supplied with $V_{DD} = 1.8$ V and $I_{DD} = 40$ mA. Microwave excitation is always on during this measurement and center of the ESR spectra is approximately at 379 mT. Measurements are performed in the following conditions: the RF excitation frequency f_{rf} is swept from 16.051 MHz to 16.221 MHz, the B_0 field is swept from 0.377 T to 0.381 T, pulse length $\tau_{rf} = 3$ μs, pulse repetition time $T_r = 100$ ms, time-domain match filter time constant $T_m = 50$ μs, acquisition time $T_{daq} = 15$ ms, number of averagings $N_{avg} = 25000$.

observed that after 200000 averagings (i.e., 5.5 hours), the non-enhanced NMR signal is still not visible. The DNP enhancement curve is shown in Fig. 2.18. Here, for the non-enhanced NMR signal the noise level is used, which results in an underestimation of the enhancement. The DNP-enhanced NMR spectrum is the average of $N_{avg} = 4000$ spectra and is obtained in 6 minutes. Solid effect enhancements up to 100 are reported on the same sample with NOVEL method [141]. Pulsed DNP experiments might enable larger enhancements using the frequency tunability of the single chip DNP microsystems. An experimental scheme to perform pseudo-pulsed ESR measurements with frequency tunable single chip ESR detectors is reported in Ref. [142].

2.7 ESR experiments at cryogenic temperatures

ESR measurements at cryogenic temperatures have been performed to show the possibility to use this single chip DNP microsystem also at low temperatures. ESR spectra of 2% BDPA:PS at 180 K and 15 K are shown in Fig. 2.19 and Fig. 2.20, respectively. The ESR spectrum at 180 K (Fig. 2.19) has lower amplitude (approximately 0.6 kHz) compared to the ESR spectra (approximately 1.5 kHz) at 294 K (Fig. 2.16). One of the reasons behind this phenomena is the effect of O_2. The ESR measurement at 294 K is performed in air whereas the one at 180 K is

Figure 2.19: **ESR spectrum of 2% BDPA:PS at 180 K.** The oscillator is supplied with $V_{DD} = 1.8$ V and $I_{DD} = 40$ mA. Experimental conditions: modulation magnetic field $B_m \cong 1.1$ mT, and modulation frequency $f_m = 16.789$ kHz.

performed in He atmosphere after the removal of O_2. After the O_2 removal, a five times signal amplitude reduction is observed in ESR spectra of 2% BDPA:PS.

As the temperature decreases from 180 K to 15 K, the signal amplitude increases from 0.6 kHz to 2.5 kHz. This increase is less than the expected one by the Curie law [143] which is 12 times. It can be attributed to two phenomena: 1) the microwave magnetic field B_{1e} generated by the ESR oscillator increases as the temperature decreases, 2) the relaxation times of the sample are longer at lower temperatures which results in easier saturation of the sample. The microwave magnetic field B_{1e} increases as the temperature decreases because the power consumption of the oscillator and the microwave current in the ESR microcoil increases. This is mostly attributed to the carrier mobility increase in the transistor [144]. As a consequence, B_{1e} generated by the oscillator increases, causing larger sample saturation.

NMR and enhanced-NMR spectra have not been measured yet, but the low temperature ESR measurements are promising also for low temperature DNP experiments with this single chip 10 GHz DNP microsystem.
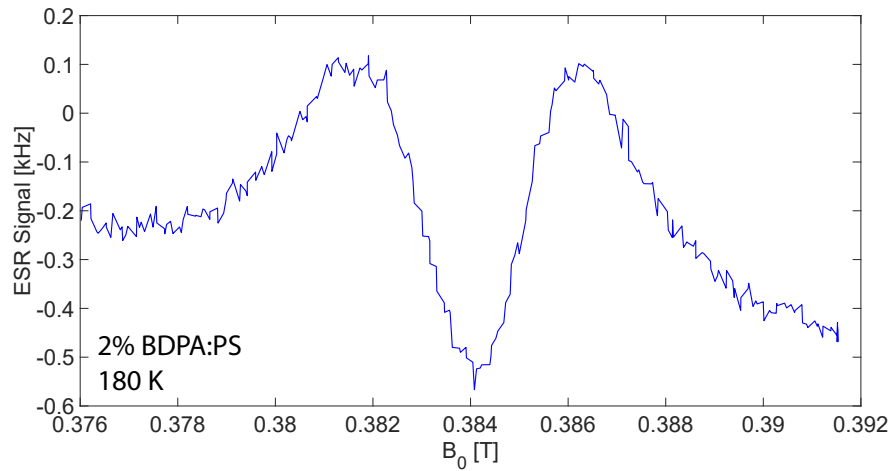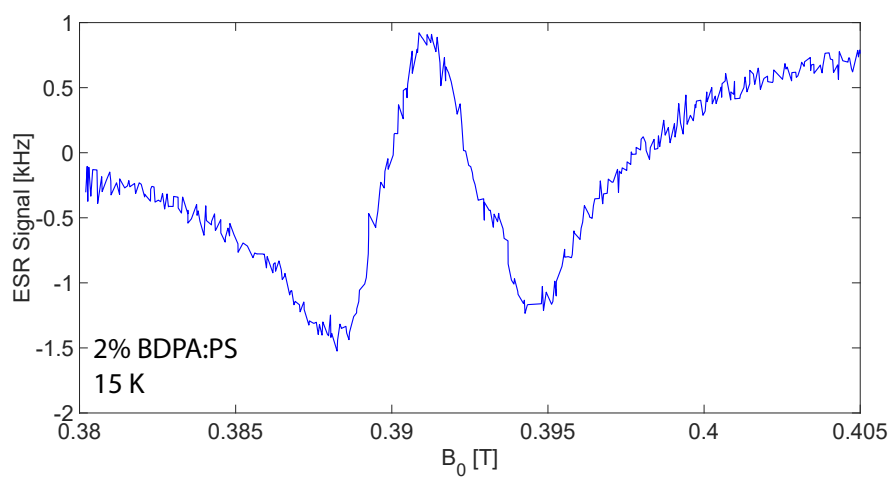
Figure 2.20: **ESR spectrum of 2% BDPA:PS at 15 K.** The oscillator is supplied with $V_{DD} = 1.8$ V and $I_{DD} = 40$ mA. Experimental conditions: modulation magnetic field $B_m \cong 1.1$ mT, and modulation frequency $f_m = 16.789$ kHz.

3 Single chip 200 GHz DNP microsystems

The single chip integration of the sensitivity relevant part of nuclear magnetic resonance (NMR), electron spin resonance (ESR), and dynamic nuclear polarization (DNP) enhanced NMR detectors is a promising approach to improve the limit of detection, especially for nanoliter and subnanoliter samples. A single chip DNP microsystem operating at 11 GHz (ESR)/16 MHz (NMR) has been demonstrated in section 2. Here, we report on a single chip DNP microsystem operating at 200 GHz (ESR)/300 MHz(NMR). The single chip integrated microsystem consists of a microwave oscillator operating at about 200 GHz for ESR excitation/detection and of a radio frequency receiver operating at about 300 MHz with frequency downconversion for NMR detection. The proposed microsystem eliminates the need of a high power microwave generator (e.g. a gyrotron) and high quality microwave wave guides for DNP experiments. Additionally, it works from 300 K down to at least 15 K because of the intrinsic capabilities of the chosen integrated circuit technology. The NMR excitation is performed with a non-integrated coil. To exemplify its possible applications, ^{1}H DNP enhanced NMR experiments on solid samples of volumes from 125 pL to 2 nL are performed at temperatures from 15 K to 300 K. DNP enhancements as large as 50 are achieved with 2% α,γ-bisdiphenylene-β-phenylallyl in polystyrene (2% BDPA:PS) at 15 K. This work demonstrates the possibility to extend the single chip approach to the realization of probes for DNP studies of nanoliter and subnanoliter samples at high frequency, high field, and low temperature.

3.1 Introduction

Nuclear magnetic resonance (NMR) methods are a powerful tool employed in many research fields, including physics, chemistry, material science, biology, and medicine. Their importance for industrial and clinical applications is also widely recognized such as industrial process monitoring and magnetic resonance imaging (MRI). The use of NMR methodologies for an even wider range of studies is often hindered by the low signal-to-noise ratio (SNR) achievable in the available experimental time. An approach to increase the SNR, applicable to samples of any volume, is to increase the nuclear spin polarization (hyperpolarization), e.g., by microwave, optical, and chemistry-based methodologies [7, 100–110, 125, 126]. Dynamic nuclear

35

polarization (DNP) is one of the most powerful and versatile methods to improve the SNR in NMR experiments [3, 7, 145–147]. Microwave driven DNP methods employ a microwave magnetic field which excites the unpaired electrons (added or, rarely, naturally present) in the sample under investigation into electron spin resonance (ESR). The ESR excitation of the unpaired electrons increases the polarization of the nearby nuclear spins well above the thermal equilibrium value, producing an effective increase in the SNR up to 660 for ^{1}H nuclei (and more for nuclei with a lower gyromagnetic ratio). DNP enhanced NMR experiments are performed in wide range of magnetic fields, from zero to more than 20 T [7, 125, 148–151]. As for non-DNP enhanced NMR spectroscopy, operation at higher magnetic fields allows for larger thermal spin polarization that increases SNR and larger chemical shifts that increase the spectral information content. Despite the reduction in the DNP enhancements generally observed at higher magnetic fields, the previous two advantages makes the exploration of DNP methods at high fields interesting and potentially impactful. High field DNP provides information that is otherwise not available, for example in solid state NMR alone [8]. Conventional high field DNP methodologies require the use of relatively expensive and bulky microwave/quasi-optical sources and waveguides [150, 152, 153], which reduces their widespread use.

During the last two decades, the separate integration on a single chip of the front-end electronics of inductive NMR spectrometers [34, 41, 42, 44, 45, 47–57, 154] as well as ESR spectrometers [72–74, 93–96, 99, 155] have been demonstrated. Recently, the co-integration on a single silicon chip of the front-end electronics of an NMR and an ESR detector has been demonstrated [46]. This combination of sensors allowed to perform DNP experiments at 10.7 GHz (ESR)/16 MHz(NMR) using a single chip integrated microsystem of about 2 mm^2. Overhauser DNP experiments in liquid samples of TEMPOL/H$_2$0 at room temperature with NMR enhancements as large as -50 has been reported. Details of this microsystem is explained in chapter 2.

Due to the strong motivations to operate at higher static magnetic fields described above, in this work we designed and characterized a single chip integrated DNP microsystem operating 200 GHz (ESR)/300 MHz (NMR). The realized single chip microsystem generates microwave magnetic fields at 200 GHz, allows to performs continuous wave ESR experiments by field or frequency sweeps, and to perform NMR and DNP enhanced NMR experiments. The integration of the microwave source and ESR detector together with the NMR sensor allows to study DNP enhanced NMR without the need of an external microwave source and connections to carry the microwave signals such as waveguides. All the connections to/out of the magnet, where the microwave excitation and ESR detection occurs on chip, are DC. As a result, these single chip integrated ESR, NMR, and DNP-NMR detectors are suitable for the miniaturization of the probe, for the reduction of the losses and complexity of the connections, and for the realization of dense arrays of detectors for parallel (simultaneous) spectroscopy of several samples. Additionally, the single chip approach might allow for a better SNR for volume limited samples in the nanoliter and subnanoliter range tightly matched to the sensitive volume of the detector with respect to the conventional bulky inductive probes which are optimized for microliter and larger sample volumes. By suppressing the need for external microwave sources

and microwave connections, the single chip approach proposed here reduce drastically the cost and the complexity of the DNP instrumentation and, hence, should allow for a more widespread use and study of DNP methologies on nanoliter and subnanoliter samples.

In this chapter, a 200 GHz DNP microsystem and a 200 GHz DNP array microsystem are presented from design to measurement results. ESR and NMR detector designs are explained starting from the technology selection. Design criteria, co-integration of ESR and NMR detectors, simulation methods, sample preparation, measurement setups, and measurement results are reported and discussed.

3.2   Technology selection

There are several important specifications that should be considered in the technology selection for a custom integrated circuit design. Since it is hardly possible to design a circuit without trade-offs, it is crucial to set the most important criteria in the circuit. For the NMR detector the criteria are 1) noise, 2) deadtime (wideband low frequency amplifier), 3) gain, 4) power consumption, 5) low temperature operation, from the most important to least important. For the ESR detector, they can be ordered as 1) frequency, 2) microwave magnetic field B_{1e}, 3) power consumption, 4) low temperature operation. For the 200 GHz DNP microsystem design, the most important criteria can be listed as:

1. **Operation frequency.** High field DNP experiments are performed with costly equipments, thus the goal is to perform DNP experiments without them. Previously we have shown a 10 GHz DNP system and we aim to increase the frequency at least an order of magnitude. We have selected 200 GHz because of the availability of a 7 T magnet in our laboratory.

2. **High microwave magnetic field amplitude** B_{1e}**.** High B_{1e} is important especially for high field DNP. It has been shown that at high field solid effect enhancements are larger than Overhauser, but solid effect requires larger microwave B_{1e} [7]. Additionally, in our previous 10 GHz system, it has been observed that the Overhauser enhancements were also not saturated.

3. **Low temperature operation.** Low temperature operation is necessary to increase the versatility of the system, and because the majority of the solid effect experiments are performed at low temperatures. Due to the generally longer longitudinal relaxation time of electron (T_{1e}), it is easier to saturate ESR transitions at low temperatures, hence it is easier to achieve higher enhancements at lower temperatures [7].

Although the aforementioned criteria are the most important ones, the list is not exhaustive for the success of the 200 GHz DNP microsystem. It is important to have a low noise and wide band receiver to perform NMR experiments. Noise of the integrated NMR receiver depends

Table 3.1: Integrated circuit technology comparison table (room temperature).

	TSMC	ST FD-SOI	IHP SiGe:C	IHP SiGe:C(Cu)
	40 nm	28 nm	130 nm	130 nm
f_T [GHz]	360 (260 for miniasic)	320	300	300
f_{max} [GHz]	200	320	500	500
Number of thick metals	2	2	2	3
R$_{sh}$ [mΩ/sq]	18	19	11	11
	22	19	18	6
				6

on the planar microcoil because of the high sheet resistance of the available metal layers in integrated circuit technologies. As a consequence, one of the most important specifications for integrated NMR detectors with integrated microcoils are the sheet resistance (R_{sh}) of available metal layers in the technology (see Table 3.1). This is explained in details in section 3.4.

Another important specification is the power consumption of the NMR circuitry. NMR receiver consists of building blocks that would consume large powers, especially the low noise amplifier (LNA). To design a low noise LNA, it is necessary to have enough power budget, because transistor's noise performance is not good enough at low power consumptions. Giving LNA enough power budget means restriction of power budget in the following stages. Fortunately CMOS technology is optimized in terms of power consumptions. So, it is important to have the power of CMOS technology available in the technology. This is a very important quality of SiGe:BiCMOS (SiGe:C) technologies. In the building blocks where the performance has more importance over the power consumption, heterojunction bipolar transistors (HBT) are selected for the design and in other building blocks where the power consumption is more critical, CMOS devices are selected. This is explained in details in section 3.4.

An IC technology comparison is shown in Table 3.1. f_T is the transit frequency (cut-off or gain-bandwidth) of the transistors. It defines the frequency at which the current gain of the transistor drops to zero. TSMC 40 nm shows the highest f_T but it is not provided for "miniasic" program which allows universities to access the technology at a reduced price. f_{max} is the maximum oscillation frequency of the transistor. It defines the maximum frequency to get a power gain out of the transistor. IHP SiGe:C technologies offer the highest f_{max}. R_{sh} is the sheet resistance of the thick metal layers available in the technology. In the first row, thickness of the top layer is given. In the second and third rows, thicknesses of the second and third layers from the top are given. The IHP SiGe:C(Cu) technology offers the lowest R_{sh} and an extra thick metal layer for inductors with higher quality factors. High f_T and f_{max} frequencies are required for high frequency oscillators (i.e. ESR detector) and low R_{sh} is required for microcoils with less noise (i.e. NMR microcoil of NMR receiver).

The Silicon Germanium (SiGe) technology is chosen mainly for operating frequency, cryogenic

temperature performance, large oscillation capacity of transistors and cost. Oscillators with operation frequencies at around 200 GHz in SiGe HBT technology have been previously reported [79–90]. Their highly doped Ge emitter allows both high current gain and high cut off frequency. SiGe HBT devices offer higher gain at relatively higher current compared to CMOS transistors. Higher current allows for higher oscillation amplitude. The cost of SiGe HBT technology is similar if not lower compared to a CMOS technology that would allow a similar cutoff frequency. Moreover, the SiGe technology is adapted and optimized for low temperature operation. The potential of SiGe HBTs have been extensively studied by Cressler [156], showing that SiGe HBT devices are promising for cryogenic circuit design. As stated in this work, cooling these devices improves the critical properties such as current gain (β) and cut-off frequency (f_T). Moreover, the technology offers additional localized backside etching (LBE) and through silicon via (TSV). LBE increases the quality factor of inductors, up to a factor of two at 5 GHz. TSV reduces the ground inductance which has high importance in microwave design. As these add-on processes have extra cost, we have not implemented them in the first prototype of our system. However, these extra costs per chip would be reduced in the mass production of such probes.

3.3   ESR detector

The ESR detector consists of a 200 GHz voltage controlled oscillator (VCO) with an oscillation amplitude detection output (see Fig. 3.1). The ESR phenomenon produces a variation of the oscillation frequency and of the oscillation amplitude of the oscillator [94]. In the case where the high frequency signals (especially at frequencies larger than 10 GHz) are transfered out of the magnet, signal quality is deteriorated because of large losses in long cables. Hence it becomes very important to manipulate the signal locally on chip especially at 200 GHz. Since the ESR phenomenon creates both frequency and amplitude variations, either a frequency down-conversion circuit or an amplitude detection circuit are possible. In this work, we have decided to use amplitude detection mainly because of the simplicity of the circuit.

The DC component of the voltage at the V_{ESR} node (see Fig. 3.1) is proportional to the amplitude of the oscillations. This property has first been shown in cross-coupled CMOS LC VCOs [157] and used for ESR detection based on the same type of oscillators [97, 158, 159]. Since it is based on the differential working principle of cross-coupled VCOs, we predicted that the same principle applies also to differential Colpitts oscillators. The freedom of voltage variation in the center of L_B inductors is assured by the current biasing in the same node (I_B) through a biasing resistor R_P. The amplitude-encoded signal on the V_{ESR} node is transfered out of the chip through an RF decoupling inductor L_P.

Here is the step-by-step procedure followed for oscillator design:

1. **Decision on the topology.** The most common topology used for SiGe oscillators in 200 GHz operation range is the differential Colpitts topology [79–90]. The design of the
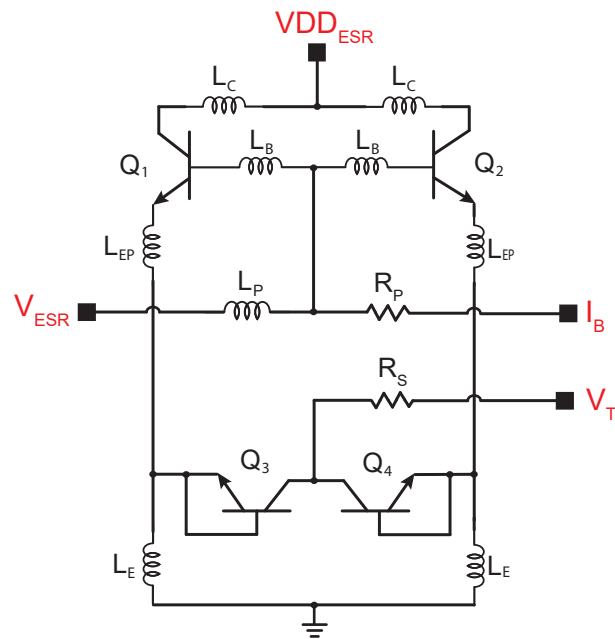
Figure 3.1: **Schematic of the 200 GHz ESR detector.** The gate width and the emitter length of Q_1, Q_2, Q_3 and Q_4 transistors are 70 nm and 900 nm respectively. The number of emitters for Q_1 and Q_2 transistors is 6, whereas for Q_3 and Q_4 transistors is 5. R_S and R_P resistors are 280 Ω and 18 kΩ. The L_B inductor is the excitation/detection coil of the ESR detector. VDD_{ESR} is the supply voltage, I_B is the supply current, V_T is the tuning voltage and V_{ESR} is the output of the ESR oscillator.

oscillator we realized is based on the work by Voinigescu et al. [82]. As also suggested in their work, the oscillator is simulated in two different forms: 1) regular "oscillator configuration" where the oscillation frequency, amplitude and microwave current in the L_B inductor are maximized, 2) "amplifier configuration" (or negative gain configuration) to optimize components (e.g. inductors, transistors, varactors) and to make sure there are no other frequencies where the oscillation condition (Barkhausen criteria) is met. While the importance of the first one is obvious, the second one is also very useful to the designer in understanding the effect of changes in each component.

2. **"Amplifier configuration" simulation (small signal - AC simulation).** Even though oscillators work in large signal mode, small signal simulations provide key information in the design of oscillators. For this simulation, the oscillator feedback is broken and it is simulated as an amplifier as in Fig. 3.2. In this simulation, the real and imaginary parts of the input impedance are computed. There should be only one zero crossing of the imaginary part while the real part is negative. This allows us to make sure there will be only one oscillation frequency possible. All DC voltages, currents, and component values can be decided for 200 GHz oscillations at this step.

3. **Optimization of transistor size, bias voltages and component values for Barkhausen criteria.** The design starts using the values given in the work [82] and using the maximum number of emitters in the transistor. In the initial simulations only the transistors have real model files, all the other components are ideal with reasonable assumptions of the parasitics. For example, L_B inductor is chosen as 7 pH and a series resistance of 1 Ω is assumed. After these simulations, there is already a rough design of oscillator. However, schematic design is only the starting point of the circuit design at 200 GHz. It is important to simulate all connections with electromagnetic (EM) simulations. Following the previous example, it is seen that the series resistance of the L_B inductor varies between some mΩ to 1.5 Ω from DC to 200 GHz. Using the EM simulation in the circuit simulation is crucial in microwave oscillator design (details will be explained later in this section). The oscillation frequency is determined by the L_B inductors and the parasitic capacitances of Q_1, Q_2, Q_3 and Q_4 transistors. The transistor of highest f_T is chosen from the technology. This transistor size cannot be changed but the number of emitters can be changed. The number of emitters of the Q_1 and Q_2 transistors are optimized with two main criteria: 1) enough gain to sustain oscillations and 2) frequency of operation. The larger the number of emitters the larger the gain and the lower the frequency of operation. The number of emitters of Q_3 and Q_4 transistors are optimized to obtain the desired oscillation frequency and large enough tuning range. Even though their effect is not pronounced as a first order effect, inductors L_C, L_{EP} and L_E also effect the operation frequency. So, a full circuit simulation is necessary to obtain the desired oscillation frequency.

4. **"Oscillator configuration" simulation (large signal - transient simulation).** This simulation is performed for the optimization of the oscillation frequency, amplitude and microwave current in the L_B inductor.

5. **Layout.** The layout design starts with the design of the L_B, L_E and L_C inductors. After the separate simulation results converge to the desired values, combination of these inductors are simulated. More components are added in each iteration until the final layout is reached. For example, you would start only with three inductors, then you would draw the transistor connections. This would introduce the inductance of L_{EP} and parasitic capacitances, resistances and inductors at transistor nodes because of vias. At 200 GHz, a via has a non-negligible inductance.

6. **EM simulation.** ADS (Advanced Design System, Keysight) software is used to perform EM simulations and extract the S-parameters file. This file contains the high frequency characterization of the metal lines and can be imported to the circuit design software (EDA software), in our case Cadence. Model files of the technology are provided by the foundry and are imported to Cadence. Combination of technology model files with S-parameters files from ADS enables accurate simulations. Design of a 200 GHz oscillator requires EM simulation files that contains data at least up to 400 GHz. EM simulations up to 400 GHz is very time consuming, and even impossible without simplifications such as via merging, modelling vias not 3D but as wire connections, and removing some complex connections that are not critical for high frequency behaviour. A second important method for layout simplification in EM simulation is to simulate some layout parts separately. In this design, the vias and connections to transistors are simulated separately, and their inductance, resistance, and capacitance are added as separate parasitics components to the oscillator simulations. This manipulation saves significant amount of simulation time as these connections mostly are not redesigned in each iteration.

7. **Back to step 2 and 4.** Combining EM simulations output with circuit simulation in Cadence enables a good post layout simulation. At this step, iterations of circuit and layout optimization is performed. Once the desired result is achieved in both simulations (in step 2 and 4) of the final layout, the design is finished.

The oscillator design for high spin sensitivity ESR detection and effective DNP excitation goes in opposite directions. High frequency oscillators require low microwave magnetic field B_{1e} for high spin sensitivity, hence low power consumption. The low B_{1e} is desired to avoid saturation of samples having long spin relaxation times and to maintain low 1/f noise in the oscillator, which is the dominant noise type in high frequency oscillators. On the other hand, ESR oscillators for DNP excitations are optimized for large microwave magnetic field B_{1e}, hence high power consumption. SiGe technology is chosen for the DNP application mainly because of its high power capability at high frequency as explained in the previous section (see section 3.2). High oscillation amplitude in the resonator is required to be able to saturate the ESR transitions in the samples.

The oscillator frequency is variable by the tuning voltage V_T. Varactors that are available in the technology are too large for the target frequency of 200 GHz. For this reason, Q_3 and Q_4 HBTs
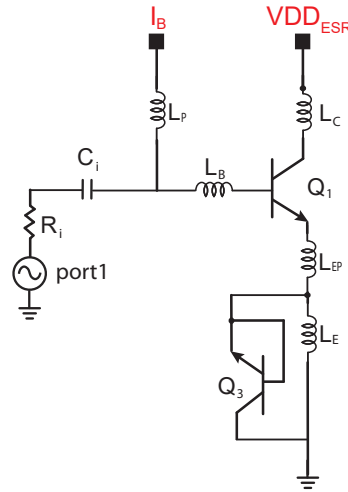
Figure 3.2: **Amplifier configuration of the ESR oscillator.** R_i is set as 1 Ω to reflect the expected effective resistance of the L_B inductor [82]. C_i should be large and is chosen as 5 nF. S-parameter simulation is performed and Z_{11} parameter is extracted from S_{11} parameter. Oscillation condition is met when imaginary part of Z_{11} crosses zero where the real part of Z_{11} is negative. This condition should be met only once and at 200 GHz.

(same as Q_1 and Q_2 but different in size) are used to form variable capacitors as suggested also in [82]. The frequency variability of the oscillator allows to perform ESR experiments with a frequency sweep rather than a magnetic field sweep [95]. The frequency tuning range of the oscillator is 8 GHz. The frequency can be changed up to 3 GHz by changing the tuning voltage (V_T) between -0.5 V and 2 V (see Fig. 3.15). An additional 5 GHz tuning is achieved by adjusting the supply current I_B and the supply voltage V_{DDESR}. The oscillator frequency also depends on the operating temperature. The VCO frequency increases approximately linearly as the temperature decreases, with central frequency of 190 GHz at room temperature and 200 GHz at 10 K.

The oscillator operates with a supply voltage (V_{DDESR}) range of 1 to 1.5 V and a supply current (I_B) range from 6 to 70 μA and consumes 5 to 24 mA. Since the microwave magnetic field B_{1e} is generated on chip by the oscillator and the ESR signal is encoded as DC signal, no microwave connections are necessary (all signals from/to the single chip ESR detector are DC). In this work, we recorded the ESR spectra by measuring the oscillation amplitude variation as explained previously. Standard magnetic field modulation and lock-in demodulation is used to improve the signal-to-noise ratio (see discussion in Section 3.7.2). The maximum microwave magnetic field B_{1e} in the center of the ESR microcoil is calculated as 2.75 G with the equation $B_{1e} = \mu_0 I_{RF}/4D_{in}$, where the peak-to-peak simulated RF current I_{RF} in the ESR microcoil is 35 mA and D_{in} is the inner diameter of the microcoil.
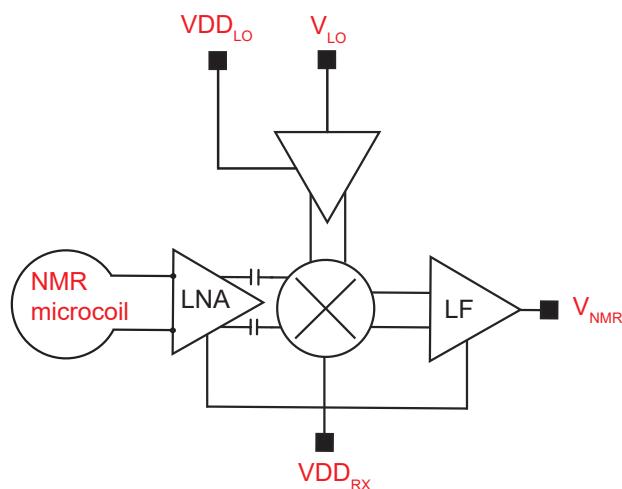
Figure 3.3: **Block diagram of the NMR receiver.** It is a heterodyne receiver consisting of LNA, mixer and a low frequency amplifier. The local oscillator signal V_{LO} is splitted and amplified to drive the differential mixer.

3.4 NMR detector

The NMR detector is a receiver-only chain with 75 dB overall gain, consisting of a microcoil, a broadband low noise amplifier (LNA) operating up to 1 GHz, a mixer, and a low frequency (LF) amplifier with a 4 MHz bandwidth (see Fig. 3.3). An external coil is used for NMR excitation (see Figs. 3.12(a), (d), 3.13(b), and additional details in section 3.7.2).

The design of the NMR detector starts with the detection coil (see the photograph of the NMR microcoil in Fig. 3.8(c)). Here, the NMR microcoil design is explained step-by-step:

1. **Coil diameter.** In most of the designs, the coil diameter is chosen according to the sample volume. In this work, it is chosen according to the ESR excitation coil. A distance of at least the diameter of the ESR microcoil should be kept from the ESR microcoil to the inner diameter of the NMR microcoil to avoid a significant perturbation of the ESR oscillator. The NMR microcoil diameter is not increased any further as the goal is to perform DNP experiments on samples with a large fraction of their volume which is efficiently hyperpolarized by the ESR excitation.

2. **Number of turns.** The NMR signal is proportional to the number of turns in the NMR microcoil, and the noise is proportional to square-root of series resistance ($\sqrt{R_s}$) of the NMR microcoil. The design strategy is as follows: 1) maximize the intrinsic signal-to-noise ratio (SNR) at coil ends with attention to keep the self resonance frequency above the operating frequency, 2) design an LNA that do not significantly deteriorate this intrinsic SNR. Number of turns, wire width, spacing between wires and the inner diameter determine the outer diameter of the NMR microcoil. The outer diameter of

the NMR microcoil is kept in moderate size to avoid increasing the aspect ratio of the NMR and ESR microcoil diameters. Thus, number of turns is limited to 21 for two main reasons: 1) to avoid a large aspect ratio of the NMR and ESR microcoil diameters and 2) to keep a safety margin with the operating frequency and the self resonance frequency of the NMR microcoil.

3. **Broadband or tuned approach decision.** This step goes together with the previous step, because the broadband or tuned approach decision would be taken according to the quality factor of the microcoil. The quality factor (Q) of a coil is defined as $Q = \omega L/R_s$, where $\omega = 2\pi f$, f is the frequency and L is the inductance of the resulting microcoil. If the Q factor of the coil is high, the coil can be tuned by tuning and matching capacitors, and the signal and the noise of the coil would be intrinsically amplified before the low noise amplifier. This approach would be especially interesting for reducing the requirements on the LNA, as it would not be required to have a very low noise. However, if the Q factor cannot be made high, for example because of the high sheet resistance of available metals of the integrated circuit technology, tuning and matching would both not be very effective (gain of this amplification would be low), and the noise of the microcoil would already be high and leave a more relaxed LNA design in terms of input equivalent noise.

4. **EM simulation.** Once the design of the coil is finalized, it is important to simulate the microcoil in an EM simulator as it was done for the ESR microcoil in section 3.3. This simulation take much less time compared to the ESR microcoil simulation and give values very close to the calculated ones because of the lower frequency operation. It is critical to make sure that the self resonance frequency of the NMR microcoil, which is extracted from the EM simulation, is above the desired operation frequency.

Even though the selected SiGe technology has three thick metal layers, the sheet resistance of these metal layers are still not low enough to achieve high-Q factor coils. As a result a broadband approach is chosen, with the potential advantage of studying different nuclei or operating at different fields with the same NMR detector. Once this decision is made, the number of turns are increased until the SNR is maximized at the NMR microcoil ends. Finally, the NMR detection microcoil is realized with the three thick top metal layers available in the technology. It has an external diameter of 200 μm (250 μm for the microsystem with four microwave oscillators inside the NMR microcoil), a wire width of 5 μm, a wire thickness of around 3 μm, a spacing between the wires of 2.8 μm, and a total number of turns of 21 with 7 turns in each layer. The computed values for the inductance and the series resistance of the resulting NMR microcoil at the operating frequency of 300 MHz are 79 nH and 24 Ω for the 200 μm microcoil.

The NMR microcoil is connected to the LNA directly (i.e. without tuning/matching capacitors). The schematic of the LNA is shown in Fig. 3.4. A differential design is chosen for the LNA and for the complete receiver architecture to have a higher immunity against noise and
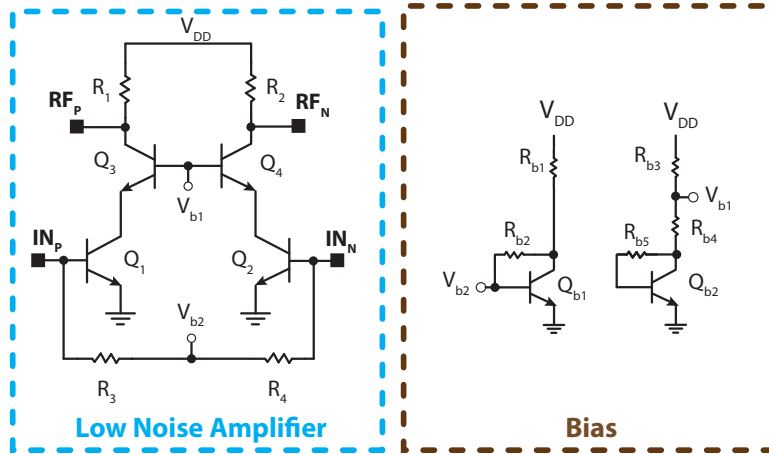
Figure 3.4: **Schematic of the low noise RF amplifier.** A differential cascode topology is used in the LNA design.

interferences [160]. The LNA is designed to amplify the signal without significantly impacting the SNR. The gain of the LNA is limited to 28 dB to avoid possible oscillations. Cascode topology is chosen to achieve higher gain without additional power consumption and noise deterioration [161]. The LNA operates from DC to 1 GHz and a total input referred noise of 0.8 nV/Hz$^{1/2}$ including the microcoil and the input impedance of 1.5 kΩ.

The LNA is connected to the down conversion mixer with decoupling capacitors which sets the minimum operating frequency of the receiver chain to 15 MHz. A double balanced mixer is used to down convert the signal. Down-conversion is important to reduce the output signal frequency and to be able to add an additionaly LF amplifier to increase the immunity against noise and interferences along the cables. The local oscillator (LO) signal is used for the down conversion and brought to the chip from outside of the magnet. It is amplified and separated into two signals which have 180° phase shift by an inverter chain amplifier. See Fig. 3.3 for the connection to the mixer and Fig. 3.5 for the block diagram of LO signal amplification. The output of the mixer is directly connected to the LF amplifier which further amplifies the signal.

The LF amplifier is designed to drive low impedance loads and have further amplification in the receiver chain such that the signal and noise is not deteriorated along the cables. The LF amplifier consists of an OPAMP that is designed in the Miller OTA topology. A resistive feedback is used to set the gain of the LF amplifier as shown in Fig. 3.6. Fig. 3.7 shows the current source used in the OPAMP. The LF amplifier has a bandwidth of 4 MHz and a low output impedance of 15 Ω. The large LF bandwidth is important for experiments on solid samples having short T_2^* which require a receiver chain with short dead-times after the excitation pulse. The measured deadtime is about 1 μs. The total input referred noise of the receiver is about 1 nV/Hz$^{1/2}$ in the post layout simulation and the worst corner. The spin sensitivity of the NMR receiver is 10^{13} spins/Hz$^{1/2}$ at 300 MHz and room temperature. It is calculated as $N_{min} = V_s N_s V SD / S_O$ where V_s is the sample volume in m^3, N_s is the spin density spins/m^3, $V SD$ is the voltage
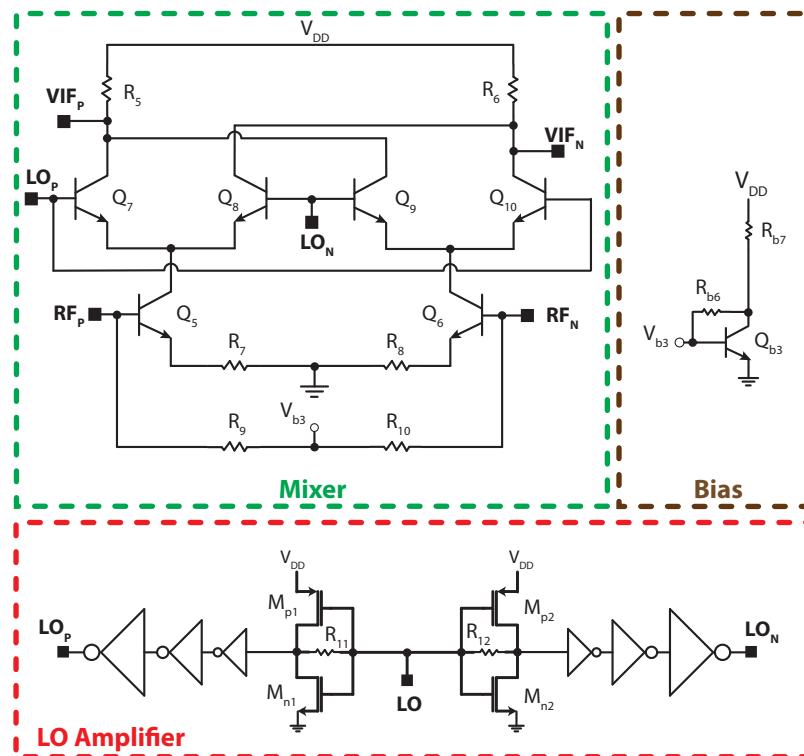
Figure 3.5: **Schematic of the mixer and LO signal amplifier.** The down conversion mixer is designed in Gilbert cell topology. The LO signal is splitted and amplified. R_{11} and R_{12} resistors are biasing the DC voltage at the inputs of the first amplifier stage.
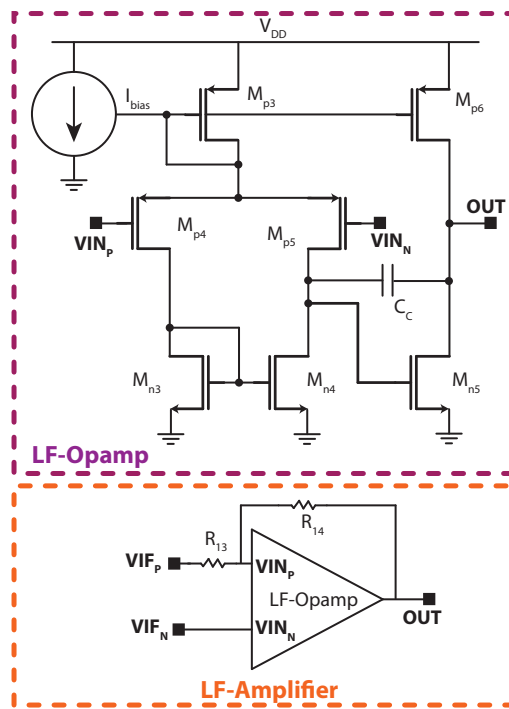
Figure 3.6: **Schematic of the low frequency amplifier.** The OPAMP is designed in Miller OTA topology and simple resistive feedback is used to limit the gain and enhance the bandwidth. The details of the current source is given in Fig. 3.7.
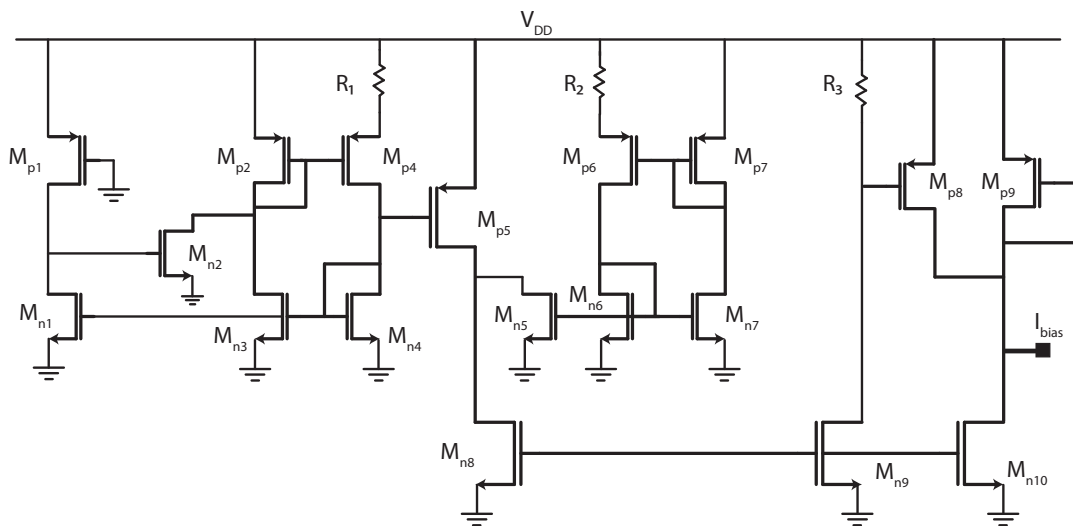
Figure 3.7: **Schematic of the current source used in the low frequency amplifier.**
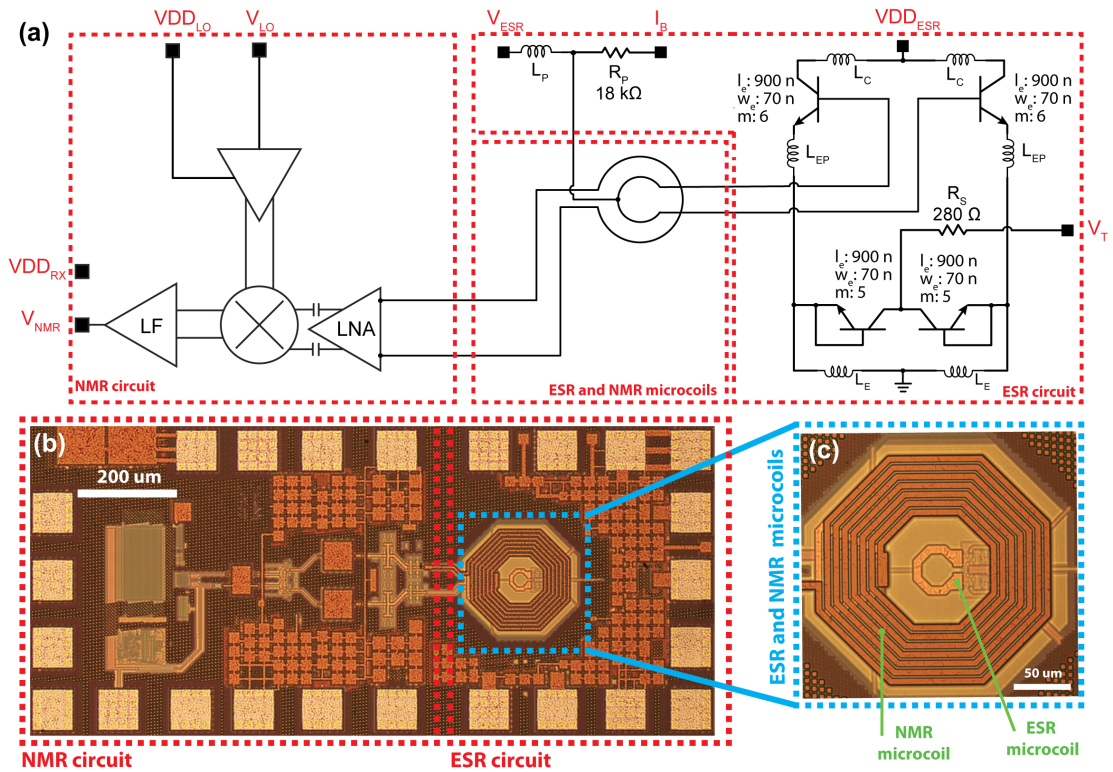
Figure 3.8: **The single chip integrated DNP microsystem operating at 200 GHz(ESR)/300 MHz(NMR). (a)** Schematic of the single chip DNP microsystem. The dashed red lines indicate the NMR/ESR circuits and the concentric NMR/ESR microcoils. The black squares next to the port names represent the bonding pads. VDD_{RX} is connected to several nets and the connections are not shown in the schematic for simplicity. VDD_{RX} is the supply voltage of all the blocks in the receiver of the NMR circuit. **(b)** Photograph of the single chip DNP microsystem. The blue line indicates the concentric NMR/ESR microcoils. The dashed red lines indicate the NMR/ESR circuits as in (a). **(c)** Photograph of the NMR and ESR microcoils. The ESR microcoil has a single turn and an external diameter of 45 μm. The NMR microcoil has 21 turns (7 turns in each of the three top metal layers) and an external diameter of 200 μm.

noise spectral density at the output of the chip in V/Hz$^{1/2}$ and S_O is the signal at the output of the chip in V. The spin sensitivity is improved by the factor of enhancement in the case of DNP enhanced NMR experiments.

3.5 Co-integration of ESR and NMR detectors

The main concern in the co-integration is the placement of the ESR and NMR microcoils. The NMR microcoil is designed such as the inner diameter is at least twice as much the outer diameter of ESR microcoil. This is necessary for the ESR oscillator to be not significantly affected by the NMR microcoil.

The second concern is related to the ESR oscillator layout. Most of this layout has to be below the NMR microcoil, because of the big frequency and size difference between ESR and NMR systems. As the ESR oscillator operates at very high frequency, the coils and inductive lines are very short compared to the much lower frequency of the NMR counter part. The NMR coil has 21 turns and is realized with the three top thick layers according to the criteria explained in the Section 3.3. As a result, the ESR oscillator layout is designed without using the three top thick metals apart from the L_B (see Fig. 3.1 and Fig. 3.8(c)).

Since the L_B inductor (ESR microcoil) is in the middle of the NMR microcoil, there is freedom to choose which layer to use in the design. The ESR excitation/detection coil L_B is designed using the second thick metal from the top. The top layer is thicker than the second top layer, but its series resistance is not lower because it is made of aluminum rather than copper which is less resistive by about a factor of 1.6. Moreover, connection from the second top layer to the top layer needs to be done through a resistive thin layer and very resistive vias. Hence, using the second top layer is preferable. The third top layer has the same sheet resistance as the second top layer, so the third top layer could also be utilized for L_B design. The distance from the sample is important at the level of some micrometers as the diameter of the ESR microcoil is 45 μm. So, the second top layer becomes a better choice compared the third top layer to minimize the distance to the top surface of the chip. Moreover, the vias from the third top layer to the second top layer have a sufficiently low resistance to have negligible impact on the oscillator performance.

The EM simulations of the oscillator are performed with a complete metal coverage in place of the NMR microcoil to allow for a converging and faster simulation. In Fig. 3.9, the picture of the layout simulation file is shown. The orange layer indicates the metal coverage that is used to simulate the effect of the other layers. As the other layers have slits in the real layout, the metal coverage simulates the worst condition.

3.6 Array microsystem

The ESR microcoil of the single oscillator interrogates a sample volume of about 50 μm x 50 μm x 25 μm. Although there are interesting samples to work at this volume, there are also concentration limited samples where larger volumes are preferred. For this reason, the study of solutions to increase the excited volume are of great interest. Arrays of ESR and NMR systems have been shown before as discussed in section 1.3. In this work, we demonstrate, for the first time, an array of four frequency locked oscillators for ESR excitation in a DNP microsystem. Having four oscillators coupled together increases the effective sample volume to 100 μm x 100 μm x 50 μm, i.e. by a factor of 8 with respect to the single oscillator.

Fig. 3.10 shows the complete DNP array microsystem together with ESR and NMR microcoil photograph. The array system consists of four 200 GHz oscillators that are coupled together as shown in Fig. 3.11. The smallest capacitors available in the technology (34 fF) are used to couple oscillators and, at the same time, to load them as little as possible. Simulations show
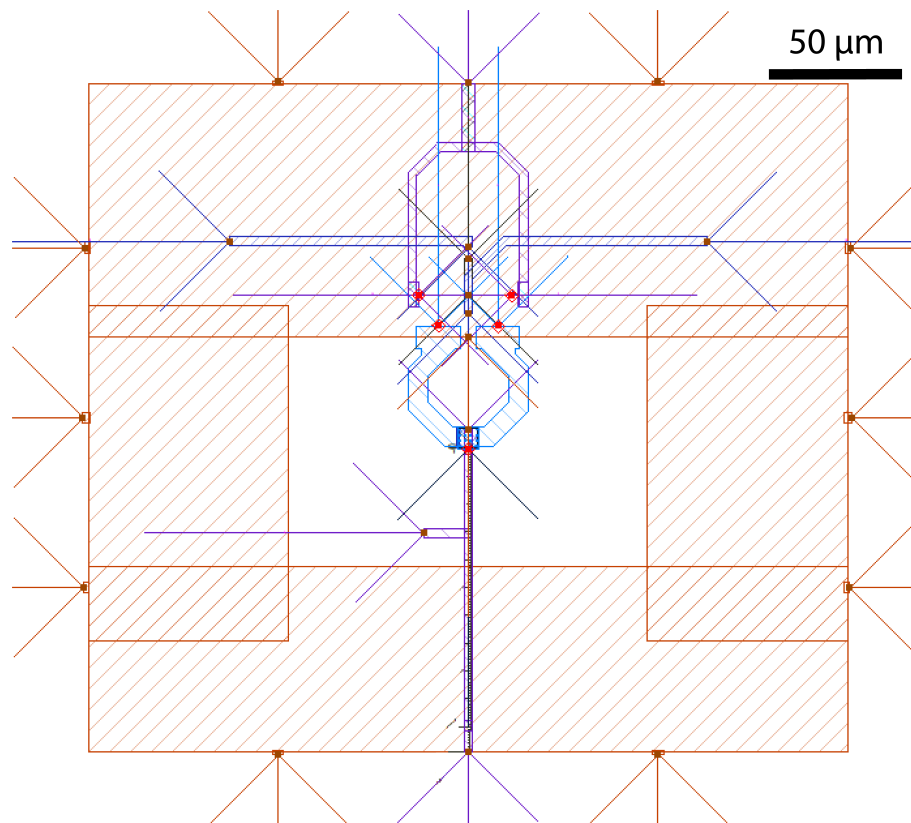
Figure 3.9: **ESR oscillator layout used for EM simulations.** The orange area shows the metal layer drawn for EM simulation to emulate the effect of the NMR coil on the oscillator.The NMR coil is deleted and replaced by metal coverage to allow for a converging and faster simulation. Arrows are the ports of the simulation.
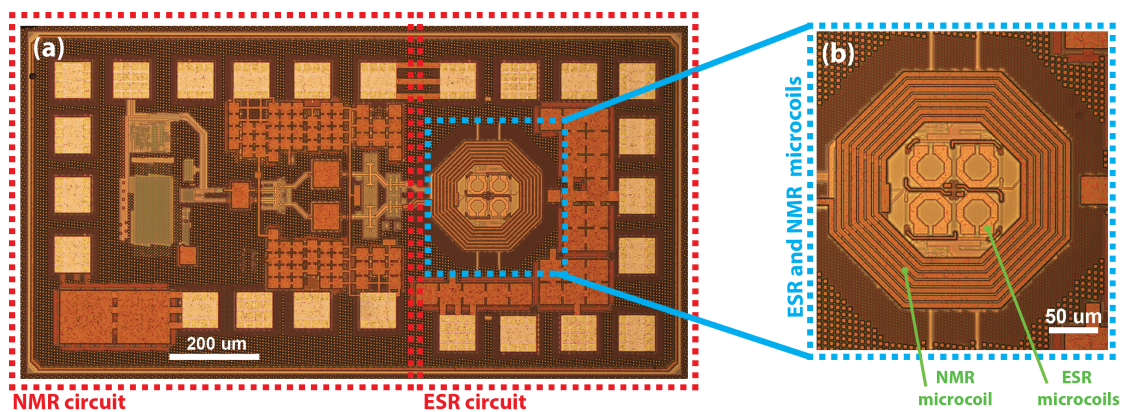
Figure 3.10: **The single chip integrated DNP array microsystem with four frequency locked microwave oscillators. (a)** Photograph of the single chip DNP array microsystem with four frequency locked microwave oscillators operating at 190 GHz. **(b)** Photograph of the NMR and ESR microcoils. Each ESR microcoil has a single turn and an external diameter of 45 μm. The NMR microcoil has 21 turns (7 turns in each of the three layers) and an external diameter of 250 μm.
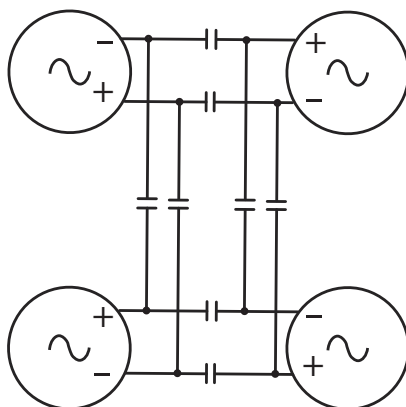
Figure 3.11: **Frequency locked oscillators of the single chip DNP array microsystem.** Each coupling capacitor has a capacitance of about 34 fF.

that when the oscillators are working at different frequencies (a difference is intentionally introduced in each oscillator for this simulation), after coupling them with this method, they all oscillate at the same frequency which is approximately the average frequency. There might be additional parasitic capacitive and inductive coupling of the oscillators which is not investigated in details.

The NMR microcoil for the array microsystem is slightly larger compared to the single microsystem. It is also realized with the three thick top metal layers available in the technology. It has an external diameter of 250 μm (50 μm larger compared to single oscillator microsystem NMR microcoil), a wire width of 5 μm, a wire thickness of around 3 μm, a spacing between the wires of 2.8 μm, and a total number of turns of 21 with 7 turns in each layer. The computed values for the inductance and the series resistance of the resulting NMR microcoil at the operating frequency of 300 MHz are 119 nH and 35 Ω. The NMR receiver electronics of the array microsystem is the same as the 200 GHz DNP microsystem. The NMR spin sensitivity of the array microsystem is calculated as 1.5×10^{13} spins/Hz$^{1/2}$ (see chapter 3.4 for the details of the spin sensitivity calculation).

3.7 Measurements

3.7.1 Preparation of the samples for DNP experiments

In order to characterize the performance of the realized DNP microsystems, we have used polystyrene (PS) and styrene-ethylene-butylene-styrene (SEBS) solid polymers doped with 2% α,γ-bisdiphenylene-β-phenylallyl (BDPA/benzene, 152560, Sigma-Aldrich). The BDPA ESR linewidth in these polymers is in the order of 10 G, hence it is well suited for observing well separated solid effect (SE) lines in the DNP enhancement profile at the ^{1}H Larmor frequency of 300 MHz corresponding to a field offset for the solid effect of about $\mp$110 G. BDPA:PS has

been investigated in several previous DNP experiments [113, 162–166] whereas BDPA:SEBS has not been investigated yet. At room temperature, the ^{1}H NMR linewidth of PS is of about 50 kHz whereas the one of SEBS is of about 1 kHz, presumably due to motional narrowing as observed also in other elastomers above their glass temperature [30, 48, 50].

The samples of 2% BDPA:PS and 2% BDPA:SEBS are prepared by dissolving PS (331651, MW 35000, Sigma-Aldrich) and BDPA in chloroform and SEBS (Kraton Corporation) and BDPA in toluene, respectively. The mixture is then drop casted on a glass plate and dried overnight under fumehood with a glass cover to reduce the speed of evaporation. If the evaporation is too fast, the top surface of the sample becomes very irregular. The amount of chloroform and toluene can be adjusted to tune the thickness of the resulting dried sample. Once the sample is completely dried, it is cut by a ceramic blade to obtain the desired dimensions. SEBS samples are difficult to cut due to their stretchability. In order to overcome this problem, SEBS samples are cut using an optical laser (Optec LightShot LSV3). Measurements show that the laser does not deteriorate the samples. Once cutted, the samples are picked up by toothpicks sharpened by a cutter. The samples adhere to the toothpick by Van der Waals forces and do not require any additional glue. Once in contact with chip surface, the samples adhere to it also by Van der Waals forces, or eventually glued adding diluted paper glue (Pritt, Henkel AG & Company). In Fig. 3.12(c), a 2% BDPA:PS sample placement example on top of the sensitive area of the microchip (i.e., on top of the concentric ESR and NMR microcoils) is shown.

3.7.2   Measurement setup

The single chip DNP microsystems are glued on PCBs with conductive epoxy (Epo-Tek, H20E-FC) and connections from the chip to PCB are made by bonding wires. Fig. 3.12(a) shows the PCB and 3.12(d) shows the bonding wires. The PCB shape and dimensions are chosen according to the available space in the magnet (Superconducting magnet with variable temperature insert, Cryogenic Ltd.). There are two coaxial cables and twelve twisted pair wires that can reach the PCB, thus there are two AC connectors available in the PCB. One of them is used for the NMR excitation signal and is connected to the NMR excitation coil through tuning and matching capacitors as shown in Fig. 3.12(a), (d) and Fig. 3.13(b). The NMR excitation coil is resonated by series tuning and parallel matching using mechanically tunable capacitors (EW Electronics, SGC3S100NM and SGC3S300NM). The excitation coil has two turns, a diameter of 6.5 mm and a wire diameter of 400 μm which results in 50 nH inductance and 1 Ω series resistance. The other AC connector is used for the local oscillator signal V_{LO} that is used in the down conversion of the NMR signal on-chip (see Fig. 3.3 and Fig. 3.5). All the other connections, including the NMR output and the ESR output are made using the twisted wires.

As seen in Fig. 3.12(a), there is a packaged component on the PCB (the black device in the center of the PCB) which is an amplifier. This amplifier is used for the amplification of the ESR signal to avoid deterioration of the SNR. Fig. 3.13(a) shows the complete amplifier schematic design. OPAMP THS4304D is used in the design because it is known to be working down to 1.4
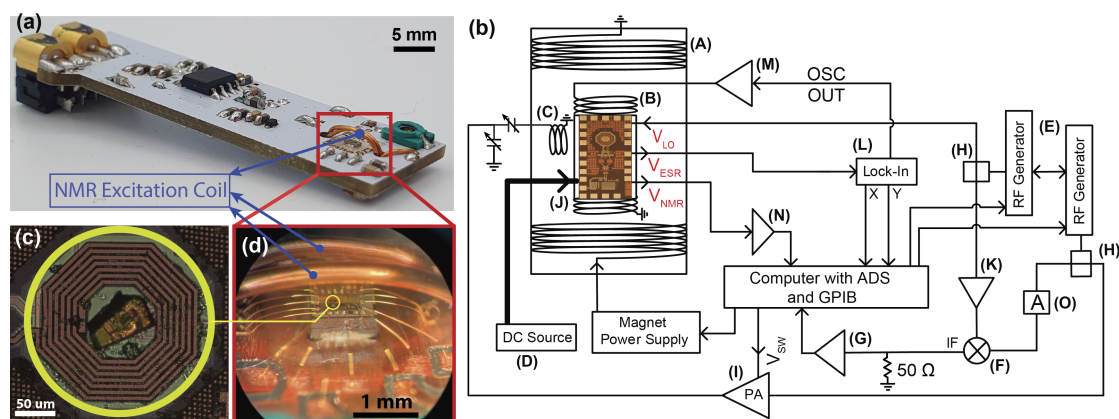
Figure 3.12: **Set-up for the characterization of the single chip integrated DNP microsystem operating at 200 GHz(ESR)/300 MHz(NMR). (a)** Printed Circuit Board (PCB) used for characterizing single chip DNP microsystem. The red rectangle indicates the chip and the NMR excitation coil. **(b)** Block diagram of the complete setup for the characterization of the single chip DNP microsystem: (A) Superconducting magnet with variable temperature insert (1.4-300 K, 0-9.4 T, Cryogenic Ltd); (B) Home-made resistive modulation coil (2.8 mT/A); (C) Home-made NMR excitation coil with tune and match variable capacitors; (D) DC power supplies (Keithley 2400); (E) RF generators (Stanford Research Systems SG384) ; (F) Frequency mixer (Mini-Circuits ZAD-1); (G) Amplifier (Stanford Research Systems SR560); (H) Power splitters (Mini-Circuits ZSC-2-1+); (I) RF Power amplifier (RFPA). The V_{SW} is the control signal that is connected to the power amplifier switch for generating pulsed excitations; (J) Photograph of the single chip DNP-NMR microsystem; (K) Amplifier (Mini-circuits ZX60-V83-S+); (L) Lock-in amplifier (EG&G 7265); (M) Power amplifier (Rohrer PA508); (N) Low noise differential amplifier (NF Corporation 5305, DC-10 MHz); (O) 26 dB attenuator. **(c)** Photograph of a 2%BDPA:PS sample placed on top of the ESR and NMR microcoils. **(d)** Photograph of the chip which shows the bonding wires and a part of the NMR excitation coil.

Figure 3.13: **Schematic of the components on the PCB. (a)** Schematic of the PCB ESR amplifier. The OPAMP is a THS4304D. R_1 =10 kΩ, R_2 =100 Ω, C_1 =100 pF, C_2 =10 μF, R_i =1 kΩ, C_i =1 μF and C_O =100 nF. **(b)** NMR excitation circuit. L_{excit} is the NMR excitation coil. The photograph of the excitation coil is in Fig. 3.12(a) and (d). C_T is tuning capacitor (SGC3S100NM) and C_M matching capacitor (two SGC3S300NM with a 10 pF capacitor in parallel).

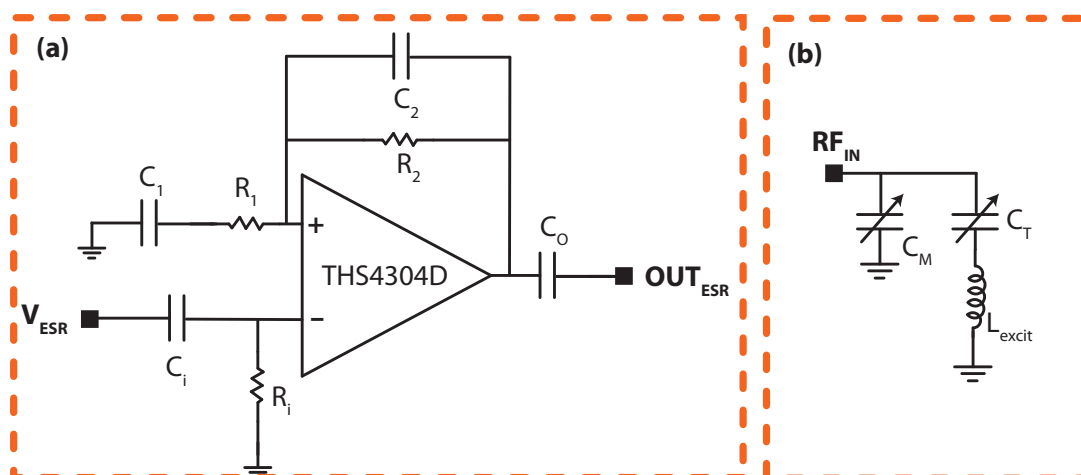K [73]. A simple resistive feedback with filters is utilized to set a gain of 100 V/V, a low pass filter of around 150 kHz, and a high pass filter of around 1 kHz. The bandwidth determines the modulation frequency range of the continuous wave ESR detection.

The NMR excitation coil is used to excite the subnanoliter sample placed on top of the integrated NMR detection microcoil. However, it excites efficiently also a volume of about 50 μL in the FR4 epoxy PCB, a material with a high density of ^{1}H nuclei. Despite the presence of a Cu layer having a thickness of 37 μm between the excited volume in the PCB and the integrated detection coil, the NMR signal induced in the detection coil by the ^{1}H nuclei in PCB substrate can be larger than the non-enhanced NMR signal induced in the detection coil by ^{1}H nuclei contained in a sample having a volume smaller than the sensitive volume of the detection coil. In order to compute the DNP enhancement, we quantified the background NMR signal by performing measurements without sample in the detection coil. For some of the samples investigated in this work (2% BDPA:PS), the background NMR signal is much larger than the non-enhanced NMR signal from the sample. This large ratio, makes an accurate experimental evaluation of the non-enhanced NMR signal difficult because the background NMR experiment and the experiment in presence of the sample cannot, in practice, be performed in the exact same conditions and are affected by noise. In our experimental conditions we estimated that the background signal cannot be determined with an error of less than 10%. In experiments where the non-enhanced NMR signal is below 10% of the background signal, we have assumed that the non-enhanced NMR signal is 10% of the background signal. To cross check this assumption, we have calculated the NMR signals that are expected to be measured. The expected signal is calculated based on the Bloch equations as explained in Ref. [30]. Even at

the optimum condition, the calculated NMR signal is smaller than the 10% of the background signal, which is the NMR signal amplitude used in the enhancement calculations. Therefore, this criteria leads to an underestimation of the DNP enhancement.

A possible solution to the background signal is the use of ceramic PCBs. These type of PCBs are produced generally from alumina based materials and does not contain ^{1}H nuclei. Another solution is the integration of the excitation coil and the transmitter. We have shown this approach in the 10 GHz DNP microsystem (see section 2.1) [46].

The measurement setup is shown in Fig. 3.12(b). Continuous wave ESR detection is performed with a modulation coil and a lock-in amplifier. The NMR output V_{NMR} is taken directly out of the chip and not further amplified on the PCB. Outside of the magnet, it is further amplified (amplifier (N) in Fig. 3.12(b)). This amplifier can be AC coupled at the input, but the deadtime is reduced if V_{NMR} is DC coupled. Since the V_{NMR} has a DC component of about 1 V, a differential amplification with a DC voltage source set to 1 V is required. Two frequency locked RF generators are used for NMR excitation and down conversion. Even though they are frequency locked at a fixed frequency difference of about 125 kHz, phase lock is not guaranteed by this method. As NMR signal coherence is necessary for signal averaging, a reference signal is generated by mixing these two RF signals (excitation and V_{LO}, with mixer (F) in Fig. 3.12(b)) and phase correction is applied in the digital signal processing performed by a home-made Labview^{TM} program.

3.7.3   Single chip DNP microsystem

At low temperature, due to saturation, the ESR spectrum of 2% BDPA:PS is hardly measurable in absence of oxygen. For this reason, in order to determine the oscillator frequency we used a grain of BDPA having a volume of a few μm^3. The operating frequency of the integrated oscillator is determined assuming an effective gyromagnetic ratio of 28.02 GHz/T [167]. The ESR spectra of the same BDPA grain at 300 K is shown in Fig. 3.14. The oscillator frequency shifts by the change of base current I_B and supply voltage VDD_{ESR} causing the ESR signal shift observed in the figure. Up to base current of 8 μA, the ESR signal is not saturated and it has the shape of the derivative of absorption (derivative is obtained because of the field modulation), while from 20 μA base current up, the ESR signal is reduced and its shape is changed. The change in amplitude and broadening is caused most probably by saturation, whereas the change in shape is not yet fully understood. From the measurement of the BDPA linewidth we determined the approximate value of the microwave magnetic field B_{1e} produced by the oscillator coil. The measured values at the inner side of the ESR microcoil wire are between 5 G and 11 G at 300 K depending on the I_B and the VDD_{ESR}, which is in agreement with the calculation of 2.75 G in the center of the coil (see Section 3.3).

The frequency tunability of the oscillator is measured with a BDPA sample. The graph in Fig. 3.15 is obtained when the oscillator is supplied with I_B = 45 μA, VDD_{ESR} = 1.05 V and IDD_{ESR} = 17 mA. The frequency is tunable up to 3 GHz by changing V$_T$ from 0 to 2 V. The
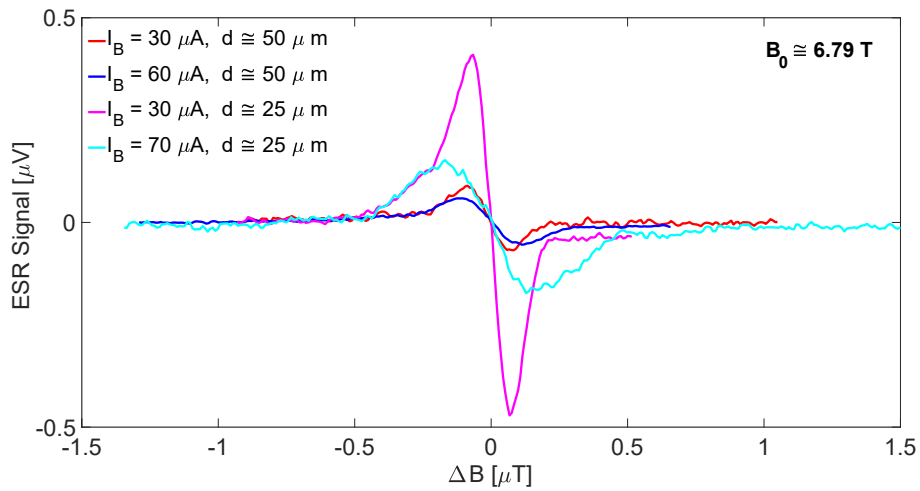
Figure 3.14: **ESR spectra of a grain of BDPA measured with the single chip DNP microsystem at 300 K.** The volume of the BDPA grain is approximately $(10 \ \mu m)^3$. The oscillator supply current I_B is changed from 30 μA to 70 μA, resulting in IDD_{ESR} changing between 14 and 21 mA. VDD_{ESR} is biased around 1.24 V. d is the distance between the sample and the ESR microcoil. The ESR measurements are performed in the following conditions: Modulation frequency $f_m \cong 16.829$ kHz, modulation magnetic field $B_m \cong 0.15$ mT, microwave frequency $f_{mw} \cong 190$ GHz, tuning voltage $V_T = 0$ V. The ESR spectra are shifted to center at the same point. The static magnetic field is around 6.79 T.
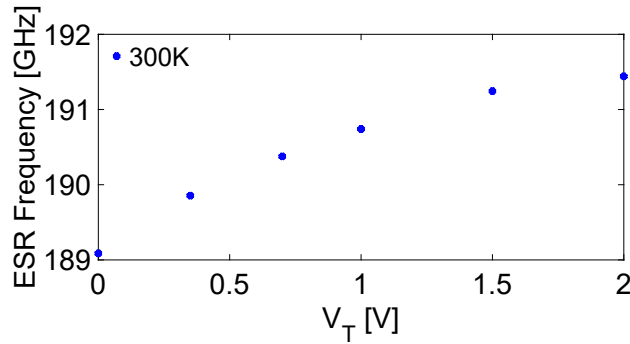
Figure 3.15: **Oscillator frequency vs. tuning voltage V_T curve measured with the single chip DNP microsystem at 300 K.** The oscillator is supplied with $I_B = 45\ \mu$A, $VDD_{ESR} = 1.05$ V and $IDD_{ESR} = 17$ mA. The oscillator frequency is calculated from the ESR spectrum of a BDPA sample, assuming a gyromagnetic ratio of 28.02 GHz/T.

oscillation frequency also depends on I_B and VDD_{ESR}. Fig. 3.14 shows that by changing I_B from 30 to 70 μA, ESR field is reduced by 90 mT which corresponds to 2.5 GHz frequency shift. Additional measurements show that the frequency is tunable up to 8 GHz by changing I_B, VDD_{ESR} and V_T altogether.

Fig. 3.16 shows the ESR spectra of BDPA at 10 K, 100 K and 200 K, demonstrating the possibility to work in a broad range of temperatures. The operation frequency of the oscillator shifts to higher frequencies as the temperature decreases.

This DNP system is suitable for different types of microwave driven DNP experiments. Solid effect DNP is selected as an example. Fig. 3.17 shows ^{1}H NMR spectra (left column) and DNP enhancement (right column) curve measured with a sample of 2% BDPA in PS having a volume of 100 x 200 x 100 μm^3 and 100 x 50 x 25 μm^3 at 15 K and 100 K. Both DNP curves are measured by sweeping the frequency of the oscillator by V_T. At each V_T value, the ^{1}H NMR spectra are measured with 80 and 200 averaging at 15 K and 100 K, respectively. Additional to the solid effect, Overhauser effect is observed at 15 K (see Fig. 3.17 (c)), as it has been previously reported in the literature [164]. When the microwave frequency is at $\omega_{OS} - \omega_{OI}$ ($\omega_{OS} = \gamma_e B_0$ is the ESR frequency and $\omega_{OI} = \gamma_{^1H} B_0$ is the NMR frequency), the NMR signal is enhanced by approximately +50 and +10 times (blue curves) at 15 K and 100 K, respectively. When microwave frequency is at $\omega_{OS} + \omega_{OI}$, the NMR signal is enhanced by approximately -50 and -10 times (red curves) at 15 K and 100 K, respectively. These results are compatible with the ones reported in the literature. Enhancements as large as 12 at 9.4 T and 100 K [164] and 10 at 5 T and 300 K [163] has been shown for the same sample. For a BDPA doped highly deuterated PS sample, enhancements of 8 at 300 K and 15 at 100 K has been shown at 18.8 T [168].
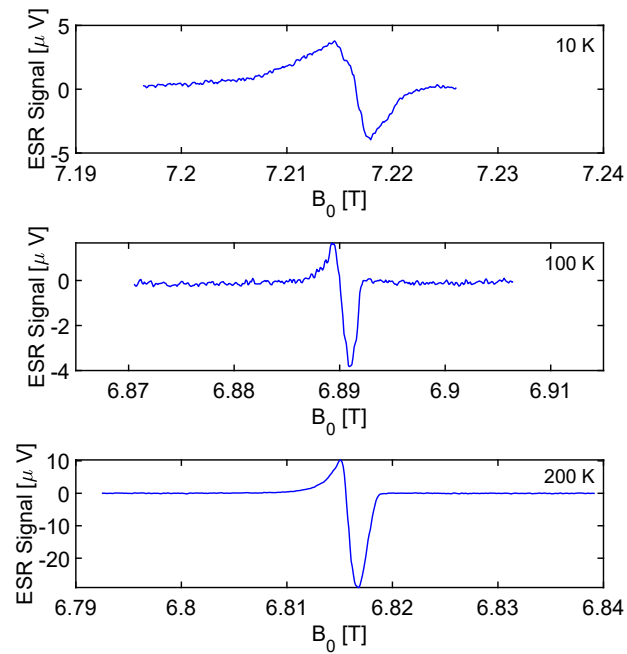
Figure 3.16: **ESR spectra of a grain of BDPA measured with the single chip DNP microsystem at 10, 100 and 200 K.** The oscillator supply current I_B is changed from 30 to 50 μA. VDD_{ESR} is adjusted between 0.7 and 1.3 V as the bias current increased, resulting in IDD_{ESR} to change between 20 and 22 mA. The ESR measurements are performed in the following conditions: Modulation frequency $f_m \cong 16.829$ kHz, modulation magnetic field $B_m \cong 0.15$ mT.
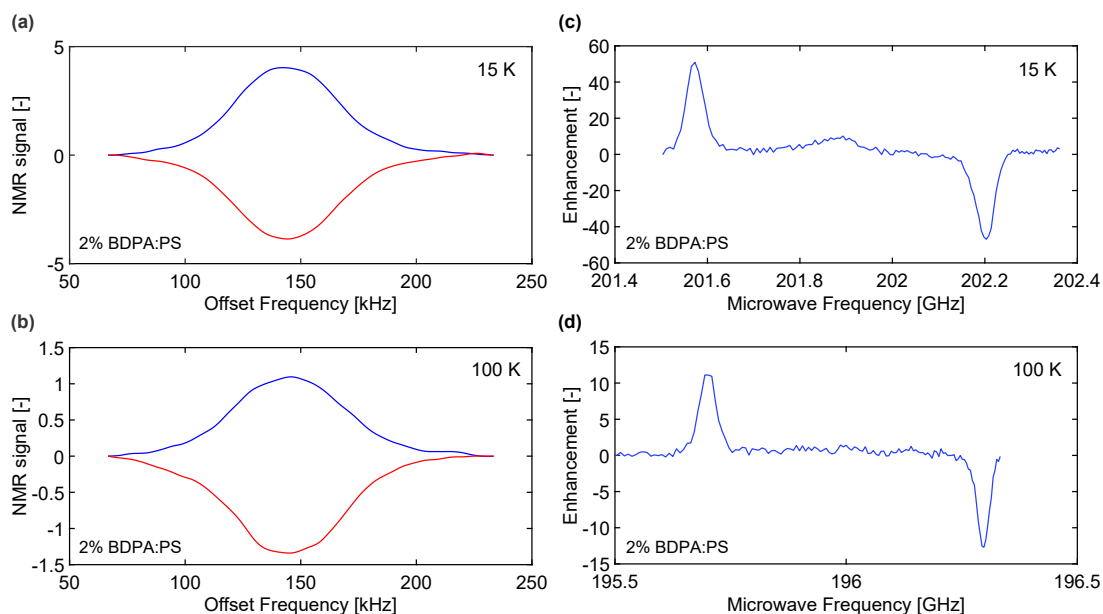
Figure 3.17: [1]**H NMR spectra and DNP enhancement curves measured with single chip integrated DNP microsystem.** ^{1}H NMR spectra **(a)** and DNP enhancement **(c)** curve measured with a sample of 2% BDPA in PS having a volume of 100 x 200 x 100 μm^3 at 15 K. The oscillator is supplied with $I_B = 30$ μA, $VDD_{ESR} = 1.1$ V and $IDD_{ESR} = 19$ mA. Each NMR measurement is performed in the following conditions: $f_{rf} \cong 307$ MHz, pulse length $\tau_{rf} = 3$ μs, pulse repetition time $T_r = 4$ s, time-domain match filter time constant $T_m = 30$ μs, acquisition time $T_{daq} = 15$ ms, number of averaging $N_{avg} = 80$. ^{1}H NMR spectra **(b)** and DNP enhancement **(d)** curve measured with a sample of 2% BDPA in PS having a volume of 100 x 50 x 25 μm^3 at 100 K. Oscillator is supplied with $I_B = 45$ μA, $VDD_{ESR} = 1.05$ V and $IDD_{ESR} = 23$ mA. Each NMR measurement is performed in the following conditions: $f_{rf} \cong 297$ MHz, $\tau_{rf} = 8$ μs, $T_r = 1$ s, $T_m = 30$ μs, $T_{daq} = 15$ ms, $N_{avg} = 200$. In **(a)** and **(b)** the blue curve is the DNP enhanced NMR spectra when microwaves are applied on the left side of the ESR peak ($\omega_{OS} - \omega_{OI}$) and the red curve is the DNP enhanced NMR spectra when microwaves are applied on the right side of the ESR peak ($\omega_{OS} + \omega_{OI}$).
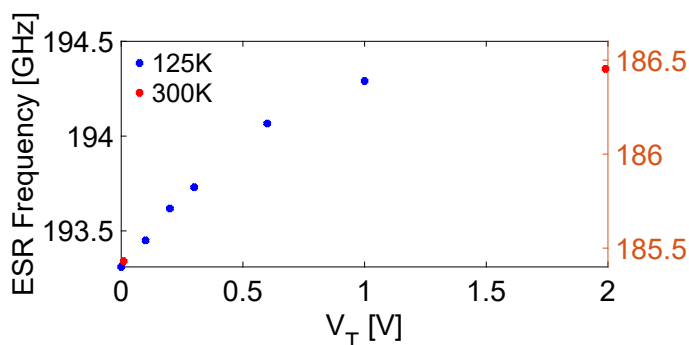
Figure 3.18: **Oscillator frequency vs. tuning voltage V_T curve measured with the single chip DNP array microsystem at 300 K and 125 K.** The oscillators are supplied with $I_B = 160$ μA, $VDD_{ESR} = 1.45$ V and $IDD_{ESR} = 77$ mA at 125 K and $I_B = 120$ μA, $VDD_{ESR} = 1.4$ V and $IDD_{ESR} = 50$ mA at 300 K. The oscillator frequency is calculated from the ESR spectrum of a BDPA sample, assuming a gyromagnetic ratio of 28.02 GHz/T.

3.7.4 Single chip DNP array microsystem

The main difference compared to the single oscillator microsystem is that the operating frequency is approximately 5 GHz lower in the oscillator array microsystem. The frequency tunability of the DNP array microsystem is measured similarly to the DNP microsystem and shown in Fig. 3.18 at 300 K and 125 K. The frequency tuning is not effective above 1 V, which is also an important difference compared to the single oscillator microsystem. The frequency is tunable by approximately 1 GHz, by changing the tuning voltage V_T from 0 to 2 V. On the other hand, the frequency tunability by I_B and VDD_{ESR} is still as effective as for the DNP microsystem with the single oscillator.

Fig. 3.19 shows the ESR spectra of a BDPA grain having a volume of a few μm^3. This BDPA grain is placed on top of the polymer sample, so there is a distance of about 30 μm from the top of the ESR microcoil to the sample. In Fig. 3.19(c), an ESR spectrum with a V_T scan is shown.

Fig. 3.20 shows ^{1}H NMR spectra (left column) and DNP enhancement (right column) curves measured with a sample of 2% BDPA in PS having a volume of 100 x 175 x 50 μm^3 at 200 K, a sample of 2% BDPA in SEBS having a volume of 90 x 90 x 30 μm^3 and 200 x 200 x 100 μm^3 at 300 K. All three DNP curves are measured by sweeping the frequency of the oscillator. At each V_T value, the ^{1}H NMR spectra are measured with 720, 480 and 3600 averaging at 200 K, 300 K and 100 K, respectively. While it was not possible to measure non-enhanced NMR for the 2% BDPA:PS sample, non-enhanced NMR signals for 2% BDPA:SEBS samples are shown in green in Fig. 3.20(b) and (c). To the best of my knowledge, DNP experiments on BDPA:SEBS samples are performed for the first time in this work. An Overhauser DNP is observed at room temperature in Fig. 3.20(e) and Fig. 3.20(f). Overhauser and solid effect enhancements are below two at 300 K, whereas the solid effect enhancements increase up to 20 at 200 K.
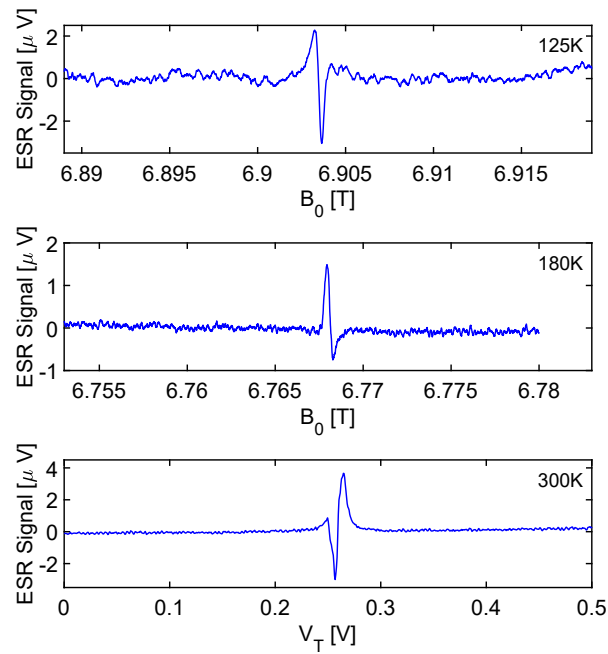
Figure 3.19: **ESR spectra of a grain of BDPA measured with the single chip DNP array microsystem at 125, 180 and 300 K.** The BDPA grain is placed on top of a polymer sample, so there is a distance of about 30 μm from the sample to the detection coil. The oscillator supply current I_B is changed from 140 to 160 μA. VDD_{ESR} is adjusted between 1.2 and 1.35 V as the bias current increased, resulting in IDD_{ESR} changing from 63 to 79 mA. The ESR measurements are performed in the following conditions: Modulation frequency $f_m \cong 16$ kHz, modulation magnetic field $B_m \cong 0.15$ mT.
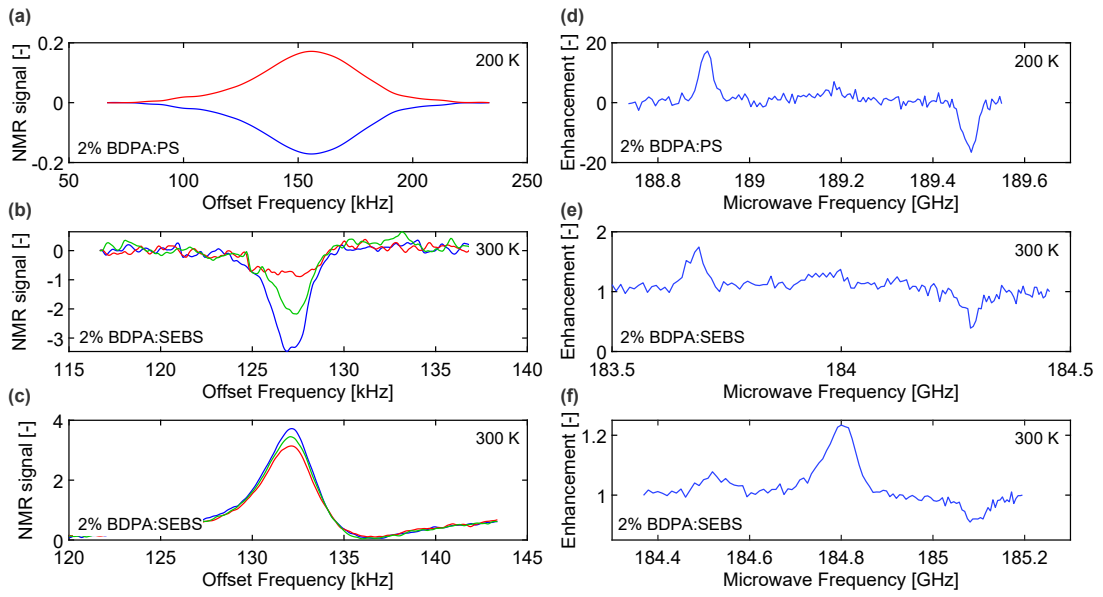
Figure 3.20: ^{1}**H NMR spectra and DNP enhancement curves measured with the single chip integrated DNP array microsystem**. ^{1}H NMR spectra **(a)** and DNP enhancement **(d)** curve measured with a sample of 2% BDPA in PS having a volume of 100 x 175 x 50 μm^3 at 200 K. The oscillators are supplied with $I_B = 180\mu$A, $VDD_{ESR} = 1.5$ V and $IDD_{ESR} = 80$ mA. Each NMR measurement is performed in the following conditions: $f_{rf} \cong 287$ MHz, $\tau_{rf} = 8$ μs, $T_r = 500$ ms, $T_m = 30$ μs, $T_{daq} = 15$ ms, $N_{avg} = 720$. ^{1}H NMR spectra **(b)** and DNP enhancement **(e)** curve measured with a sample of 2% BDPA in SEBS having a volume of 90 x 90 x 30 μm^3 at 300 K. The oscillators are supplied with $I_B = 140$ μA, $VDD_{ESR} = 1.1$ V and $IDD_{ESR} = 60$ mA. Each NMR measurement is performed in the following conditions: $f_{rf} \cong 280$ MHz, $\tau_{rf} = 18$ μs, $T_r = 1$ s, $T_m = 1$ ms, $T_{daq} = 15$ ms, $N_{avg} = 480$. ^{1}H NMR spectra **(c)** and DNP enhancement **(f)** curve measured with a sample of 2% BDPA in SEBS having a volume of 200 x 200 x 100 μm^3 at 300 K. Oscillators are supplied with $I_B = 140$ μA, $VDD_{ESR} = 1.1$ V and $IDD_{ESR} = 60$ mA. Each NMR measurement is performed in the following conditions: $f_{rf} \cong 281$ MHz, $\tau_{rf} = 8$ μs, $T_r = 100$ ms, $T_m = 1$ ms, $T_{daq} = 15$ ms, $N_{avg} = 3600$. In **(a)**, **(b)** and **(c)** the blue curve is the DNP enhanced NMR spectra when microwaves are applied on the left side of the ESR peak ($\omega_{OS} - \omega_{OI}$), the red curve is the DNP enhanced NMR spectra when microwaves are applied on the right side of the ESR peak ($\omega_{OS} + \omega_{OI}$). In **(b)** and **(c)** the green curve is the NMR spectra when microwaves are far from the ESR peak.

Overhauser enhancements in BDPA:PS have been reported in the literature [164].

The DNP enhancement curve shown in Fig. 3.20(f) is measured with a sample size which is 16 times larger than the one in Fig. 3.20(e). The oscillator is biased at the same values, whereas the pulse length τ_{rf} and the repetition time T_r are longer for the curve in Fig. 3.20(e). While Overhauser enhancements are similar for both DNP curves (about 1.2), the solid effect enhancement is larger in Fig. 3.20(e) compared to Fig. 3.20(f) (about 1.7 and 1.05, respectively). This is most probably due to the larger build up time of the solid effect compared to the Overhauser effect ($T_r = 1$ s compared to $T_r = 100$ ms leads to a larger solid effect enhancement).

4 Low power HEMT oscillators for cryogenic single chip DNP microsystems

This chapter is a variation of the publications "A single chip electron spin resonance detector based on a single high electron mobility transistor, A.V. Matheoud, N. Sahin, G. Boero, *Journal of Magnetic Resonance 294*, 2018" [94], "A Low-Power Microwave HEMT *LC* Oscillator Operating Down to 1.4 K, A.V. Matheoud, N. Sahin Solmaz, G. Boero, *IEEE Transactions on Microwave Theory and Techniques 67(7)*, 2019" [169], and "A Low Power 35 GHz HEMT Oscillator for Electron Spin Resonance Spectroscopy, N. Sahin Solmaz, A.V. Matheoud, G. Boero, *IEEE Radio Frequency Integrated Circuits Symposium (RFIC)*, 2021." [170]. I have contributed to measurements, data analysis and paper writing of the first two work [94], [169]. I have contributed to the chip design, measurements, data analysis and paper writing of the last work [170].

4.1 Introduction

Electron spin resonance (ESR) is a widely used spectroscopic tool in physics, chemistry, material science, biology and medicine, to investigate the structure, dynamics, and spatial distribution of paramagnetic species in a wide range of frequencies (typically from 100 MHz to 1 THz) and temperatures (typically from 10 mK to 1000 K) [171–173]. The use of ESR detectors in an even wider range of applications is often hindered by the low spin sensitivity of such sensors. Several methods have been proposed to improve the limit of detection of ESR spectrometers [24, 25, 27, 65, 68, 70, 71]. The integration on a chip of the sensitivity-relevant part of such detectors has been shown to be a promising approach, especially for samples in the nanoliter and sub-nanoliter range [63, 72–74, 93]. Integration of the sensitivity-relevant part of the ESR sensor reduces complexity and loss of the connections, improving the spin sensitivity and allowing for future implementation in array of detectors for parallel (simultaneous) spectroscopy of several samples in the same magnet. The matching of the size of the detection coil to the size of the sample provides the optimization of the sensor sensitivity. Generally speaking, operation at higher frequency and lower temperature allows also to improve the spin sensitivity.

High electron mobility transistors (HEMT) based on two dimensional electron gases (2DEG) in

III-V heterostructures have superior charge carrier mobility compared to silicon based CMOS technologies. The large mobility makes them particularly attractive for a variety of low noise and high power, radio frequency, microwave, and terahertz applications [174–177]. HEMTs are currently widely used also for cryogenic applications, and considered as promising candidates for the cold read-out electronics of future quantum computers [178–186]. At temperatures of about 1 K and above, the cooling power of ^{4}He based cooling systems can exceed 100 mW [187]. At temperatures below 1 K, the effective cooling power available with ^{3}He and ^{3}He^{4}He dilution refrigerators is typically below 1 mW [115]. Hence, for applications at temperatures in the order of 1 K and below, electronics has to be designed considering power dissipation as a major critical constraint.

The goal of this work is to design ultra low power microwave oscillators for ESR excitation and detection, and investigate their characteristics at different temperatures. These oscillators are planned to be used for low power cryogenic single chip DNP microsystems that will be able to operate down to 1 K and possibly below. Low power consumption is necessary to operate these microsystems at such low temperatures. As a first step towards this goal, in section 4.2, HEMT transistors are characterized at different temperatures and static magnetic fields. In the second step, in section 4.3, a low power 11 GHz oscillator is reported. The detailed characterization of this oscillator as an ESR sensor is reported in Ref. [94] and the analytical study on low power oscillators is reported in Ref. [169]. Lastly, in section 4.4, a low power 35 GHz oscillator is designed and characterized as an ESR sensor. A comparison table is given to show its performance compared to the oscillators reported in the literature.

4.2 HEMT transistor modeling

In this section we investigate the behavior of a standalone HEMT transistor. In particular, we perform its characterization in the temperature range from 1.4 to 300 K and in the magnetic field range from 0 to 8 T. Devices were manufactured using an HEMT technology having a minimum gate length of 70 nm (D007IH mHEMT, OMMIC, France). The transistor channel consist of a 2DEG in In$_{0.7}$Ga$_{0.3}$As. In [176] and [188], transistors and low noise microwave amplifiers fabricated with the same technology are characterized in the temperature range from 20 to 300 K. In this work we extend the temperature range and add a strong magnetic field as a means to extract useful information about the properties of the transistors.

4.2.1 Description of the measurement set-up

Fig. 4.1(a) shows the layout of the standalone HEMT transistor, which consists of four fingers having a width of 15 μm, a drain-source distance of 2.5 μm, and a gate length of 70 nm. The properties of this standalone HEMT transistor as a function of the temperature (1.4 to 300 K) and of the magnetic field (0 to 8 T) are investigated in Section 4.2.2. Fig. 4.1(b) shows the block diagram of the set-up used to characterize the standalone HEMT transistor. The standalone transistor is connected to a semiconductor parameter analyzer in Kelvin 4-wires
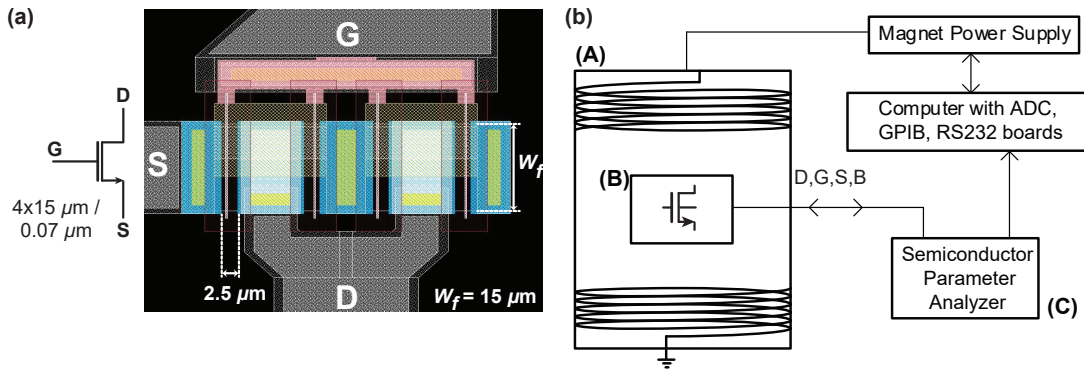
Figure 4.1: **Schematic and picture of the realized HEMT structure.** (a) Symbol and layout of the standalone HEMT transistor of four fingers. The finger width W_f is 15 μm, the source-drain distance is 2.5 μm, and the gate length is 70 nm. (b) Block diagram of the complete set-up for the characterization of the standalone transistor: (A) Superconducting magnet with variable temperature insert (1.4 to 300 K, 0 to 9.4 T, Cryogenic Ltd); (B) Standalone HEMT transistor; (C) Semiconductor parameter analyzer (HP 4156A).

configuration.

4.2.2 Measurements and transistor parameters extraction

In this section, we report the characterization of the standalone HEMT transistor shown in Fig. 4.1(a) in the temperature range from 1.4 to 300 K. A static magnetic field from 0 to 8 T is used to measure its geometrical magnetoresistance (i.e., only due to the Lorentz force) and its Shubnikov-de-Haas (SdH) resistance oscillations. The former is a standard approach which allows to extract the effective drain-source mobility as an independent variable, whereas the latter leads to the extraction of the charge carriers density as an independent parameter from the mobility (i.e., a necessary condition to cross-check the obtained results with the mobility and the conductivity measurements). Indeed, as we will show below, the values of these parameters extracted from magnetoresistance measurements are in good agreement with those obtained from the DC characterization of the transistor at zero magnetic field.

Fig. 4.2 shows the DC characterization (I_{DS}-V_{DS} curves for different V_{GS} values) from 1.4 to 300 K of the HEMT transistor shown in Fig. 4.1(a). V_{DS} is swept from 0 to 1 V whereas V_{GS} spans from -0.4 to 0 V. For a given bias condition (V_{GS} and V_{DS}), the drain current I_{DS} is almost constant from 1.4 to 30 K, and increases from 30 to 300 K. The kink effect with hysteresis [189] is visible below 10 K.

According to the level 1 Shichman-Hodges model [190–192], we extract the threshold voltage V_{th}, the intrinsic β, and the channel length modulation factor λ from the DC characterization at temperatures from 1.4 to 300 K shown in Fig. 4.2. The extraction of these parameters aims at extending the applicability of the models provided by the foundry down to deep cryogenic
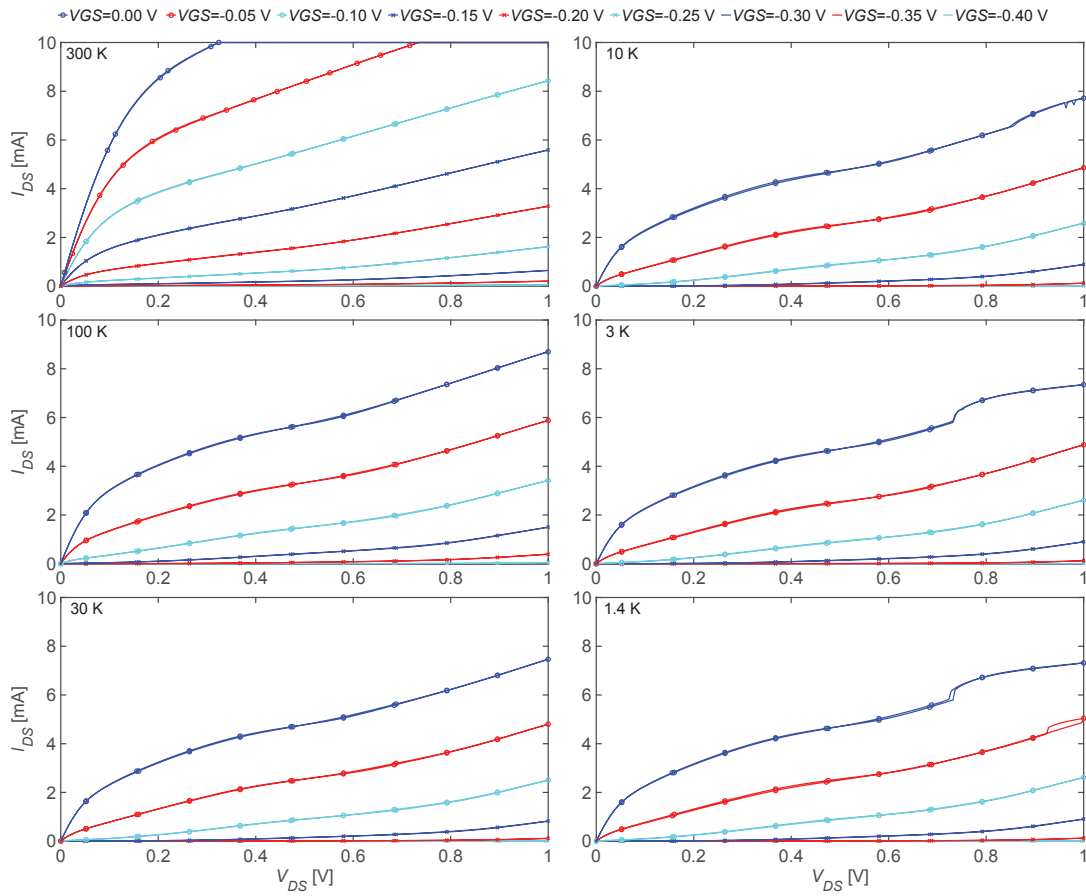
Figure 4.2: **Characterization of the standalone HEMT transistor.** The DC drain-source current I_{DS} is shown as a function of the drain-source voltage V_{DS} for different gate-source voltages V_{GS}, from 1.4 to 300 K. The transistor is composed of 4 fingers (each having a width of 15 μm for a total width of 60 μm), and it has a source-drain distance of 2.5 μm, and a gate length of 70 nm (see Fig. 4.1(a)).
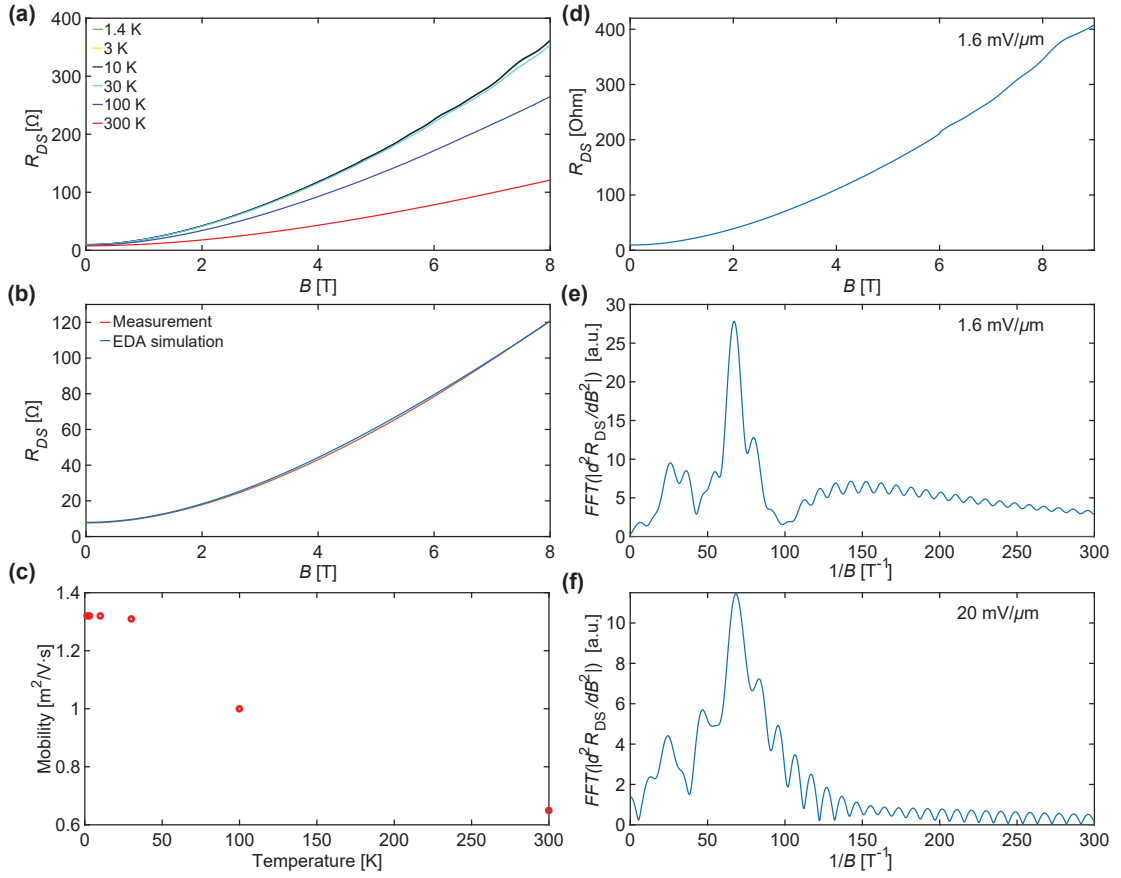
Figure 4.3: **Magnetoresistance, mobility, and Shubnikov-de-Haas oscillations of the standalone HEMT transistor.** (a) Source-drain resistance R_{DS} as a function of the applied static magnetic field (from 0 to 8 T, orthogonal to the 2DEG) from 1.4 to 300 K. The curves from 1.4 to 30 K overlap. The transistor is biased with $V_{GS} = 0.2$ V and $V_{DS} = 50$ mV. (b) Comparison between the measured and the EDA simulated R_{DS} as a function of the applied static magnetic field (see details of the EDA simulation in the text). (c) Extracted effective carrier mobility as a function of the temperature. The magnitude of carrier mobility has no significant variation from 1.4 to 30 K, and decreases by a factor of two from 30 to 300 K. (d) Source-drain resistance R_{DS} as a function of the magnetic field for $V_{GS} = 0.2$ V and $V_{DS} = 4$ mV (i.e., electric field of 16×10^{-4} V/μm). Small Shubnikov-de-Haas oscillations are visible above 5 T. (e) FFT of $d^2 R_{DS}/dB^2$ plotted as a function of $1/B$. The source-drain resistance R_{DS} is the one plotted in (d). The main periodicity of the Shubnikov-de-Haas oscillations is at 70 T^{-1}. (f) FFT of $d^2 R_{DS}/dB^2$ plotted as a function of $1/B$. The source-drain resistance R_{DS} is measured at $V_{DS} = 50$ mV (i.e., with an electric field of 2×10^{-2} V/μm). The periodicity is the same as in (e), but with a much smaller amplitude, presumably due to the larger electric field applied.

conditions. In order to extract V_{th}, we plot the I_{DS}-V_{GS} curves from the data shown in the I_{DS}-V_{DS} characterization, and we identify the tangent line with the maximum slope for $V_{DS} = 10$ mV. The latter intercepts the V_{GS} axis at the point which corresponds to the threshold voltage V_{th} [193]. The value of β is directly extracted from the source-drain resistance $R_{DS} = V_{DS}/I_{DS}$ when the transistor is polarized in the triode region ($V_{DS} << V_{GS} - V_{th}$), i.e., $\beta = 1/(R_{DS}(V_{GS} - V_{th}))$. The channel length modulation factor is extracted in deep saturation ($V_{DS} >> V_{GS} - V_{th}$) and can be written as $\lambda = 2\Delta I_{DS}/(\Delta V_{DS}\beta(V_{GS} - V_{th})^2)$. From the experimental data, we obtain $V_{th} = -0.22$ V at 300 K and $V_{th} = -0.07$ V at 1.4 K. A similar behavior has been already reported in the literature for both CMOS and HEMT transistors at low temperature [194–196]. The extracted value of β is 0.28 A/V^2 at 300 K and 0.47 A/V^2 at 1.4 K. λ is approximately 10 V^{-1} at 300 K and 2 V^{-1} at 1.4 K.

Fig. 4.3(a) shows the measured HEMT transistor source-drain resistance R_{DS} as a function of the static magnetic field B applied in the direction orthogonal to the 2DEG plane. If the magnetic field is applied parallel to the 2DEG plane, a much smaller change of R_{DS} is measured (about 2.5% from 0 to 8 T). This indicates that the observed resistance variation is due to the geometrical magnetoresistance (i.e., the Hall effect). The measurement of the geometrical magnetoresistance is widely used as a method for the extraction of the charge carrier mobility [197–199]. In order to model the device and extract the carrier mobility, we used the equivalent circuit described in [200]. Such model, which can be implemented in any electronic-design-automation (EDA) simulator, consists of a network of identical magnetic field dependent resistors and current-controlled-current-sources. The extracted mobility value is 0.65 m^2/Vs at 300 K and 1.2 m^2/Vs at 1.4 K. This result is coherent with the extracted β, which also increases by a factor of two at low temperature.

The drain-source resistance R_{DS} is approximately 8 Ω at zero field, regardless of the temperature (Fig. 4.3(a)). Since the conductivity is defined as $\sigma = en\mu$ (where e is the elementary charge, n is the density of carriers, and μ is the mobility) and the resistance is $R_{DS} = L_{SD}/W\sigma$ (where $L_{SD} = 2.5$ μm and $W = 60$ μm are the transistor source-drain distance and width, respectively), we estimate a density of carriers of about 5×10^{16} m^{-2}. In order to cross check such a result, we measured the periodicity of the SdH oscillations [197, 201]. In our case, the SdH oscillations are the oscillations of R_{DS} as a function of the applied magnetic field, which we measured at 1.4 K. As shown in Fig. 4.3(d,e,f), we observe SdH oscillations for magnetic field values above 5 T, at 1.4 K, and for V_{DS} values of 50 mV (i.e., at an electric field of 2×10^{-2} V/μm) and 4 mV (i.e., at an electric field of 16×10^{-4} V/μm). The periodicity is more evident at the lower electric field. Performing the Fast-Fourier-Transform (FFT) of $d^2 R_{DS}/dB^2$, plotted as a function of $1/B$, allows to extract the oscillation frequency. As shown in Figs. 4.3(e, f) there is a main frequency component at about 70 T^{-1}. According to [201], we compute the density of carriers as $n \cong \frac{2e/h}{\Delta(1/B)} \cong 3.5 \times 10^{16}$ m^{-2}, where h is the Planck constant and $\Delta(1/B)$ is the periodicity of the SdH oscillations. This value for the density of carriers is in good agreement with the one estimated above, obtained from measurements of the resistance (i.e., 5×10^{16} m^{-2}). The SdH oscillations reported in this work are significantly smaller than those reported in previous publications [201–205]. This might be due to the larger electric fields applied to

the HEMT transistor with respect to those usually reported in the literature. In [202–204], it is shown that the SdH oscillations are reduced when the applied electric field is increased. In our measurements, the minimum practically applicable electric field is approximately 10^{-3} V/μm. Indeed, in our experimental set-up, at lower V_{DS} and, hence, at lower electric fields, the magnetoresistance measurements are too noisy to allow for the extraction of the charge carrier density.

4.3   Single chip 11 GHz HEMT ESR detector

HEMTs based on two dimensional electron gases in III-V heterostructures have superior mobility compared to the transistors of silicon based CMOS technologies. The large mobility makes them attractive not only for low noise and high power microwave applications but also for low power applications down to deep cryogenic temperatures. In this section, we report a low power HEMT *LC* Colpitts oscillator operating at 11 GHz whose minimum power consumption is 90 μW at 300 K and 4 μW at 1.4 K.

In the design of integrated CMOS and HEMT microwave oscillators, the main effort is usually focused on the improvement of phase noise, output power, and tuning range [206–209]. Recently, motivated by their use in room temperature applications where power consumption is important (such as RF identification), several low power consumption CMOS and HEMT designs have been reported [210–219]. For example, an HEMT oscillator operating at 4.7 GHz has achieved power consumption of 2.7 mW [219] whereas CMOS oscillators have achieved a power consumptions of 280 μW at 40 GHz [210] and, very recently, of 130 μW at 57.4 GHz [213]. A very limited literature exists on microwave oscillators operating at liquid helium temperature (i.e., 4.2 K) and below [186, 220–222]. The lowest reported power consumption is of about 7 mW [186]. Hence, the HEMT oscillator reported in this work achieves a room temperature power consumption which is slightly better than the state-of-the-art, and a significantly lower power consumption at low temperature.

Reducing the power consumption in *LC* oscillators is of crucial importance, e.g., for their application as single chip ESR spectroscopy detectors [94, 223–227] and single chip DNP microsystems at low temperatures. Exploring the behavior of microwave *LC* oscillators in cryogenic conditions is also interesting for studies of the phase noise of thermal and non-thermal origin [228, 229]. Particularly interesting would be the operation in the condition $\hbar\omega > k_B T$, which should result in a dramatic reduction of the phase noise of thermal origin, well beyond the linear dependence on T of the power spectral density in the condition $\hbar\omega < k_B T$ [230, 231], where k_B is the Boltzmann constant, T is the temperature, $\hbar$ is the reduced Planck constant, and ω is the oscillation angular frequency. The study of the zero-point quantum noise [230, 232–235], which in this case should be possibly present in the form of oscillator phase noise, would be also experimentally accessible.
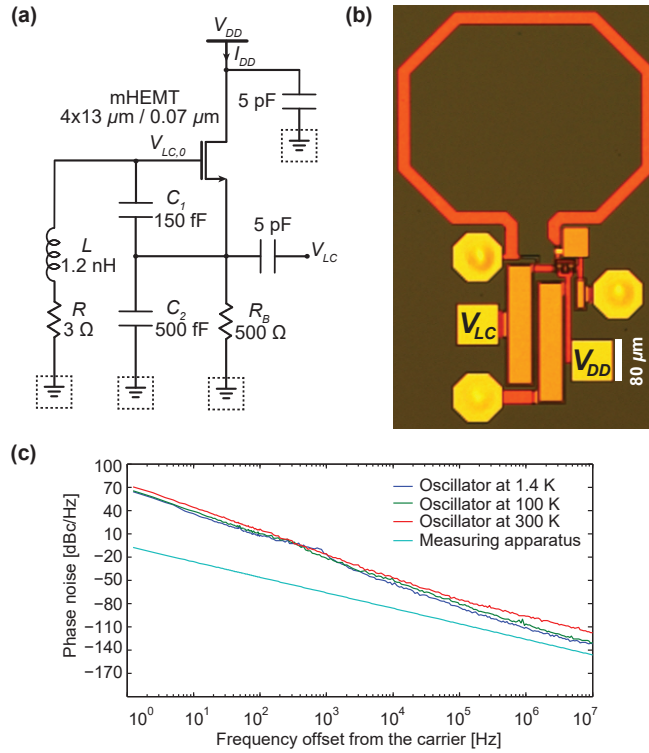
Figure 4.4: **Schematics, picture and phase noise of the 11 GHz ESR detector.** (a) Detailed schematic of the HEMT LC Colpitts oscillator. It consists of an inductor L with a series resistance R, forming a resonator with the capacitors C_1 and C_2, a single HEMT transistor, and a bias resistor R_B. The transistor has a gate length of 0.07 μm and a total gate width of 52 μm (four fingers, each 13 μm wide). The oscillator is power supplied from a dc source (current: I_{DD}, voltage: V_{DD}). (b) Picture of the single chip ESR detector. (c) Measured phase noise spectral density of the HEMT LC Colpitts oscillator at 1.4 K, 100 K, and 300 K, at the minimum bias voltage for stable oscillations. At all temperatures, the minimum noise is measured at the minimum bias.

4.3.1 Description of the oscillator

The single chip ESR detector described in this chapter is manufactured using a high electron mobility transistor (HEMT) technology (D007IH mHEMT, OMMIC, France). The transistor channel consists of a two dimensional electron gas (2DEG) in $In_{0.7}Ga_{0.3}As$. The gate length is 70 nm. The ESR detector based on an 11 GHz HEMT LC Colpitts oscillator operating in the temperature range from 300 K down to 1.4 K, at least.

Figure 4.4 shows a picture of the realized HEMT LC Colpitts oscillator and its detailed schematics. As shown in Fig. 4.4(a), the oscillator consists of a single HEMT transistor, a single turn planar coil inductor, a resistor, and two capacitors. The realized common-drain Colpitts topology achieves low output impedance without loading the LC resonator. The capacitors C_1 and C_2 not only provide the positive feedback to the amplifier, but also form the resonator

with the inductor. The inductor is connected to ground by means of metalized holes (vias) connecting the top-side to the bottom-side of the chip. These metalized holes are useful to avoid the use of bonding wires for ground connections, hence allowing the implementation of non-differential topologies with low parasitics. Since the source-drain on-resistance of the HEMT transistor and the dc resistance from gate to ground are very low, the 500 Ω resistor determines the dc operating point of the oscillator and acts as current source. The operating frequency of the oscillator depends on the bias voltage V_{DD} and on the temperature, with an overall range from 11.2 GHz to 11.7 GHz. The integrated Colpitts LC oscillator has a size of 0.8×0.5 mm^2 (Fig. 4.4(b)). A conductive epoxy (Epo-Tek, H20E-FC) is used to glue the chip to a standard FR4 printed circuit board. Au wires having a diameter of 20 μm are used for wedge-wedge bonding of the chip to the board.

In Table 4.1, the key-features of the realized system is reported. Coil inductance, resistance and quality factor are simulated values. The HEMT LC Colpitts oscillator shows a minimum (i.e., start-up) power consumption of 90 μW at 300 K (V_{DD} = 220 mV, I_{DD} = 400 μA) and 4 μW below 30 K (V_{DD} = 40 mV, I_{DD} = 110 μA). The aforementioned power consumption is, to the best of my knowledge, the lowest reported to date for an LC oscillator working in the same frequency range.

As reported above, the realized oscillator shows a lower power consumption at cryogenic temperatures than at 300 K. This is presumably due to the following reasons. The decrease of the threshold voltage from -0.22 to -0.07 V (see section 4.2.2) allows to reduce V_{DD} to obtain the same overdrive voltage $V_{GS} - V_{th}$. The decrease of the coil resistance results in a lower transconductance (g_m) necessary for oscillations (and, hence, in a lower minimum V_{DD}), whereas the increase of β results in a larger g_m (see Ref. [169] for detailed calculations).

It is worthy to note that the topology of the LC oscillator reported here (Fig. 4.4) is optimized for low parasitics and area occupation. Only a few components are required and the bias point of the oscillator is set through a single supply voltage V_{DD} (i.e., no extra pads are required). However, this architecture can be further optimized to achieve an even lower power consumption (see section 4.4). Indeed, the bias resistance R_B is large with respect to R_{DS} and R, so the majority of the power provided by the generator is dissipated across R_B, which has the only aim to produce a suitable V_{GS} bias. Additionally, since the threshold voltage of the transistor varies as a function of the temperature, it would be beneficial to optimize V_{GS} independently (e.g., by adjusting the gate voltage) whereas in the proposed architecture it results intrinsically defined by V_{DD}. As discussed in the section 4.4, a slightly more complex topology, where R_B is replaced by an inductor L_B and the gate-source voltage V_{GS} is freely adjustable, should allow to obtain a further significant reduction of the start-up power consumption.

In Fig. 4.4(c), we report the experimentally measured phase noise at 1.4 K, 100 K, and 300 K as well as the noise of the measuring apparatus, which is lower than the oscillator noise (6 dB in the worst case, i.e., at low temperature and large frequency offset from the carrier). The mea-

Table 4.1: Key-Features of the 11 GHz HEMT ESR detector

	300 K	1.4 K
Oscillation frequency [GHz]	11.2	11.3
Coil size [μ m^2]	400 x 480	400 x 480
Coil inductance [nH]	1.2	-
Coil resistane [Ω]	3	-
Coil quality factor	27	-
$V_{DD_{min}}$ [mV]	220	40
$I_{DD_{min}}$ [μA]	410	110
P_{min} [μW]	90	4
Frequency noise [Hz/Hz$^{1/2}$] @ 100 kHz	17	4
Figure of merit [dBc/Hz][*] @ 1 MHz frequency offset from the carrier	188	217
Minimum B_{1e} [μT]	0.4	-
Spin sensitivity [spins/Hz$^{1/2}$] @ 150 kHz	8×10^{10}	2×10^{9}[**]

[*] The oscillator figure-of-merit (FOM) is computed as $(20\log(f_{LC}/f_{OS}) - \mathscr{L}(f_{OS})) - 10\log(P_{min}))$, where $\mathscr{L}(f_{OS})$ is the phase noise (in dBc/Hz) at the frequency offset f_{OS} (in Hz), f_{LC} is the oscillator working frequency (in Hz), and P_{min} is the minimum power consumption (in mW) [229, 236].

[**] The spin sensitivity is given for 10 K. At 1.4 K, the spin sensitivity is reduced because of proximity with the antiferromagnetic transition of BDPA [94, 237].

sured phase noise floor (i.e., the phase noise at offset frequencies above the $1/f$ noise corner frequency, which is of about 1 MHz for our oscillator) corresponds, within a factor of two, to the thermal phase noise originating from the coil resistance given by $10\log(kTR(f_{LC}/f_{OS}V_{LC,0})^2)$, where $V_{LC,0}$ is the oscillation amplitude (in V), R is the coil resistance at the operating frequency (in Ω), and f_{OS} is the frequency offset from the carrier (in Hz) [238].

The results of the measurements on BDPA, Cu:Ni(mnt)$_2$, and Mn:MgO, performed with this oscillator are reported in Ref. [94]. These results underline the essential advantage of the HEMT sensor proposed in this work with respect to previously reported CMOS sensors. The previously reported CMOS sensors [72–74, 93, 239] had much larger B_1 values (in the range from 0.1 mT to 0.8 mT), causing line broadening and signal reduction (and, therefore, a very significant deterioration of the signal-to-noise ratio and, finally, of the spin sensitivity). The excessive B_1 was severely limiting the use of those sensors to samples having a product $T_1 T_2$ smaller than 10^{-15} s^2 (i.e., relaxation times shorter than 30 ns for $T_1 \cong T_2$). In this oscillator the minimum B_{1e} is estimated to be 0.4 μT at room temperature according to the simulations and measurements [94].

4.4 Single chip 35 GHz HEMT ESR detector

This section presents a low power microwave oscillator designed as sensor for electron spin resonance (ESR) spectroscopy. Low power consumption is necessary for low temperature operation. Additionally, lower power consumption allows for a lower microwave magnetic field in the sensing volume, which avoids the saturation of samples having long spin relaxation times and, consequently, the degradation of the spin sensitivity. The oscillator operates at 35 GHz, consuming 90 μW at 300 K and 15 μW at 1.4 K. This is, to the best of my knowledge, the lowest power consumption reported to date for oscillators operating in the same frequency range. The fully integrated oscillator is based on a single HEMT transistor having a gate length of 70 nm and realized using a 2DEG in In$_{0.7}$Ga$_{0.3}$As. The chip area is about 0.3 mm^2. The spin sensitivity is 3×10^8 spins/Hz$^{1/2}$ at 300 K and 1.2×10^7 spins/Hz$^{1/2}$ at 10 K.

The ESR sensor based on integrated microwave oscillators, presented in section 4.3, achieved a minimum power consumption of 90 μW at room temperature with operation at 11 GHz [94, 169]. Here, we propose a sensor operating at 35 GHz with the same power consumption but with an improvement of the spin sensitivity by a factor 50 (which reduces the required measurement time by a factor 2500) compared to the 11 GHz design. The sensitivity improvement is obtained by the combined effect of a factor 10 for the frequency increase (from 11 GHz to 35 GHz) and of a factor of 25 because of the reduction of the coil size (from 400 × 480 μm^2 to 140 × 160 μm^2), which largely compensate for the increase of the frequency noise of a factor 4 (from 17 Hz/Hz$^{1/2}$ to 80 Hz/Hz$^{1/2}$).

It is important to notice that, compared to the large majority of the reported microwave oscillators used for other applications [220, 241–246] (see Table 4.3), the use of the oscillator as detector for ESR spectroscopy demands different key-performance and, hence, a different
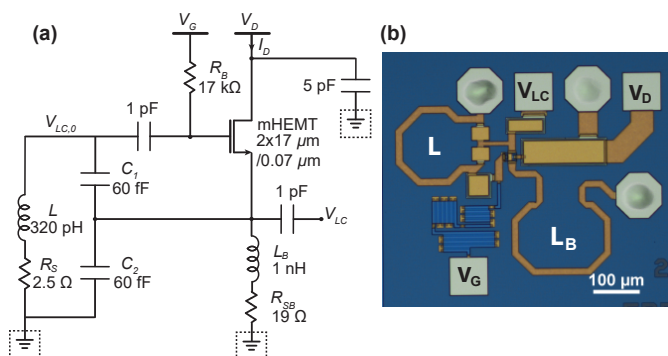
Figure 4.5: **Schematic and picture of 35 GHz HEMT ESR detector.** (a) Schematic and (b) picture of the 35 GHz Colpitts HEMT oscillator used as a detector for ESR spectroscopy. The ESR sensing coil L is the one on the top left part of the picture.
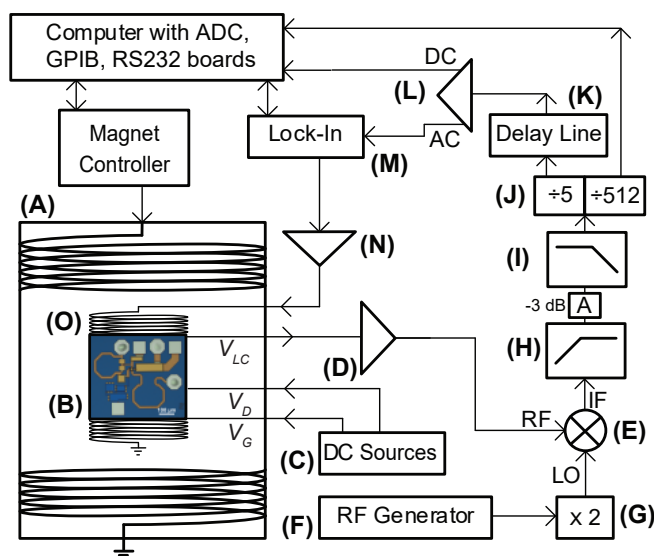
Figure 4.6: **Block diagram of the complete setup for the characterization of the integrated 35 GHz HEMT oscillator as sensor for ESR spectroscopy.** (A) Superconducting magnet with variable temperature insert (1.4 to 300 K, 0 to 9.4 T, Cryogenic Ltd); (B) HEMT LC Colpitts oscillator; (C) DC power supplies (Keithley 2400); (D) high frequency amplifier (Pasternack PE15A3300); (E) down conversion mixer (Marki Microwave MM1-1857L); (F) RF generator (Rohde&Schwarz SMR-20); (G) frequency multiplier (Marki Microwave ADA-2052); (H) 100 MHz high-pass filter (Crystek CHPFL-0100); (I) 300 MHz low-pass filter (Crystek CLPFL-0300); (J) frequency divider (Valon Technology 3010); (K) home-made delay-line-discriminator [129, 240] (200 MHz central frequency, 1 MHz detection range, 5 MHz FM bandwidth); (L) amplifier (Stanford Research Systems SR560); (M) lock-in amplifier (EG&G 7265); (N) power amplifier (Rohrer PA508); (O) home-made modulation coil (1.9 mT/A).

Table 4.2: Key-Features of the 35 GHz HEMT ESR detector

	300 K	1.4 K
Oscillation frequency [GHz]	34.5	34.8
Coil size [μm^2]	140 x 160	140 x 160
Coil inductance [pH]	320	-
Coil resistane [Ω]	2.5	-
Coil quality factor	30	-
$V_{DD_{min}}$ [mV]	240	110
$I_{DD_{min}}$ [μA]	380	140
P_{min} [μW]	90	15
Frequency noise [Hz/Hz$^{1/2}$] @ 100 kHz	80	30
Figure of merit [dBc/Hz][*] @100 kHz offset from the carrier	184	200
Minimum B_{1e} [μT]	1[***]	-
Maximum B_{1e} [μT]	16[***]	-
Spin sensitivity [spins/Hz$^{1/2}$]	3×10^8	1.2×10^{7}[**]

[*] The oscillator figure-of-merit (FOM) is computed as $(20\log(f_{LC}/f_{OS}) - \mathcal{L}(f_{OS}) - 10\log(P_{min}))$, where $\mathcal{L}(f_{OS})$ is the phase noise (in dBc/Hz) at the frequency offset f_{OS} (in Hz), f_{LC} is the oscillator working frequency (in Hz), and P_{min} is the minimum power consumption (in mW) [229].

[**] The spin sensitivity is given for 10 K. At 1.4 K, the spin sensitivity is reduced because of proximity with the antiferromagnetic transition of BDPA [94, 237].

[***] At the center of the ESR microcoil (computed from the microwave currents in the ESR microcoil obtained by ADS simulations).

design optimization. For example, the phase noise is of crucial importance also for the ESR spectroscopy application, but a low power consumption and a low value for the microwave field in the sensing volume of the oscillator coil are particularly important for our application, which requires, in turn, a compromise with the phase noise. Additionally, since we obtain the spectroscopic ESR information from the oscillator frequency variation as a function of the applied magnetic field, the output microwave power is not directly relevant for our application.

4.4.1 Description of the oscillator and measurement setup

The single chip 35 GHz HEMT ESR detector is manufactured using an HEMT technology having a minimum gate length of 70 nm (D007IH mHEMT, OMMIC, France). The transistor channel consist of a 2DEG in $In_{0.7}Ga_{0.3}As$. Fig. 4.5(a) shows the detailed schematic of the designed oscillator, which utilizes a common drain Colpitts topology. The current source
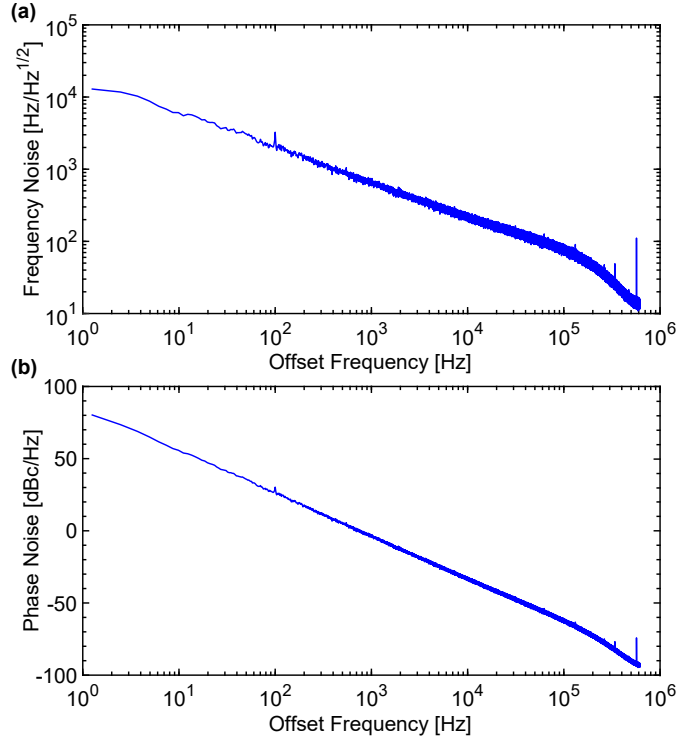
Figure 4.7: **Frequency noise (a) and phase noise (b) at 300 K.** The two quantities are related by $\mathscr{L}(f_{OS}) = 20\log(FN(f_{OS})/f_{OS})$, where FN is the frequency noise (in $\text{Hz}/\text{Hz}^{1/2}$), $L(f_{OS})$ is the phase noise (in dBc/Hz) and f_{OS} is the offset frequency from the carrier (in Hz).

at the source node of the single HEMT transistor is replaced with a biasing inductor L_B as suggested in section 4.3 to reduce the power consumption. The inductor L and capacitors C_1 and C_2 form the resonator, while C_1 and C_2 also provide the positive feedback. Since the DC voltage of the source node is fixed to ground, a second bias node V_G is introduced in the new design, which is DC decoupled from the resonator with a 1 pF capacitor. In order to block RF signals at the bias node a large resistor R_B is placed in series to the bias node. The operating frequency of the oscillator depends on the bias voltages V_D and V_G, and on the temperature, with an overall range from 34.2 to 34.8 GHz. The integrated Colpitts LC oscillator has a size of 0.58×0.5 mm^2 (see Fig. 4.5(b)).

Fig. 4.6 shows the block diagram of the set-up used to characterize the HEMT LC Colpitts oscillator as sensor for ESR spectroscopy. The signal at the output of the oscillator is down-converted to 1 GHz and divided by 5 to match the central frequency of a homemade delay-line-discriminator (DLD) [129, 240], which performs the frequency-to-voltage conversion. The divide-by-512 output of the same divider is connected to a frequency counter of a digital acquisition (DAQ) board, used to acquire the frequency of the oscillator at different bias voltages. The amplifiers shown in the block diagram are used to match the dynamic range of the frequency dividers and of the analog-to-digital-converters of the DAQ board. The filters are used to improve the spectral purity of the signals. Field modulation with lock-in synchronous
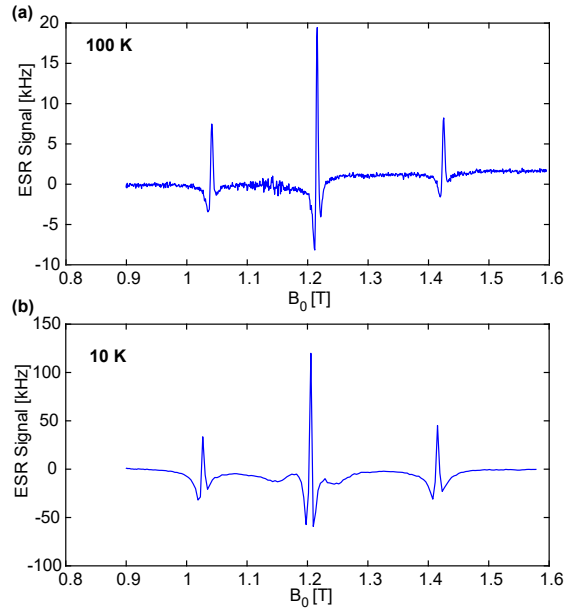
Figure 4.8: **ESR spectra of a ruby sapphire (Cr^{3+}:Al_2O_3 with a Cr^{3+} concentration of 1%) sphere having a diameter of 122 μm at 100K (a) and 10 K (b).** Experimental conditions: microwave magnetic field $B_1 \cong 1$ μT (simulated), frequency of the magnetic field modulation ν_m = 96 kHz, amplitude of the modulation magnetic field $B_m \cong 0.4$ mT, equivalent noise bandwidth of the lock-in amplifier δf = 2.5 Hz, time interval of the magnetic field sweep $t_s \cong 2$ min.

demodulation is used, as in conventional continuous-wave ESR spectroscopy.

4.4.2 Measurements

In this section, we report the results of measurements performed on the 35 GHz LC Colpitts oscillator. In particular, we investigated the start-up condition and the frequency noise. ESR spectra are also reported. In addition to the conventional representation of the oscillator noise in terms of phase noise, we show also the frequency noise, because it is directly related to the sensitivity characterization of the oscillator. The ESR signal correspond to a frequency variation of the oscillator in Hz, so to evaluate the signal-to-noise ratio (and, finally the spin sensitivity) the most direct representation of the noise is the frequency noise in Hz/Hz$^{1/2}$.

In Table 4.2 we report the key features of the realized oscillator. The spin sensitivity (in spins/Hz$^{1/2}$) is estimated using a sample of BDPA (α,γ-bisdiphenylene-β-phenylallyl complex with benzene, Merck 152560) and computed as N_{min}=($3N/SNR$) where N is the number of spins in the sample and SNR is the ratio between the ESR signal (in Hz) and the frequency noise FN (in Hz/Hz$^{1/2}$). From 300 K to 30 K, the spin sensitivity follows the Curie law, and the sensitivity is inversely proportional to the temperature. Below 10 K the signal amplitude decreases, probably due to the proximity with the antiferromagnetic transition of BDPA

Table 4.3: Comparison with relevant state-of-the-art microwave oscillators at 300 K

	Tech	f_0	d	$P_{DD_{min}}$	$\mathscr{L}$(100 kHz)	FN @100 kHz	FOM @100 kHz	B_1	N_{min}
		[GHz]	[μm]	[mW]	[dBc/Hz]	[Hz/Hz$^{1/2}$]	[dBc/Hz]	[μT]	[spins/Hz$^{1/2}$]
This work	pHEMT 70 nm	34.5	150	0.09	-62 -	80	184	1	3×10^8
[94]	pHEMT 70 nm	11	440	0.09	-74	20	185	0.4	8×10^{10}
[74]	CMOS 40 nm	50	120	0.95	-61	90	175	100	10^8
[93]	CMOS 130 nm	27	95	200	-74	20	148	300	10^8
[220]	SiGe 130 nm	30	-	37	-80	10	174	-	-
[241]	CMOS 65 nm	24	80	4.8	-84	6	185	-	-
[242]	CMOS 16 nm	27.5	80	4	-80	10	183	-	-
[243]	CMOS 40 nm	31	130	9	-78	13	178	-	-
[244]	CMOS 180 nm	25	-	3.1	-81	9	184	-	-
[245]	CMOS 130 nm	48	80	5.5	-75	18	181	-	-
[246]	CMOS 65 nm	30	-	3	-76	16	181	-	-

[94, 237]. The minimum and maximum B_{1e} at the center of the ESR microcoil are estimated to be 1 μT and 16 μT at room temperature according to the circuit simulations, respectively. They are calculated as $B_{1e} = \mu_0 I_{RF}^{pp}/4d$ where d is the average coil diameter and I_{RF}^{pp} is the peak-to-peak RF current in the coil. Average coil diameter is 150 μm and the minimum and the maximum peak-to-peak RF currents are simulated as 0.5 mA and 8 mA in ADS, respectively.

In Fig. 4.7(a) and (b), we report the experimentally measured frequency and phase noise of the oscillator. The voltage spectral density at the output of the DLD is measured and the frequency noise is calculated using the frequency-to-voltage conversion ratio of the DLD. The noise spectrum follows the flicker noise ($1/f$) behavior up to 100 kHz. The amplifier ((L) in Fig. 4.6) in the measurement chain contains a low pass filter at 300 kHz, which can be seen in the noise measurement. The measured frequency noise of the microwave oscillator at 100 kHz offset from the carrier is 80 Hz/Hz$^{1/2}$ at 300 K. The frequency noise is reduced approximately by a factor of 3 at 1.4 K.

Fig. 4.8 shows ESR spectra obtained with a Cr^{3+}:Al_2O_3 (Ruby G10, Saphirwerk Industrieprodukt AG) sphere having a diameter of 122 μm at 100 K and 10 K. The concentration of Cr^{3+} ions is about 1%. The sample is placed in the center of the excitation/detection oscillator coil L (see Fig.4.5). The high field part of its spectrum consists of 3 lines, in agreement with previous studies of the same sample [74].

In this section, we designed and characterized a low power 35 GHz LC Colpitts oscillator based on a single HEMT transistor as sensor for ESR spectroscopy. In comparison to the low power HEMT based ESR detector operating at 11 GHz reported in Section 4.3, the measured frequency noise is increased by a factor of about 4 at room temperature and a factor of 6 at 1.4 K. However, thanks to the frequency increase to 35 GHz and the reduction of the coil size, the spin sensitivity N_{min} of the detector (which is proportional to $f_0{}^2 d^3/FN$, where f_0 is the operating frequency, d is the coil diameter, and FN is the frequency noise in $Hz/Hz^{1/2}$) is improved by a factor of 50 compared to the 11 GHz detector [169]. The resulting spin sensitivity of the oscillator measured with a sample of BDPA is 3×10^8 spins/$Hz^{1/2}$ at 300 K and 1.2×10^7 spins/$Hz^{1/2}$ at 10 K. Previously reported single chip CMOS based ESR sensors in the same frequency range [74] have achieved a similar spin sensitivity. However, their much higher power consumption (in the order of 1 mW) and higher microwave magnetic field (in the order of 0.1 mT) makes them significantly less suitable for low temperature operation and for samples having long spin relaxation times with respect to the single chip HEMT based ESR sensor reported in this work.

5 Conclusions and outlook

In this thesis, the integration on a single silicon chip of DNP microsytems consisting of NMR and ESR detectors are demonstrated for the first time. In chapter 2, a single chip DNP microsystem operating at 10.7 GHz(ESR)/16 MHz(NMR) and integrated in a CMOS chip is presented. In chapter 3, a single chip DNP microsystem and a single chip DNP array microsystem operating at 200 GHz(ESR)/300 MHz(NMR) and integrated in a SiGe:BiCMOS chip are reported. In chapter 4, the possibility of the integration of single chip DNP microsystems in an $In_{0.7}Ga_{0.3}As$ HEMT chip is investigated and ESR detectors operating up to 35 GHz are described.

Single chip 10 GHz DNP microsystem

The first single chip DNP microsystem operates at 10.7 GHz(ESR)/16 MHz(NMR) and has a CMOS integrated chip area of less than 2 mm^2. This microsystem consists of an oscillator as ESR detector which works at 10.7 GHz and a broadband transceiver as NMR detector which works up to 1 GHz. Continuous wave ESR experiments, pulsed NMR experiments and DNP-enhanced NMR experiments are performed on liquid samples as well as solid samples. Room temperature measurements on TEMPOL/H_2O solutions show Overhauser enhancements as large as 50 on samples having an effective volume of about 1 nL and on BDPA doped polymers show solid effect enhancements as large as 20 on samples having an effective volume of about 1 nL.

In the following, the foreseen improvements and extensions of the single chip 10 GHz DNP microsystem are discussed.

1. With a redesign of the input stage of the NMR amplifier to increase its input impedance, as discussed in chapter 2.4, it would be possible to increase of the microwave magnetic field B_{1e} and reach higher enhancements.

2. Preliminary measurements performed with the 10 GHz DNP microsystem proposed in this work show that it can be operated also at temperatures down to 4 K, at least. Hence, the single-chip DNP approach proposed here could be well suited also for the study of

DNP processes other then the Overhauser in liquids and solid effects in polymers at room temperature.

3. The 10 GHz DNP microsystem can be combined with a permanent magnet and create a miniaturized bench top DNP system for the study of nanoliter samples.

4. Despite the generally lower enhancement factors observed in liquid state DNP at high magnetic fields, a very significant improvement of the SNR (and of the spectral separation of chemically shifted signals) can be obtained by increasing the operating frequency of the NMR/ESR subsystems [100]. A moderate increase of the frequency to the 40 GHz(ESR)/60 MHz(NMR) region could allow for low-cost DNP-enhanced NMR spectrometers for nanoliter samples in permanent magnets.

Single chip 200 GHz DNP microsystems

The second single chip DNP microsystem is integrated in a SiGe:CMOS chip area of less than 1 mm^2 and operates at 200 GHz(ESR)/300 MHz(NMR). In chapter 3, we demonstrated, for the first time, the possibility to extend the single chip approach to the realization of probes for DNP studies of subnanoliter samples at magnetic fields up to 7 T and temperatures down to 15 K. This microsystem consists of a 200 GHz oscillator as ESR detector and a broadband receiver as NMR detector which works up to 1 GHz. The ESR excitation and the amplitude detection are performed on-chip without the need of external microwave signals and of microwave connection. Measurements on 2% BDPA:PS sample show solid effect enhancements as large as 50 and 10 on samples having an effective volume of about 2 nL and 125 pL at 15 K and 100 K, respectively. The single chip DNP array microsystem operating at 200 GHz(ESR)/300 MHz(NMR) is reported to demonstrate the possibility of arrays of such microsystems. The array microsystem has four frequency locked 200 GHz oscilators as ESR detectors and a broadband receiver as an NMR detector which works up to 1 GHz. It is integrated on a SiGe:BiCMOS chip area of less than 1 mm^2. Measurements on 2% BDPA:PS sample show enhancements as large as 20 on samples having an effective volume of about 1 nL at 200 K.

In the following, the foreseen improvements and extensions of the 200 GHz DNP microsystems are discussed.

1. The 200 GHz single chip DNP microsystem and the 200 GHz single chip DNP array microsystem have been characterized down to 15 K and 200 K, respectively. Depending on the available cooling power, measurements down to 10 K and possibly below might be feasible.

2. The experiments performed with the single chip 200 GHz DNP microsystem on solid samples having short T_2^* suffered from the presense of a large background signal. This problem can be solved using a ceramic or polytetrafluorethylen (PTFE) PCB as a support for the chip.

3. The NMR excitation coil and the transmitter can be integrated on the same chip (similarly to the single chip 10 GHz DNP microsystem reported in chapter 2) to drastically reduce the NMR background signals, hence allowing for a more accurate determination of the DNP enhancement.

4. Pseudo-pulsed DNP experiments can be performed using the frequency tunability of the single chip 200 GHz microsystems. An experimental scheme to perform pulsed ESR measurements with frequency tunable single chip ESR detectors is reported in Ref. [142].

5. The microwave magnetic field B_{1e} generated by 200 GHz oscillators can be increased to achieve higher enhancements in room temperature solid effect experiments. High frequency oscillators with large powers are found in the literature [84,247]. However, due to the high power consumption of these oscillators, the operation at lower temperatures might be limited by the available cooling power.

6. The use of state-of-the-art submicrometer integrated circuit technologies should allow the extension of the single-chip DNP microsystem approach proposed here up to the THz(ESR)/GHz(NMR) region [175,229,248], corresponding the strongest static magnetic fields currently available, while keeping a broad temperature range from 300 K down to a few K.

Single chip DNP microsystems

In the following the foreseen improvements that are applicable to all single chip DNP microsystems proposed in this thesis are discussed.

1. An interesting opportunity offered by the single-chip approach is the possibility to create dense arrays of such sensors for parallel DNP-enhanced NMR spectroscopy of a large number of nanoliter and subnanoliter different samples (or a bigger volume of the same sample). Integrated arrays of NMR detectors [44, 48] as well as ESR detectors [96–99] have been previously reported. A single chip DNP array microsystem consisting of four frequency locked 200 GHz oscillators is reported in section 3.6 of this thesis. Recently, an array of 32 frequency locked oscillators operating at 263 GHz was reported [96].

2. DNP experiments on solid samples are often performed with magic angle spinning (MAS) to improve the spectral resolution. There are two possible solutions to add MAS in our single chip DNP microsystem approach. One of them is the spinning of the chip together with the sample. This would require inductive coupling for all necessary connections such as bias voltages, input signals and output signal. The second solution is the optical MAS of small samples. This study is being carried out by Marti et al. at ETH Zurich [249]. The goal of the optical MAS is to exceed the maximum frequency limit of the current MAS techniques by an order of magnitude

using optically trapped microspheres. First model samples are polyethylene, gamma-irradiated alanine and silica spheres of approximately 20-40 micrometers diameter [249]. Successful trapping of the samples has been performed in close proximity to the single chip microsystems reported in this thesis and ESR measurements of gamma-irradiated alanine have been performed with our ESR detectors. The next step will be the combination of these experiments to show optical MAS DNP experiments using single chip DNP microsystems.

3. NMR experiments on subnanoliter biological samples using a single chip NMR detector have been recently reported [250–253]. An interesting extension would be the use of the single chip DNP microsystems realized in this thesis for such experiments with the addition of suitable biocompatible polarizing agents. The samples could be confined into microfluidic reservoirs at a distance of about 10 μm from the chip surface. This microfluidic reservoir size would allow to perform ESR excitation/detection and NMR excitation/detection of the same volumes.

Single chip HEMT microsystems

The goal of the work presented in chapter 4 was to design ultra low power microwave oscillators for ESR excitation and detection, and to investigate their characteristics at different temperatures for the future application of low power single chip DNP microsystems that will be able to operate around and below 1 K.

Firstly, the low power HEMT LC Colpitts oscillator operating at 11 GHz is reported. In particular, the minimum power consumption to sustain stable oscillations and the phase noise in the temperature range from 1.4 to 300 K are investigated. Secondly, a 35 GHz low power microwave LC Colpitts oscillator based on a single HEMT transistor as an ESR detector is designed and characterized. The realized 11 and 35 GHz oscillators show the lowest power consumption reported in the literature for LC oscillators working in their frequency range. The 11 GHz oscillator consumes 90 μW and 4 μW, where as the 35 GHz oscillator consumes 90 μW and 15 μW at 300 K and 1.4 K, respectively. In comparison to the 11 GHz counterpart, the measured frequency noise of the 35 GHz low power HEMT based ESR detector is 4 times higher at room temperature as well as at 1.4 K. However, thanks to the increased frequency and the reduction of the coil size, the spin sensitivity N_{min} of the 35 GHz detector is improved by a factor of 50 compared to the 11 GHz detector. The resulting spin sensitivity of the 35 GHz oscillator measured with a sample of BDPA is 3×10^8 spins/Hz$^{1/2}$ at 300 K and 1.2×10^7 spins/Hz$^{1/2}$ at 10 K. Previously reported single chip CMOS based ESR sensors in the same frequency range [74] have achieved a similar spin sensitivity. However, their much higher power consumption (in the order of 1 mW) and higher microwave magnetic field (in the order of 0.1 mT) makes them significantly less suitable for low temperature operation and for samples having long spin relaxation times with respect to the single chip HEMT based ESR sensor reported in this thesis.

To sum up the key points, it was possible to achieve low power consumption in the single chip HEMT ESR detectors reported in this thesis thanks to (1) the high mobility of the HEMT transis-

tor (with respect to standard CMOS), (2) to the reduced threshold voltage at low temperature, and (3) to a design optimization aimed at this specific goal. A reduced power consumption is of crucial importance for measurements at low temperatures. At temperatures below 1 K, the limited effective cooling power of ^{3}He and ^{3}He^{4}He dilution refrigerator systems demands for devices operating with power in the μW range and below, especially if the power has to be dissipated in a very small volume, such as the channel of an HEMT transistor suitable to operate at microwave frequencies above 10 GHz.

In the following, we discuss the foreseen improvements and extensions of ESR detectors based on HEMT technnology.

1. It is certainly interesting to study the oscillator behavior in the condition $\hbar\omega > kT$, where we expect to observe a significant reduction of the thermal noise and, possibly, also an observable quantum behavior related to the oscillator energy quantization coupled with the non linear behavior of the transistor. *LC* resonators operating in the condition $\hbar\omega > k_B T$ are, in principle, possible candidates to show a macroscopic quantum behavior however, due to their linear behavior, the energy (frequency) quantization is not observable [254].The *LC* oscillators described in this work show a relatively strong dependence of the oscillator frequency on the applied bias voltage, which make these oscillators highly anharmonic. This condition might be sufficient to observe interesting unexplored phenomena, which might include their behavior as artificial atoms, as reported before for superconducting quantum circuits (SQC) based on Josephson junctions [254, 255]. The 11 GHz and 35 GHz HEMT oscillators realized in this thesis are, most probably, able to operate at temperatures below 1 K and, hence, in the condition $\hbar\omega > k_B T$ (i.e. $f > 20$ GHz/K).

2. The 11 GHz and 35 GHz HEMT detectors can be combined with an NMR detector to realize a single chip DNP microsystem that can operate at 1 K and, possibly, below.

Comments on integrated circuit technologies

In this thesis, the single chip integrated magnetic resonance detectors are realized in CMOS, SiGe:BiCMOS and In$_{0.7}$Ga$_{0.3}$As HEMT integrated circuit technologies. Each of these technologies have certain advantages and disadvantages compared to the others. Generally, CMOS technologies have the lowest cost, moderate power consumption, and the highest integration level. However their high frequency performance is lower compared to SiGe:BiCMOS and HEMT technologies and their cost is increasing for higher performance nodes. HEMT technologies are the optimum for very high frequency and low power consumption circuitry, but there are less metal layers available in the technology and the quality of these metal layers and connections between them are much lower compared to CMOS and SiGe:BiCMOS technologies which result in lower integration levels. SiGe:BiCMOS technology provides, most probably, the best compromise between high frequency, high microwave magnetic field B_{1e} and the high integration level with the availability of CMOS transistors and high performance

SiGe HBT transistors. The drawback of this technology is the need of high power consumption for the high microwave magnetic field B_{1e}, which limits the operation at low temperatures. At temperatures below 1 K, the use of HEMT technologies are most probably a better approach because of their higher electron mobility.

Bibliography

[1] S. Fan, Q. Zhou, K.-M. Lei, P.-I. Mak, R. P. Martins, Miniaturization of a nuclear magnetic resonance system: Architecture and design considerations of transceiver integrated circuits, IEEE Transactions on Circuits and Systems I: Regular Papers 69 (8) (2022) 3049–3060.

[2] M. Rosay, M. Blank, F. Engelke, Instrumentation for solid-state dynamic nuclear polarization with magic angle spinning nmr, Journal of Magnetic Resonance 264 (2016) 88–98.

[3] R. W. Hooper, B. A. Klein, V. K. Michaelis, Dynamic nuclear polarization (dnp) 101: A new era for materials, Chemistry of Materials 32 (11) (2020) 4425–4430.

[4] Y. Hu, K. Cheng, L. He, X. Zhang, B. Jiang, L. Jiang, C. Li, G. Wang, Y. Yang, M. Liu, Nmr-based methods for protein analysis, Analytical chemistry 93 (4) (2021) 1866–1879.

[5] M. Pellecchia, D. S. Sem, K. Wüthrich, Nmr in drug discovery, Nature Reviews Drug Discovery 1 (3) (2002) 211–219.

[6] V. S. Lee, Mri: From science to society, Journal of Magnetic Resonance Imaging 37 (4) (2013) 753–760.

[7] J. Eills, D. Budker, S. Cavagnero, E. Y. Chekmenev, S. J. Elliott, S. Jannin, A. Lesage, J. Matysik, T. Meersmann, T. Prisner, et al., Spin hyperpolarization in modern magnetic resonance, Chemical Reviews 123 (4) (2023) 1417–1551.

[8] T. Prisner, W. Koeckenberger, Dynamic nuclear polarization: new experimental and methodology approaches and applications in physics, chemistry, biology and medicine, Applied Magnetic Resonance 34 (3-4) (2008) 213–218.

[9] K. K. Frederick, V. K. Michaelis, B. Corzilius, T.-C. Ong, A. C. Jacavone, R. G. Griffin, S. Lindquist, Sensitivity-enhanced nmr reveals alterations in protein structure by cellular milieus, Cell 163 (3) (2015) 620–628.

[10] K. Tagami, R. Thicklin, S. Jain, A. Equbal, M. Li, T. Zens, A. Siaw, S. Han, Design of a cryogen-free high field dual epr and dnp probe, Journal of Magnetic Resonance 347 (2023) 107351.

Bibliography

[11] D. L. Olson, T. L. Peck, A. G. Webb, R. L. Magin, J. V. Sweedler, High-resolution microcoil ^{1}H-NMR for mass-limited, nanoliter-volume samples, Science 270 (5244) (1995) 1967–1970.

[12] A. G. Webb, Radiofrequency microcoils in magnetic resonance, Prog. Nucl. Mag. Res. SP. 31 (1) (1997) 1–42.

[13] M. E. Lacey, R. Subramanian, D. L. Olson, A. G. Webb, J. V. Sweedler, High-resolution NMR spectroscopy of sample volumes from 1 nl to 10 μl, Chem. Rev. 99 (10) (1999) 3133–3152.

[14] K. R. Minard, R. A. Wind, Picoliter ^{1}H NMR spectroscopy, J. Magn. Reson. 154 (2) (2002) 336–343.

[15] C. Massin, F. Vincent, A. Homsy, K. Ehrmann, G. Boero, P. A. Besse, A. Daridon, E. Verpoorte, N. De Rooij, R. S. Popovic, Planar microcoil-based microfluidic NMR probes, J. Magn. Reson. 164 (2) (2003) 242–255.

[16] D. Sakellariou, G. Le Goff, J. F. Jacquinot, High-resolution, high-sensitivity NMR of nanolitre anisotropic samples by coil spinning, Nature 447 (7145) (2007) 694–697.

[17] Y. Maguire, I. L. Chuang, S. Zhang, N. Gershenfeld, Ultra-small-sample molecular structure detection using microslot waveguide nuclear spin resonance, Proc. Natl. Acad. Sci. U.S.A. 104 (22) (2007) 9198–9203.

[18] H. G. Krojanski, J. Lambert, Y. Gerikalan, D. Suter, R. Hergenröder, Microslot NMR probe for metabolomics studies, Anal. Chem. 80 (22) (2008) 8668–8672.

[19] J. Bart, A. J. Kolkman, A. J. Oosthoek-de Vries, K. Koch, P. J. Nieuwland, H. Janssen, J. van Bentum, K. A. Ampt, F. P. Rutjes, S. S. Wijmenga, et al., A microfluidic high-resolution NMR flow probe, J. Am. Chem. Soc. 131 (14) (2009) 5014–5015.

[20] S. S. Zalesskiy, E. Danieli, B. Blumich, V. P. Ananikov, Miniaturization of NMR systems: Desktop spectrometers, microcoil spectroscopy, and "NMR on a chip" for chemistry, biochemistry, and industry, Chem. Rev. 114 (11) (2014) 5641–5694.

[21] G. Finch, A. Yilmaz, M. Utz, An optimised detector for in-situ high-resolution NMR in microfluidic devices, J. Magn. Reson. 262 (2016) 73–80.

[22] Y. Chen, H. S. Mehta, M. C. Butler, E. D. Walter, P. N. Reardon, R. S. Renslow, K. T. Mueller, N. M. Washton, High-resolution microstrip NMR detectors for subnanoliter samples, Phys. Chem. Chem. Phys. 19 (41) (2017) 28163–28174.

[23] A. Blank, Y. Twig, Y. Ishay, Recent trends in high spin sensitivity magnetic resonance, Journal of Magnetic Resonance 280 (2017) 20–29.

[24] C. Eichler, A. Sigillito, S. A. Lyon, J. R. Petta, Electron spin resonance at the level of 1 0 4 spins using low impedance superconducting resonators, Physical review letters 118 (3) (2017) 037701.

[25] A. Bienfait, J. Pla, Y. Kubo, M. Stern, X. Zhou, C. Lo, C. Weis, T. Schenkel, M. Thewalt, D. Vion, et al., Reaching the quantum limit of sensitivity in electron spin resonance, Nature nanotechnology 11 (3) (2016) 253–257.

[26] P. Haikka, Y. Kubo, A. Bienfait, P. Bertet, K. Mølmer, Proposal for detecting a single electron spin in a microwave resonator, Physical Review A 95 (2) (2017) 022306.

[27] Y. Artzi, Y. Twig, A. Blank, Induction-detection electron spin resonance with spin sensitivity of a few tens of spins, Applied Physics Letters 106 (8) (2015) 084104.

[28] N. Wu, T. L. Peck, A. G. Webb, R. L. Magin, J. V. Sweedler, Nanoliter volume sample cells for 1h nmr: application to online detection in capillary electrophoresis, Journal of the American Chemical Society 116 (17) (1994) 7929–7930.

[29] A. Webb, Radiofrequency microcoils for magnetic resonance imaging and spectroscopy, Journal of Magnetic Resonance 229 (2013) 55–66.

[30] G. Boero, Integrated NMR probe for magnetometry, Hartung-Gorre, 2000.

[31] J. G. Korvink, N. MacKinnon, V. Badilita, M. Jouda, "small is beautiful" in nmr, Journal of Magnetic Resonance 306 (2019) 112–117.

[32] J. Anders, F. Dreyer, D. Krüger, I. Schwartz, M. B. Plenio, F. Jelezko, Progress in miniaturization and low-field nuclear magnetic resonance, Journal of Magnetic Resonance 322 (2021) 106860.

[33] E. Danieli, J. Perlo, B. Blümich, F. Casanova, Small magnets for portable nmr spectrometers, Angewandte Chemie International Edition 49 (24) (2010) 4133–4135.

[34] N. Sun, T. J. Yoon, H. Lee, W. Andress, R. Weissleder, D. Ham, Palm NMR and 1-chip NMR, IEEE J. Solid-State Circuits 46 (1) (2010) 342–352.

[35] A. Magnetics, 125 mhz benchtop nmr spectrometer (2021).
URL https://www.qmagnetics.com/qm-125-features

[36] C. Zhou, J. Tang, Analysis on the operation parameters of cooling water system in 45.22 t hybrid magnet experiment, Case Studies in Thermal Engineering 44 (2023) 102868.

[37] Z. Gan, P. Gor'kov, T. A. Cross, A. Samoson, D. Massiot, Seeking higher resolution and sensitivity for nmr of quadrupolar nuclei at ultrahigh magnetic fields, Journal of the American Chemical Society 124 (20) (2002) 5634–5635.

[38] G. Eidmann, R. Savelsberg, P. Blümler, B. Blümich, The nmr mouse, a mobile universal surface explorer, Journal of Magnetic Resonance, Series A 122 (1) (1996) 104–109.

[39] C. M. Castro, A. A. Ghazani, J. Chung, H. Shao, D. Issadore, T.-J. Yoon, R. Weissleder, H. Lee, Miniaturized nuclear magnetic resonance platform for detection and profiling of circulating tumor cells, Lab on a Chip 14 (1) (2014) 14–23.

[40] W. Tang, W. Wang, A single-board nmr spectrometer based on a software defined radio architecture, Measurement Science and Technology 22 (1) (2010) 015902.

[41] D. Ha, J. Paulsen, N. Sun, Y.-Q. Song, D. Ham, Scalable NMR spectroscopy with semiconductor chips, Proc. Natl. Acad. Sci. U.S.A. 111 (33) (2014) 11955–11960.

[42] K.-M. Lei, P.-I. Mak, M.-K. Law, R. P. Martins, A μNMR CMOS transceiver using a butterfly-coil input for integration with a digital microfluidic device inside a portable magnet, IEEE J. Solid-State Circuits 51 (10) (2016) 2274–2286.

[43] K.-M. Lei, H. Heidari, P.-I. Mak, M.-K. Law, F. Maloberti, R. P. Martins, A handheld high-sensitivity micro-nmr cmos platform with b-field stabilization for multi-type biological/chemical assays, IEEE Journal of solid-state circuits 52 (1) (2016) 284–297.

[44] K.-M. Lei, D. Ha, Y.-Q. Song, R. M. Westervelt, R. Martins, P.-I. Mak, D. Ham, Portable nmr with parallelism, Anal. Chem. 92 (2) (2020) 2112–2120.

[45] J. Handwerker, M. Pérez-Rodas, M. Beyerlein, F. Vincent, A. Beck, N. Freytag, X. Yu, R. Pohmann, J. Anders, K. Scheffler, A cmos nmr needle for probing brain physiology with high spatial and temporal resolution, Nature methods 17 (1) (2020) 64–67.

[46] N. Sahin Solmaz, M. Grisi, A. V. Matheoud, G. Gualco, G. Boero, Single-chip dynamic nuclear polarization microsystem, Analytical Chemistry 92 (14) (2020) 9782–9789.

[47] G. Boero, J. Frounchi, B. Furrer, P. A. Besse, R. S. Popovic, Fully integrated probe for proton nuclear magnetic resonance magnetometry, Rev. Sci. Instrum. 72 (6) (2001) 2764–2768.

[48] J. Anders, G. Chiaramonte, P. SanGiorgio, G. Boero, A single-chip array of NMR receivers, J. Magn. Reson. 201 (2) (2009) 239–249.

[49] J. Anders, P. SanGiorgio, G. Boero, A fully integrated IQ-receiver for NMR microscopy, J. Magn. Reson. 209 (1) (2011) 1–7.

[50] M. Grisi, G. Gualco, G. Boero, A broadband single-chip transceiver for multi-nuclear NMR probes, Rev. Sci. Instrum. 86 (4) (2015) 044703.

[51] J. Anders, P. SanGiorgio, X. Deligianni, F. Santini, K. Scheffler, G. Boero, Integrated active tracking detector for MRI-guided interventions, Magn. Reson. Med. 67 (1) (2012) 290–296.

[52] J. Anders, J. Handwerker, M. Ortmanns, G. Boero, A low-power high-sensitivity single-chip receiver for NMR microscopy, J. Magn. Reson. 266 (2016) 41–50.

[53] M. Grisi, F. Vincent, B. Volpe, R. Guidetti, N. Harris, A. Beck, G. Boero, NMR spectroscopy of single sub-nl ova with inductive ultra-compact single-chip probes, Sci. Rep. 7 (2017) 44670.

[54] B. Sporrer, L. Wu, L. Bettini, C. Vogt, J. Reber, J. Marjanovic, T. Burger, D. O. Brunner, K. P. Pruessmann, G. Tröster, et al., A fully integrated dual-channel on-coil CMOS receiver for array coils in 1.5-10.5 T MRI, IEEE Trans. Biomed. Circuits Syst. 11 (6) (2017) 1245–1255.

[55] E. Montinaro, M. Grisi, M. Letizia, L. Pethö, M. Gijs, R. Guidetti, J. Michler, J. Brugger, G. Boero, 3D printed microchannels for sub-nl NMR spectroscopy, PloS one 13 (5) (2018) e0192780.

[56] M. Grisi, G. M. Conley, P. Sommer, J. Tinembart, G. Boero, A single-chip integrated transceiver for high field NMR magnetometry, Rev. Sci. Instrum. 90 (1) (2019) 015001.

[57] J. Handwerker, M. Pérez-Rodas, M. Beyerlein, F. Vincent, A. Beck, N. Freytag, X. Yu, R. Pohmann, J. Anders, K. Scheffler, A CMOS NMR needle for probing brain physiology with high spatial and temporal resolution, Nat. Methods (2019) 1–4.

[58] J. Anders, K. Lips, Mr to go, Journal of Magnetic Resonance 306 (2019) 118–123.

[59] R. Narkowicz, H. Ogata, E. Reijerse, D. Suter, A cryogenic receiver for epr, Journal of Magnetic Resonance 237 (2013) 79–84.

[60] G. Boero, M. Bouterfas, C. Massin, F. Vincent, P.-A. Besse, R. Popovic, A. Schweiger, Electron-spin resonance probe based on a 100 μm planar microcoil, Review of scientific instruments 74 (11) (2003) 4794–4798.

[61] R. Narkowicz, D. Suter, I. Niemeyer, Scaling of sensitivity and efficiency in planar microresonators for electron spin resonance, Review of Scientific Instruments 79 (8) (2008) 084702.

[62] R. Narkowicz, D. Suter, R. Stonies, Planar microresonators for epr experiments, Journal of Magnetic Resonance 175 (2) (2005) 275–284.

[63] Y. Twig, E. Dikarov, A. Blank, Ultra miniature resonators for electron spin resonance: Sensitivity analysis, design and construction methods, and potential applications, Molecular Physics 111 (18-19) (2013) 2674–2682.

[64] Y. Twig, E. Dikarov, A. Blank, Cryogenic electron spin resonance microimaging probe, Journal of Magnetic Resonance 218 (2012) 22–29.

[65] Y. Twig, A. Sorkin, D. Cristea, A. Feintuch, A. Blank, Surface loop-gap resonators for electron spin resonance at w-band, Review of Scientific Instruments 88 (12) (2017) 123901.

[66] O. Benningshof, H. Mohebbi, I. Taminiau, G. Miao, D. Cory, Superconducting microstrip resonator for pulsed esr of thin films, Journal of Magnetic Resonance 230 (2013) 84–87.

[67] H. Malissa, D. Schuster, A. Tyryshkin, A. A. Houck, S. A. Lyon, Superconducting coplanar waveguide resonators for low temperature pulsed electron spin resonance spectroscopy, Review of scientific instruments 84 (2) (2013) 025116.

[68] A. J. Sigillito, H. Malissa, A. M. Tyryshkin, H. Riemann, N. V. Abrosimov, P. Becker, H.-J. Pohl, M. L. Thewalt, K. M. Itoh, J. J. Morton, et al., Fast, low-power manipulation of spin ensembles in superconducting microresonators, Applied Physics Letters 104 (22) (2014) 222407.

[69] A. Bienfait, J. Pla, Y. Kubo, X. Zhou, M. Stern, C. Lo, C. Weis, T. Schenkel, D. Vion, D. Esteve, et al., Controlling spin relaxation with a cavity, Nature 531 (7592) (2016) 74–77.

[70] S. Probst, A. Bienfait, P. Campagne-Ibarcq, J. Pla, B. Albanese, J. Da Silva Barbosa, T. Schenkel, D. Vion, D. Esteve, K. Mølmer, et al., Inductive-detection electron-spin resonance spectroscopy with 65 spins/hz sensitivity, Applied Physics Letters 111 (20) (2017) 202604.

[71] A. Asfaw, A. Sigillito, A. Tyryshkin, T. Schenkel, S. A. Lyon, Multi-frequency spin manipulation using rapidly tunable superconducting coplanar waveguide microresonators, Applied Physics Letters 111 (3) (2017) 032601.

[72] T. Yalcin, G. Boero, Single-chip detector for electron spin resonance spectroscopy, Rev. Sci. Instrum. 79 (2008) 094–105.

[73] G. Gualco, J. Anders, A. Sienkiewicz, S. Alberti, L. Forro, G. Boero, Cryogenic single-chip electron spin resonance detector, J. Magn. Reson. 247 (2014) 96–103.

[74] A. V. Matheoud, G. Gualco, M. Jeong, I. Zivkovic, J. Brugger, H. Rønnow, J. Anders, G. Boero, Single-chip electron spin resonance detectors operating at 50 GHz, 92 GHz, and 146 GHz, J. Magn. Reson. 278 (2017) 113–121.

[75] D. Rugar, R. Budakian, H. Mamin, B. Chui, Single spin detection by magnetic resonance force microscopy, Nature 430 (6997) (2004) 329–332.

[76] M. Grinolds, M. Warner, K. De Greve, Y. Dovzhenko, L. Thiel, R. L. Walsworth, S. Hong, P. Maletinsky, A. Yacoby, Subnanometre resolution in three-dimensional magnetic resonance imaging of individual dark spins, Nature nanotechnology 9 (4) (2014) 279–284.

[77] S. Baumann, W. Paul, T. Choi, C. P. Lutz, A. Ardavan, A. J. Heinrich, Electron paramagnetic resonance of individual atoms on a surface, Science 350 (6259) (2015) 417–420.

[78] B. Razavi, A 300-ghz fundamental oscillator in 65-nm cmos technology, IEEE Journal of Solid-State Circuits 46 (4) (2011) 894–903.

[79] Y. Zhao, B. Heinemann, U. R. Pfeiffer, Fundamental mode colpitts vcos at 115 and 165-ghz, in: 2011 IEEE Bipolar/BiCMOS Circuits and Technology Meeting, IEEE, 2011, pp. 33–36.

[80] M. Jahn, K. Aufinger, T. Meister, A. Stelzer, 125 to 181 ghz fundamental-wave vco chips in sige technology, in: 2012 IEEE Radio Frequency Integrated Circuits Symposium, IEEE, 2012, pp. 87–90.

[81] M. Jahn, H. Knapp, A. Stelzer, A 122-ghz sige-based signal-generation chip employing a fundamental-wave oscillator with capacitive feedback frequency-enhancement, IEEE journal of solid-state circuits 46 (9) (2011) 2009–2020.

[82] S. P. Voinigescu, A. Tomkins, E. Dacquay, P. Chevalier, J. Hasch, A. Chantre, B. Sautreuil, A study of sige hbt signal sources in the 220–330-ghz range, IEEE Journal of Solid-State Circuits 48 (9) (2013) 2011–2021.

[83] N. Sarmah, B. Heinemann, U. R. Pfeiffer, A 246 ghz fundamental source with a peak output power of 2.8 dbm, in: 2015 10th European Microwave Integrated Circuits Conference (EuMIC), IEEE, 2015, pp. 184–187.

[84] F. Ahmed, M. Furqan, B. Heinemann, A. Stelzer, A sige-based d-band fundamental-wave vco with 9 dbm output power and-185 dbc/hz fomt, in: 2015 IEEE Compound Semiconductor Integrated Circuit Symposium (CSICS), IEEE, 2015, pp. 1–4.

[85] J. Al-Eryani, H. Knapp, J. Wursthorn, K. Aufinger, H. Li, S. Majied, S. Boguth, R. Lachner, J. Bock, L. Maurer, A fundamental 229–240 ghz vco with integrated dynamic frequency divider chain, in: 2016 46th European Microwave Conference (EuMC), IEEE, 2016, pp. 489–492.

[86] U. Ali, M. Bober, A. Thiede, Design of voltage controlled oscillators (vcos) in d-band and their phase noise measurements using frequency down-conversion, in: 2016 11th European Microwave Integrated Circuits Conference (EuMIC), IEEE, 2016, pp. 317–320.

[87] D. Fritsche, S. Li, N. Joram, C. Carta, F. Ellinger, Design and characterization of a 190-ghz voltage-controlled oscillator, in: 2016 46th European Microwave Conference (EuMC), IEEE, 2016, pp. 493–496.

[88] D. Fritsche, P. Stärke, C. Carta, F. Ellinger, A low-power sige bicmos 190-ghz transceiver chipset with demonstrated data rates up to 50 gbit/s using on-chip antennas, IEEE Transactions on Microwave Theory and Techniques 65 (9) (2017) 3312–3323.

[89] H. Bello, L. Pantoli, H. J. Ng, D. Kissinger, G. Leuzzi, Low phase-noise high output power 176-ghz voltage-controlled oscillator in a 130-nm bicmos technology, IET Microwaves, Antennas & Propagation 13 (14) (2019) 2490–2494.

[90] L. Pantoli, H. Bello, H. Ng, D. Kissinger, G. Leuzzi, A compact, low-power and constant output power 330 ghz voltage-controlled oscillator in 130-nm sige bicmos, Journal of Infrared, Millimeter, and Terahertz Waves 41 (2020) 796–809.

[91] M. Seo, M. Urteaga, J. Hacker, A. Young, Z. Griffith, V. Jain, R. Pierson, P. Rowell, A. Skalare, A. Peralta, et al., Inp hbt ic technology for terahertz frequencies: Fundamental oscillators up to 0.57 thz, IEEE Journal of Solid-State Circuits 46 (10) (2011) 2203–2214.

[92] W. Steyaert, P. Reynaert, A 0.54 thz signal generator in 40 nm bulk cmos with 22 ghz tuning range and integrated planar antenna, IEEE Journal of Solid-State Circuits 49 (7) (2014) 1617–1626.

[93] J. Anders, A. Angerhofer, G. Boero, K-band single-chip electron spin resonance detector, J. Magn. Reson. 217 (2012) 19–26.

[94] A. V. Matheoud, N. Sahin, G. Boero, A single chip electron spin resonance detector based on a single high electron mobility transistor, J. Magn. Reson. 294 (2018) 59–70.

[95] B. Schlecker, A. Hoffmann, A. Chu, M. Ortmanns, K. Lips, J. Anders, Towards low-cost, high-sensitivity point-of-care diagnostics using VCO-based ESR-on-a-chip detectors, IEEE Sens. J. 19 (20) (2018) 8995–9003.

[96] A. Chu, M. Kern, K. Khan, K. LiPS, J. Anders, A 263ghz 32-channel epr-on-a-chip injection-locked vco-array, in: 2023 IEEE International Solid-State Circuits Conference (ISSCC), IEEE, 2023, pp. 20–22.

[97] A. Chu, B. Schlecker, K. Lips, M. Ortmanns, J. Anders, An 8-channel 13ghz esr-on-a-chip injection-locked vco-array achieving 200μm-concentration sensitivity, in: 2018 IEEE International Solid-State Circuits Conference-(ISSCC), IEEE, 2018, pp. 354–356.

[98] K. Khan, M. A. Hassan, M. Kern, K. Lips, I. Schwartz, M. Plenio, F. Jelezko, J. Anders, A 12.2 to 14.9 ghz injection-locked vco array with an on-chip 50 mhz bw semi-digital pll for transient spin manipulation and detection, in: 2022 IEEE 65th International Midwest Symposium on Circuits and Systems (MWSCAS), IEEE, 2022, pp. 1–4.

[99] M. A. Hassan, T. Elrifai, A. Sakr, M. Kern, K. Lips, J. Anders, A 14-channel 7 ghz vco-based epr-on-a-chip sensor with rapid scan capabilities, in: 2021 IEEE Sensors, IEEE, 2021, pp. 1–4.

[100] C. Griesinger, M. Bennati, H.-M. Vieth, C. Luchinat, G. Parigi, P. Höfer, F. Engelke, S. J. Glaser, V. Denysenkov, T. F. Prisner, Dynamic nuclear polarization at high magnetic fields in liquids, Prog. Nucl. Mag. Res. SP. 64 (2012) 4–28.

[101] C. P. Slichter, The discovery and renaissance of dynamic nuclear polarization, Rep. Prog. Phys. 77 (7) (2014) 072–501.

[102] G. Liu, M. Levien, N. Karschin, G. Parigi, C. Luchinat, M. Bennati, One-thousand-fold enhancement of high field liquid nuclear magnetic resonance signals at room temperature, Nat. Chem. 9 (7) (2017) 676–680.

[103] B. Plainchont, P. Berruyer, J.-N. Dumez, S. Jannin, P. Giraudeau, Dynamic nuclear polarization opens new perspectives for NMR spectroscopy in analytical chemistry, Anal. Chem. 90 (6) (2018) 3639–3650.

[104] J. H. Ardenkjær-Larsen, B. Fridlund, A. Gram, G. Hansson, L. Hansson, M. H. Lerche, R. Servin, M. Thaning, K. Golman, Increase in signal-to-noise ratio of > 10,000 times in liquid-state NMR, Proc. Natl. Acad. Sci. U.S.A. 100 (18) (2003) 10158–10163.

[105] A. Capozzi, T. Cheng, G. Boero, C. Roussel, A. Comment, Thermal annihilation of photo-induced radicals following dynamic nuclear polarization to produce transportable frozen hyperpolarized ^{13}C-substrates, Nat. Commun. 8 (2017) 15757.

[106] A. Capozzi, J.-N. Hyacinthe, T. Cheng, T. R. Eichhorn, G. Boero, C. Roussel, J. J. van der Klink, A. Comment, Photoinduced nonpersistent radicals as polarizing agents for X-nuclei dissolution dynamic nuclear polarization, J. Phys. Chem. C 119 (39) (2015) 22632–22639.

[107] K. Kouřil, H. Kouřilová, S. Bartram, M. H. Levitt, B. Meier, Scalable dissolution-dynamic nuclear polarization with rapid transfer of a polarized solid, Nat. Commun. 10 (1) (2019) 1–6.

[108] M. Mompeán, R. M. Sánchez-Donoso, A. De La Hoz, V. Saggiomo, A. H. Velders, M. V. Gomez, Pushing nuclear magnetic resonance sensitivity limits with microfluidics and photo-chemically induced dynamic nuclear polarization, Nat. Commun. 9 (1) (2018) 108.

[109] T. Orlando, R. Dervişoğlu, M. Levien, I. Tkach, T. F. Prisner, L. B. Andreas, V. P. Denysenkov, M. Bennati, Dynamic nuclear polarization of ^{13}C nuclei in the liquid state over a 10 T field range, Angew. Chem. 131 (5) (2019) 1416–1420.

[110] J. Eills, W. Hale, M. Sharma, M. Rossetto, M. H. Levitt, M. Utz, High-resolution nuclear magnetic resonance spectroscopy with picomole sensitivity by hyperpolarization on a chip, J. Am. Chem. Soc. 141 (25) (2019) 9955–9963.

[111] S. Z. Kiss, N. MacKinnon, J. G. Korvink, Microfluidic overhauser dnp chip for signal-enhanced compact nmr, Scientific reports 11 (1) (2021) 4671.

[112] R. Griffin, T. Prisner, High field dynamic nuclear polarization—the renaissance, Physical Chemistry Chemical Physics 12 (22) (2010) 5737–5740.

[113] L. R. Becerra, G. J. Gerfen, B. F. Bellew, J. A. Bryant, D. A. Hall, S. J. Inati, R. T. Weber, S. Un, T. F. Prisner, A. E. Mcdermott, et al., A spectrometer for dynamic nuclear polarization and electron paramagnetic resonance at high frequencies, Journal of Magnetic Resonance, Series A 117 (1) (1995) 28–40.

[114] Bruker, Dnp-nmr (2023).
URL https://www.bruker.com/en/products-and-solutions/mr/nmr/dnp-nmr.html

[115] S. Krinner, S. Storz, P. Kurpiers, P. Magnard, J. Heinsoo, R. Keller, J. Luetolf, C. Eichler, A. Wallraff, Engineering cryogenic setups for 100-qubit scale superconducting circuit systems, arXiv preprint arXiv:1806.07862 (Jun. 2018).

Bibliography

[116] R. Schirhagl, K. Chang, M. Loretz, C. L. Degen, Nitrogen-vacancy centers in diamond: nanoscale sensors for physics and biology, Annu. Rev. Phys. Chem. 65 (2014) 83–105.

[117] D. R. Glenn, D. B. Bucher, J. Lee, M. D. Lukin, H. Park, R. L. Walsworth, High-resolution magnetic resonance spectroscopy using a solid-state spin sensor, Nature 555 (7696) (2018) 351–354.

[118] J. Smits, J. T. Damron, P. Kehayias, A. F. McDowell, N. Mosavian, I. Fescenko, N. Ristoff, A. Laraoui, A. Jarmola, V. M. Acosta, Two-dimensional nuclear magnetic resonance spectroscopy with a microfluidic diamond quantum sensor, Sci. Adv. 5 (7) (2019).

[119] D. B. Bucher, D. R. Glenn, H. Park, M. D. Lukin, R. L. Walsworth, Hyperpolarization-enhanced NMR spectroscopy with femtomole sensitivity using quantum defects in diamond, arXiv preprint arXiv:1810.02408 (2018).

[120] D. Rugar, O. Züger, S. Hoen, C. S. Yannoni, H. M. Vieth, R. D. Kendrick, Force detection of nuclear magnetic resonance, Science 264 (5165) (1994) 1560–1563.

[121] C. L. Degen, M. Poggio, H. J. Mamin, C. T. Rettner, D. Rugar, Nanoscale magnetic resonance imaging, Proc. Natl. Acad. Sci. U.S.A. 106 (5) (2009) 1313–1317.

[122] W. Rose, H. Haas, A. Q. Chen, N. Jeon, L. J. Lauhon, D. G. Cory, R. Budakian, High-resolution nanoscale solid-state nuclear magnetic resonance spectroscopy, Phys. Rev. X 8 (1) (2018) 011–030.

[123] S. Schnoz, A. Däpp, A. Hunkeler, B. H. Meier, Detection of liquids by magnetic resonance force microscopy in the gradient-on-cantilever geometry, J. Magn. Reson. 298 (2019) 85–90.

[124] U. Grob, M.-D. Krass, M. Heritier, R. Pachlatko, J. Rhensius, J. Kosata, B. Moores, H. Takahashi, A. Eichler, C. L. Degen, Magnetic resonance force microscopy with a one-dimensional resolution of 0.9 nanometers, Nano Lett. 19 (11) (2019) 7935–7940.

[125] R. G. Griffin, T. M. Swager, R. J. Temkin, High frequency dynamic nuclear polarization: New directions for the 21st century., J. Magn. Reson. 306 (2019) 128–133.

[126] D. Wisser, G. Karthikeyan, A. Lund, G. Casano, H. Karoui, M. Yulikov, G. Menzildjian, A. C. Pinon, A. Purea, F. Engelke, et al., Bdpa-nitroxide biradicals tailored for efficient dynamic nuclear polarization enhanced solid-state nmr at magnetic fields up to 21.1 t, J. Am. Chem. Soc. 140 (41) (2018) 13340–13349.

[127] C. P. Poole, Electron spin resonance: a comprehensive treatise on experimental techniques, Dover Publications Inc., Mineola, NY, USA, 1996.

[128] J. P. Goldsborough, M. Mandel, G. E. Pake, Influence of exchange interaction on paramagnetic relaxation times, Phys. Rev. Lett. 4 (1) (1960) 13.

[129] Hewlett-Packard, USA, Phase noise characterization of microwave oscillators: Frequency Discriminator Method (1985).

[130] M. Gafurov, TEMPOL as a polarizing agent for dynamic nuclear polarization of aqueous solutions, Magn. Reson. Solids 15 (1) (2013) 13103–1.

[131] B. W. Petley, R. W. Donaldson, The temperature dependence of the diamagnetic shielding correction for proton NMR in water, Metrologia 20 (3) (1984) 81.

[132] P. Höfer, P. Carl, G. Guthausen, T. Prisner, M. Reese, T. Carlomagno, C. Griesinger, M. Bennati, Studies of dynamic nuclear polarization with nitroxides in aqueous solution, Appl. Magn. Reson. 34 (3-4) (2008) 393.

[133] P. Höfer, G. Parigi, C. Luchinat, P. Carl, G. Guthausen, M. Reese, T. Carlomagno, C. Griesinger, M. Bennati, Field dependent dynamic nuclear polarization with radicals in aqueous solution, J. Am. Chem. Soc. 130 (11) (2008) 3254–3255.

[134] E. R. McCarney, B. D. Armstrong, M. D. Lingwood, S. Han, Hyperpolarized water as an authentic magnetic resonance imaging contrast agent, Proc. Natl. Acad. Sci. U.S.A. 104 (6) (2007) 1754–1759.

[135] M. T. Türke, I. Tkach, M. Reese, P. Höfer, M. Bennati, Optimization of dynamic nuclear polarization experiments in aqueous solution at 15 MHz/9.7 GHz: a comparative study with DNP at 140 MHz/94 GHz, Phys. Chem. Chem. Phys. 12 (22) (2010) 5893–5901.

[136] N. Enkin, G. Liu, I. Tkach, M. Bennati, High DNP efficiency of TEMPONE radicals in liquid toluene at low concentrations, Phys. Chem. Chem. Phys. 16 (19) (2014) 8795–8800.

[137] M.-T. Türke, G. Parigi, C. Luchinat, M. Bennati, Overhauser DNP with ^{15}N labelled frémy's salt at 0.35 Tesla, Phys. Chem. Chem. Phys. 14 (2) (2012) 502–510.

[138] K. Münnemann, C. Bauer, J. Schmiedeskamp, H. W. Spiess, W. G. Schreiber, D. Hinderberger, A mobile DNP polarizer for clinical applications, Appl. Magn. Reson. 34 (3-4) (2008) 321–330.

[139] T. Asakura, M. Demura, H. Ogawa, K. Matsushita, M. Imanari, NMR imaging of diffusion of small organic molecules in silk fibroin gel, Macromolecules 24 (2) (2018) 620–622.

[140] A. Henstra, P. Dirksen, W. T. Wenckebach, Enhanced dynamic nuclear polarization by the integrated solid effect, Physics Letters A 134 (2) (1988) 134–136.

[141] T. V. Can, J. J. Walish, T. M. Swager, R. G. Griffin, Time domain dnp with the novel sequence, The Journal of chemical physics 143 (5) (2015) 054201.

[142] M. A. Hassan, M. Kern, A. Chu, G. Kalra, E. Shabratova, A. Tsarapkin, N. MacKinnon, K. Lips, C. Teutloff, R. Bittl, et al., Towards single-cell pulsed epr using vco-based epr-on-a-chip detectors, Frequenz 76 (11-12) (2022) 699–717.

Bibliography

[143] M. Kardar, Statistical physics of particles, Cambridge University Press, 2007.

[144] A. Akturk, J. Allnutt, Z. Dilli, N. Goldsman, M. Peckerar, Device modeling at cryogenic temperatures: Effects of incomplete ionization, IEEE transactions on electron devices 54 (11) (2007) 2984–2990.

[145] T. Biedenbander, V. Aladin, S. Saeidpour, B. Corzilius, Dynamic nuclear polarization for sensitivity enhancement in biomolecular solid-state nmr, Chemical Reviews 122 (10) (2022) 9738–9794.

[146] B. Corzilius, High-field dynamic nuclear polarization, Annual review of physical chemistry 71 (2020) 143–170.

[147] T. Prisner, V. Denysenkov, D. Sezer, Liquid state dnp at high magnetic fields: Instrumentation, experimental results and atomistic modelling by molecular dynamics simulations, Journal of Magnetic Resonance 264 (2016) 68–77.

[148] E. V. Kryukov, M. E. Newton, K. J. Pike, D. R. Bolton, R. M. Kowalczyk, A. P. Howes, M. E. Smith, R. Dupree, Dnp enhanced nmr using a high-power 94 ghz microwave source: a study of the tempol radical in toluene, Physical Chemistry Chemical Physics 12 (22) (2010) 5757–5765.

[149] G. Mathies, M. A. Caporini, V. K. Michaelis, Y. Liu, K.-N. Hu, D. Mance, J. L. Zweier, M. Rosay, M. Baldus, R. G. Griffin, Efficient dynamic nuclear polarization at 800 mhz/527 ghz with trityl-nitroxide biradicals, Angewandte Chemie International Edition 54 (40) (2015) 11770–11774.

[150] S. K. Jawla, R. G. Griffin, I. A. Mastovsky, M. A. Shapiro, R. J. Temkin, Second harmonic 527-ghz gyrotron for dnp-nmr: Design and experimental results, IEEE transactions on electron devices 67 (1) (2019) 328–334.

[151] A. Lund, G. Casano, G. Menzildjian, M. Kaushik, G. Stevanato, M. Yulikov, R. Jabbour, D. Wisser, M. Renom-Carrasco, C. Thieuleux, et al., Tinypols: a family of water-soluble binitroxides tailored for dynamic nuclear polarization enhanced nmr spectroscopy at 18.8 and 21.1 t, Chemical Science 11 (10) (2020) 2810–2818.

[152] V. K. Michaelis, R. G. Griffin, B. Corzilius, S. Vega, Handbook of high field dynamic nuclear polarization, John Wiley & Sons, 2019.

[153] Y. Matsuki, T. Idehara, J. Fukazawa, T. Fujiwara, Advanced instrumentation for dnp-enhanced mas nmr for higher magnetic fields and lower temperatures, Journal of Magnetic Resonance 264 (2016) 107–115.

[154] J. Anders, F. Dreyer, D. Krüger, I. Schwartz, M. B. Plenio, F. Jelezko, Progress in miniaturization and low-field nuclear magnetic resonance, Journal of Magnetic Resonance 322 (2021) 106860.

[155] S. Künstner, A. Chu, K.-P. Dinse, A. Schnegg, J. E. McPeak, B. Naydenov, J. Anders, K. Lips, Rapid-scan electron paramagnetic resonance using an epr-on-a-chip sensor, Magnetic Resonance 2 (2) (2021) 673–687.

[156] J. D. Cressler, On the potential of sige hbts for extreme environment electronics, Proceedings of the IEEE 93 (9) (2005) 1559–1582.

[157] P. Kinget, Amplitude detection inside cmos lc oscillators, in: 2006 IEEE International Symposium on Circuits and Systems, IEEE, 2006, pp. 4–pp.

[158] A. Chu, B. Schlecker, J. Handwerker, S. Künstner, M. Ortmanns, K. Lips, J. Anders, Vco-based esr-on-a-chip as a tool for low-cost, high-sensitivity food quality control, in: 2017 IEEE Biomedical Circuits and Systems Conference (BioCAS), IEEE, 2017, pp. 1–4.

[159] A. Chu, B. Schlecker, M. Kern, J. L. Goodsell, A. Angerhofer, K. Lips, J. Anders, On the modeling of amplitude-sensitive esr detection using vco-based esr-on-a-chip detectors, Magnetic Resonance Discussions 2021 (2021) 1–19.

[160] C. Calvo, The differential-signal advantage for communications system design (2010). URL https://www.eetimes.com/The-differential-signal-advantage-for-communications-system-design

[161] J. W. Rogers, C. Plett, Radio frequency integrated circuit design, Artech House, 2010.

[162] T. Maly, T. Prisner, Relaxation filtered hyperfine spectroscopy (refine), Journal of Magnetic Resonance 170 (1) (2004) 88–96.

[163] L. R. Becerra, G. J. Gerfen, R. J. Temkin, D. J. Singel, R. G. Griffin, Dynamic nuclear polarization with a cyclotron resonance maser at 5 t, Physical Review Letters 71 (21) (1993) 3561.

[164] T. V. Can, M. A. Caporini, F. Mentink-Vigier, B. Corzilius, J. J. Walish, M. Rosay, W. E. Maas, M. Baldus, S. Vega, T. M. Swager, et al., Overhauser effects in insulating solids, The Journal of chemical physics 141 (6) (2014) 064202.

[165] D. Singel, H. Seidel, R. Kendrick, C. Yannoni, A spectrometer for epr, dnp, and multinuclear high-resolution nmr, Journal of Magnetic Resonance (1969) 81 (1) (1989) 145–161.

[166] S. J. Inati, Dynamic nuclear polarization and electron spin resonance in paramagnetic solids at high field, Ph.D. thesis, Massachusetts Institute of Technology (1999).

[167] A. Beaumont, D. Giloteaux, A. V. Matheoud, M. Buzio, G. Boero, Electron paramagnetic resonance magnetic field sensors for particle accelerators, Review of Scientific Instruments 91 (10) (2020) 105001.

[168] M. Lelli, S. R. Chaudhari, D. Gajan, G. Casano, A. J. Rossini, O. Ouari, P. Tordo, A. Lesage, L. Emsley, Solid-state dynamic nuclear polarization at 9.4 and 18.8 t from 100 k to room temperature, Journal of the American Chemical Society 137 (46) (2015) 14558–14561.

Bibliography

[169] A. V. Matheoud, N. S. Solmaz, G. Boero, A low-power microwave hemt *lc* oscillator operating down to 1.4 k, IEEE Transactions on Microwave Theory and Techniques 67 (7) (2019) 2782–2792.

[170] N. Sahin-Solmaz, A. V. Matheoud, G. Boero, A low power 35 ghz hemt oscillator for electron spin resonance spectroscopy, in: 2021 IEEE Radio Frequency Integrated Circuits Symposium (RFIC), IEEE, 2021, pp. 19–22.

[171] A. Schweiger, G. Jeschke, Principles of pulse electron paramagnetic resonance, Oxford University Press on Demand, 2001.

[172] C. P. Poole, Electron spin resonance: a comprehensive treatise on experimental techniques, Courier Corporation, 1996.

[173] J. A. Weil, J. R. Bolton, Electron paramagnetic resonance: elementary theory and practical applications, John Wiley & Sons, 2007.

[174] J. A. Del Alamo, Nanometre-scale electronics with III–V compound semiconductors, Nature 479 (7373) (2011) 317.

[175] T. Takahashi, Y. Kawano, K. Makiyama, S. Shiba, M. Sato, Y. Nakasha, N. Hara, Maximum frequency of oscillation of 1.3 THz obtained by using an extended drain-side recess structure in 75-nm-gate InAlAs/InGaAs high-electron-mobility transistors, Appl. Phys. Express 10 (2) (2017) 024102.

[176] A. H. Akgiray, S. Weinreb, R. Leblanc, M. Renvoise, P. Frijlink, R. Lai, S. Sarkozy, Noise measurements of discrete hemt transistors and application to wideband very low-noise amplifiers, IEEE Transactions on Microwave Theory and Techniques 61 (9) (2013) 3285–3297.

[177] J. Ajayan, D. Nirmal, T. Ravichandran, P. Mohankumar, P. Prajoon, L. Arivazhagan, C. K. Sarkar, InP high electron mobility transistors for submillimetre wave and terahertz frequency applications: A review, Int. J. Electron. Commun. (Jul. 2018).

[178] J. Schleeh, G. Alestig, J. Halonen, A. Malmros, B. Nilsson, P. Nilsson, J. Starski, N. Wadefalk, H. Zirath, J. Grahn, Ultralow-power cryogenic InP HEMT with minimum noise temperature of 1 K at 6 GHz, IEEE Electron Devices Lett. 33 (5) (2012) 664–666.

[179] S. Montazeri, W.-T. Wong, A. Coskun, J. Bardin, Ultra-low-power cryogenic SiGe low-noise amplifiers: Theory and demonstration, IEEE Trans. Microw. Theory Techn. 64 (1) (2016) 178–187.

[180] J. Hornibrook, J. Colless, I. Lamb, S. Pauka, H. Lu, A. Gossard, J. Watson, G. Gardner, S. Fallahi, M. Manfra, Cryogenic control architecture for large-scale quantum computing, Phys. Rev. App. 3 (2) (2015) 024010.

[181] N. Oukhanski, M. Grajcar, E. Ilichev, H.-G. Meyer, Low noise, low power consumption high electron mobility transistors amplifier, for temperatures below 1 K, Rev. Sci. Instrum. 74 (2) (2003) 1145–1146.

[182] A. Korolev, V. Shnyrkov, V. Shulga, Note: Ultra-high frequency ultra-low dc power consumption HEMT amplifier for quantum measurements in millikelvin temperature range, Rev. Sci. Instrum. 82 (1) (2011) 016101.

[183] A. Korolev, V. Shulga, I. Gritsenko, G. Sheshin, PHEMT as a circuit element for high impedance nanopower amplifiers for ultra-low temperatures application, Cryogenics 67 (1) (2015) 31–35.

[184] L. A. Tracy, D. R. Luhman, S. M. Carr, N. C. Bishop, G. A. Ten Eyck, T. Pluym, J. R. Wendt, M. P. Lilly, M. S. Carroll, Single shot spin readout using a cryogenic high-electron-mobility transistor amplifier at sub-Kelvin temperatures, Appl. Phys. Lett. 108 (6) (2016) 063101.

[185] I. Vink, T. Nooitgedagt, R. Schouten, L. Vandersypen, W. Wegscheider, Cryogenic amplifier for fast real-time detection of single-electron tunneling, Appl. Phys. Lett. 91 (12) (2007) 123512.

[186] B. Patra, R. M. Incandela, J. P. Van Dijk, H. A. Homulle, L. Song, M. Shahmohammadi, R. B. Staszewski, A. Vladimirescu, M. Babaie, F. Sebastiano, et al., Cryo-CMOS circuits and systems for quantum computing applications, IEEE J. Solid-State Circuits 53 (1) (2018) 309–321.

[187] C. Wang, T. Hanrahan, M. Johnson, High capacity closed-cycle 1 K cryocooler, Cryogenics 95 (1) (2018) 64–68.

[188] C. Chiong, H. Chen, J. Kao, H. Wang, M. Chen, 180-220 GHz MMIC Amplifier using 70-nm GaAs MHEMT Technology, IEEE Int. Symp. RFIT (Aug. 2016).

[189] P. Altuntas, N. Defrance, M. Lesecq, A. Agboton, R. Ouhachi, E. Okada, C. Gaquiere, J.-C. De Jaeger, E. Frayssinet, Y. Cordier, On the correlation between kink effect and effective mobility in InAlN/GaN HEMTs, in: 9th Eur. Microw. Integr. Circuit Conf., 2014, pp. 88–91.

[190] H. Shichman, D. A. Hodges, Modeling and simulation of insulated-gate field-effect transistor switching circuits, IEEE J. Solid-State Circuits 3 (3) (1968) 285–289.

[191] K. R. Laker, W. M. Sansen, Design of analog integrated circuits and systems, McGraw-Hill New York, 1994.

[192] P. Antognetti, G. Massobrio, Semiconductor device modeling with SPICE, McGraw-Hill, Inc., 1990.

Bibliography

[193] A. Ortiz-Conde, F. G. Sánchez, J. J. Liou, A. Cerdeira, M. Estrada, Y. Yue, A review of recent MOSFET threshold voltage extraction methods, Microelectronics Reliability 42 (4-5) (2002) 583–596.

[194] R. Incandela, L. Song, H. Homulle, E. Charbon, A. Vladimirescu, F. Sebastiano, Characterization and compact modeling of nanometer CMOS transistors at deep-cryogenic temperatures, IEEE J. Electron Devices Soc. 6 (2018) 996–1006.

[195] C. Lin, W. Wang, P. Lin, C. Lin, Y. Chang, Y. Chan, Transient pulsed analysis on GaN HEMTs at cryogenic temperatures, IEEE Electron Devices Lett. 26 (10) (2005) 710–712.

[196] S. Hong, G. Choi, R. Baek, H. Kang, S. Jung, Y. Jeong, Low-temperature performance of nanoscale MOSFET for deep-space RF applications, IEEE Electron Device Lett. 29 (7) (2008) 775–777.

[197] C.-S. Chang, H. Fetterman, C. Viswanathan, The characterization of high electron mobility transistors using Shubnikov–de Haas oscillations and geometrical magnetoresistance measurements, J. Appl. Phys. 66 (2) (1989) 928–936.

[198] R. Popovic, Hall effect devices - Magnetic sensors and characterization of semiconductors, Adam-Hilger, 1991.

[199] T. Jervis, E. Johnson, Geometrical magnetoresistance and Hall mobility in Gunn effect devices, Solid-State Electr. 13 (2) (1970) 181–189.

[200] P. Dimitropoulos, P. Drljaca, R. Popovic, P. Chatzinikolaou, Horizontal Hall devices: A lumped-circuit model for EDA simulators, Sens. Actuator A-Phys. 145 (1) (2008) 161–175.

[201] M. Mishra, R. Sharma, R. Manchanda, R. Bag, O. Thakur, R. Muralidharan, Comprehensive magnetotransport characterization of two dimensional electron gas in AlGaN/GaN high electron mobility transistor structures leading to the assessment of interface roughness, AIP Advances 4 (9) (2014) 097124.

[202] M. Arikan, A. Straw, N. Balkan, Warm electron energy loss in GaInAs/AlInAs high electron mobility transistor structures, J. Appl. Phys. 74 (10) (1993) 6261–6265.

[203] Z. Tan, C. Tan, L. Ma, G. Liu, L. Lu, C. Yang, Shubnikov-de Haas oscillations of a single layer graphene under dc current bias, Phys. Rev. B 84 (11) (2011) 115429.

[204] E. Tiras, O. Celik, S. Mutlu, S. Ardali, S. Lisesivdin, E. Ozbay, Temperature dependent energy relaxation time in AlGaN/AlN/GaN heterostructures, Superlattices and Microstruct. 51 (6) (2012) 733–744.

[205] J. Campbell, K. Cheung, L. Yu, J. Suehle, A. Oates, K. Sheng, Geometric magnetoresistance mobility extraction in highly scaled transistors, IEEE Electron Devices Lett. 32 (1) (2011) 75–77.

[206] O. Momeni, E. Afshari, High power terahertz and millimeter-wave oscillator design: A systematic approach, IEEE J. Solid-State Circuits 46 (3) (2011) 583–597.

[207] Y. Nakasha, S. Masuda, K. Makiyama, T. Ohki, M. Kanamura, N. Okamoto, T. Tajima, T. Seino, H. Shigematsu, K. Imanishi, et al., E-band 85-mW oscillator and 1.3-W amplifier ICs using 0.12 μm GaN HEMTs for millimeter-wave transceivers, in: IEEE Comp. Semicon. Int. Circuit Symp. (CSICS), 2010, pp. 1–4.

[208] Y. Kwon, D. Pavlidis, Large signal analysis and experimental characteristics of monolithic InP-based W-band HEMT oscillators, in: Proc. 21st Eur. Microw. Conf., Vol. 1, 1991, pp. 161–166.

[209] V. S. Kaper, V. Tilak, H. Kim, A. V. Vertiatchikh, R. M. Thompson, T. R. Prunty, L. F. Eastman, J. R. Shealy, High-power monolithic AlGaN/GaN HEMT oscillator, IEEE J. Solid-State Circuits 38 (9) (2003) 1457–1461.

[210] P. Burasa, N. G. Constantin, K. Wu, Low-power injection-locked zero-IF self-oscillating mixer for high Gbit/s data-rate battery-free Active μRFID tag at millimeter-wave frequencies in 65-nm CMOS, IEEE Trans. Microw. Theory Techn. 64 (4) (2016) 1055–1065.

[211] S.-L. Jang, Y.-C. Lin, Low-power three-path inductor class-C VCO without any dynamic bias circuit, Electron. Lett. 53 (17) (2017) 1186–1188.

[212] W.-S. Feng, C. Yeh, C.-M. Tsao, H.-H. Li, P. Chatterjee, C.-H. Chen, Low power design for RF circuits, in: Proc. Cross Strait Quad-Regional Radio Sci. Wireless Techn. Conf. (CSQRWC), Vol. 1, 2011, pp. 657–660.

[213] M. Motoyoshi, S. Kameda, N. Suematsu, 57 GHz 130 μW CMOS millimeter-wave oscillator for ultra low power sensor node, in: 11th Global Symp. Millimeter Waves (GSMM), 2018, pp. 1–4.

[214] S.-L. Jang, C.-F. Lee, A low voltage and power *LC* VCO implemented with dynamic threshold voltage MOSFETS, IEEE Microw. Wireless Compon. Lett. 17 (5) (2007) 376–378.

[215] D. Fathi, A. G. Nejad, Ultra-low power, low phase noise 10 GHz LC VCO in the subthreshold regime, Circuits and Systems 4 (04) (2013) 350.

[216] F. Yu, A low-voltage and low-power 3-GHz CMOS LC VCO for S-band wireless applications, Wirel. Pers. Commun. 78 (2) (2014) 905–914.

[217] B. Li, Y. Zhai, B. Yang, T. Salter, M. Peckerar, N. Goldsman, Ultra low power phase detector and phase-locked loop designs and their application as a receiver, Microelectron. J. 42 (2) (2011) 358–364.

[218] W. Xiushan, W. Zhigong, L. Zhiqun, X. Jun, L. Qing, Design and realization of an ultra-low-power low-phase-noise CMOS LC-VCO, J. Semicond. 31 (8) (2010) 085007.

Bibliography

[219] S.-L. Jang, Y.-J. Su, K. J. Lin, B.-J. Wang, An 4.7 ghz low-power cross-coupled gan hemt oscillator, Microw. Optical Techn. Lett. 60 (10) (2018) 2442–2447.

[220] A. Hollmann, D. Jirovec, M. Kucharski, D. Kissinger, G. Fischer, L. R. Schreiber, 30 GHz-voltage controlled oscillator operating at 4 K, arXiv preprint arXiv:1804.09522 (Apr. 2018).

[221] R. Kojouharov, I. Angelov, E. Kollberg, Z. Ivanov, Y. F. Chen, T. Claeson, L. Yohansson, An X-band HEMT microwave oscillator stabilized with a superconducting resonator, Supercond. Sci. Technol. 10 (1) (1997) 71.

[222] E. Vollmer, P. Gutmann, X-band GaAs MESFET oscillator for cryogenic application at 4.2 K, Electron. Lett. 27 (24) (1991) 2210–2211.

[223] A. V. Matheoud, G. Gualco, M. Jeong, I. Zivkovic, J. Brugger, H. M. Rønnow, J. Anders, G. Boero, Single-Chip spin resonance detectors operating at 50 GHz, 92 GHz, and 146 GHz, J. Magn. Reson. 278 (2017) 113–121.

[224] J. Anders, A. Angerhofer, G. Boero, K-band single-chip electron spin resonance detector, J. Magn. Reson. 217 (2012) 19–26.

[225] G. Boero, G. Gualco, R. Lisowski, J. Anders, D. Suter, J. Brugger, Room temperature strong coupling between a microwave oscillator and an ensemble of electron spins, J. Magn. Reson. 231 (2013) 133–140.

[226] T. Yalcin, G. Boero, Single-chip detector for electron spin resonance spectroscopy, Rev. Sci. Instrum. 79 (2008) 094105.

[227] G. Gualco, J. Anders, A. Sienkiewicz, S. Alberti, L. Forro, G. Boero, Cryogenic single-chip electron spin resonance detector, J. Magn. Reson. 247 (2014) 96–103.

[228] A. Hajimiri, T. Lee, A general theory of phase noise in electrical oscillators, IEEE J. Solid-State Circuits 33 (2) (1998) 179–194.

[229] B. Razavi, RF microelectronics, 2nd, international ed., Pearson Education International, Upper Saddle River, NJ, 2012.

[230] V. J. Urick, K. J. Williams, J. D. McKinney, Fundamentals of microwave photonics, Vol. 1, John Wiley & Sons, 2015.

[231] H. Nyquist, Thermal agitation of electric charge in conductors, Phys. Rev. 32 (1) (1928) 110–113.

[232] A. A. Clerk, M. H. Devoret, S. M. Girvin, F. Marquardt, R. J. Schoelkopf, Introduction to quantum noise, measurement, and amplification, Rev. Mod. Phys. 82 (2) (2010) 1155.

[233] A. R. Kerr, Suggestions for revised definitions of noise quantities, including quantum effects, IEEE Trans. Microw. Theory Techn. 47 (3) (1999) 325–329.

[234] M. Castellanos-Beltran, K. Irwin, G. Hilton, L. Vale, K. Lehnert, Amplification and squeezing of quantum noise with a tunable Josephson metamaterial, Nature Physics 4 (12) (2008) 929.

[235] L. B. Kish, G. A. Niklasson, C. G. Granqvist, Zero-point term and quantum effects in the Johnson noise of resistors: a critical appraisal, J. Stat. Mech. Theory Exp. 2016 (5) (2016) 054006.

[236] P. Baltus, A. Wagemans, R. Dekker, A. Hoogstraate, H. Maas, A. Tombeur, J. Van Sinderen, A 3.5-mw, 2.5-ghz diversity receiver and a 1.2-mw, 3.6-ghz vco in silicon on anything, IEEE J. Solid-State Circuits 33 (12) (1998) 2074–2079.

[237] W. Duffy Jr, J. F. Dubach, P. A. Pianetta, J. F. Deck, D. L. Strandburg, A. R. Miedema, Antiferromagnetic linear chains in the crystalline free radical BDPA, The Journal of Chemical Physics 56 (6) (1972) 2555–2561.

[238] J. Anders, M. Ortmanns, G. Boero, Noise in frequency-sensitive esr detectors, IFAC Proceedings Volumes 45 (2) (2012) 451–456.

[239] G. Boero, G. Gualco, R. Lisowski, J. Anders, D. Suter, J. Brugger, Room temperature strong coupling between a microwave oscillator and an ensemble of electron spins, Journal of Magnetic Resonance 231 (2013) 133–140.

[240] F. M. Gardner, Phaselock techniques, John Wiley & Sons, 2005.

[241] J. Baylon, P. Agarwal, L. Renaud, S. N. Ali, D. Heo, A Ka-band dual-band digitally controlled oscillator with 195.1-dBc/Hz FoM_T based on a compact high Q dual-path phase-switched inductor, IEEE Transactions on Microwave Theory and Techniques 67 (7) (2019) 2748–2758.

[242] C.-H. Lin, Y.-T. Lu, H.-Y. Liao, S. Chen, A. L. Loke, T.-J. Yeh, A 0.011-mm^2 27.5-GHz VCO with transformer-coupled bandpass filter achieving-191 dBc/Hz FoM in 16-nm FinFET CMOS, in: 2020 IEEE/MTT-S International Microwave Symposium (IMS), IEEE, 2020, pp. 353–356.

[243] Y. Shu, H. J. Qian, X. Luo, A 2-D mode-switching quad-core oscillator using EM mixed-coupling resonance boosting, IEEE Journal of Solid-State Circuits (2020).

[244] N. Jahan, C. Baichuan, A. Barakat, R. K. Pokharel, Utilization of multi-resonant defected ground structure resonators in the oscillator feedback for phase noise reduction of K-Band VCOs in 0.18 um CMOS technology, IEEE Transactions on Circuits and Systems I: Regular Papers 67 (4) (2020) 1115–1125.

[245] Y.-S. Lin, T.-H. Chang, C.-Z. Chen, C.-C. Chen, H.-Y. Yang, S. S. Wong, Low-power 48-GHz CMOS VCO and 60-GHz CMOS LNA for 60-GHz dual-conversion receiver, in: 2009 International Symposium on VLSI Design, Automation and Test, IEEE, 2009, pp. 88–91.

[246] Y. Huang, Y. Chen, H. Guo, P.-I. Mak, R. P. Martins, A 3.3-mW 25.2-to-29.4-GHz current-reuse VCO using a single-turn multi-tap inductor and differential-only switched-capacitor arrays with a 187.6-dBc/Hz FOM, IEEE Transactions on Circuits and Systems I: Regular Papers 67 (11) (2020) 3704–3717.

[247] P. Zhou, J. Chen, P. Yan, Z. Chen, D. Hou, W. Hong, A 273.5–312-ghz signal source with 2.3 dbm peak output power in a 130-nm sige bicmos process, IEEE Transactions on Terahertz Science and Technology 10 (3) (2020) 260–270.

[248] B. Razavi, A 300-GHz fundamental oscillator in 65-nm CMOS technology, IEEE J. Solid-State Circuits 46 (4) (2011) 894–903.

[249] L. Marti, N. Solmaz, M. A. Urban, C. P. B. Bus, A. Pappas, N. Lehmann, A. Dapp, R. Gunzenhauser, N. H. Alaniva, M. Frimmer, G. Boero, D. Klose, G. Jenschke, L. Novotny, A. Barnes, Design and development of optical magic angle spinning, in: XXIV Swiss NMR Symposium Book of Abstracts, 2022, p. 25.

[250] M. Grisi, F. Vincent, B. Volpe, R. Guidetti, N. Harris, A. Beck, G. Boero, Nmr spectroscopy of single sub-nl ova with inductive ultra-compact single-chip probes, Scientific reports 7 (1) (2017) 1–8.

[251] G. Sivelli, G. M. Conley, C. Herrera, K. Marable, K. J. Rodriguez, H. Bollwein, M. J. Sudano, J. Brugger, A. J. Simpson, G. Boero, et al., Nmr spectroscopy of a single mammalian embryo, bioRxiv (2021) 2021–07.

[252] E. Montinaro, M. Grisi, M. Letizia, L. Pethö, M. Gijs, R. Guidetti, J. Michler, J. Brugger, G. Boero, 3d printed microchannels for sub-nl nmr spectroscopy, PloS one 13 (5) (2018) e0192780.

[253] M. Grisi, E. Montinaro, F. Vincent, L. Pethö, M. C. Letizia, B. Volpe, N. Harris, A. Beck, R. Guidetti, M. Gijs, et al., Cmos and 3d printing for nmr spectroscopy at the single embryo scale, Chimia 73 (7) (2019) 635.

[254] U. Vool, M. Devoret, Introduction to quantum electromagnetic circuits, Int. J. Circ. Theor. App. 45 (7) (2017) 897–934.

[255] X. Gu, A. F. Kockum, A. Miranowicz, Y. xi Liu, F. Nori, Microwave photonics with superconducting quantum circuits, Phys. Rep. 718-719 (2017) 1 – 102.

Acknowledgements

I would like to thank many people for their invaluable contribution to my PhD and outside of EPFL life.

First of all, to Giovanni, I cannot find words that are enough to explain my gratitude towards him. He has helped me through many aspects of my life during these last five years. He has supported me not only everyday in my work but also in the hardest days of my life. He was always available and constantly teaching from the beginning where he explained the physical principals of many devices through Skype interviews to the last day of my thesis submission. His positive attitude in the lab where he would always say "We will understand" or "We will find a solution" was the most helpful when it looked like nothing will work. And the way he was so happy for me when we first saw the 200 GHz DNP signal... He is a true mentor in every aspect and I cannot thank him enough.

I would like to express my deepest appreciation to my thesis jury members Ileana-Cristina Benea-Chelmus, Sami Jannin, Donhee Ham, and Andrea Capozzi for their valuable time and insightful comments. I'm extremely grateful to Jürgen who managed our lab with care, created a positive lab atmosphere, shared his knowledge, and provided a security net to me when I really needed it. I would also like to extend my deepest gratitude to Lucie Auberson, Nicole Bouendin, and Séverine Eggli, our beloved secretaries, who always helped me. I also wish to thank Alan Vachoux and Alexander Levisse for their support in design kits and tape-outs.

I would like to thank Alessandro for introducing me to the lab environment, measurements, and instruments, and always telling me very fun stories :) Even though we spend only a few months as colleagues, it felt like years maybe because he continued to answer all my questions even after leaving EPFL. Reza has been an essential part of my studies in the last years. He was almost always available for me and extremely supportive in the most stressful periods of my PhD. We struggled through design discussions, tape-outs, and measurements, but also shared disco ball celebration moments. A special thank you for bonding my chips and fixing broken bondwires thousand times and at any time when we needed "urgent" measurements as we always do :)

Many thanks to my office mates Roberto and Mohammad for the many days we have shared

Personal Data

Name	Nergiz Şahin Solmaz
Date of birth	August 06, 1991
Place of birth	Samsun, Turkey

Education

2018-2023 PhD at École Polytechnique Fédérale de Lausanne, Lausanne, Switzerland
Topic: Single chip dynamic nuclear polarization microsystems

2015-2018 MSc in Electronics Engineering at Istanbul Technical University, Istanbul, Turkey
Topic: 0.18 µm CMOS X-BAND low noise amplifier for space applications

2011-2014 BSc in Control Engineering at Istanbul Technical University, Istanbul, Turkey
Topic: Controller design with peak observer method

2009-2014 BSc in Electronics Engineering at Istanbul Technical University, Istanbul, Turkey
Topic: 2.4 GHz 7-bit programmable frequency divider

Publications

Journal Papers

1 **Sahin Solmaz, N.**, Farsi, R., Boero, G., 200 GHz single chip dynamic nuclear polarization microsystem. *in preparation with the results reported in Chapter 3 of this PhD thesis.*

2 Farsi, R., **Sahin Solmaz, N.**, Khosropour, N., Jacinto, B., Giroud, F., Boero, G. (2023). 500 MHz high resolution proximity sensors with fully integrated digital counter. *Measurement, 217*, 113045.

3 Russo, R., Chatel, A., **Sahin Solmaz, N.**, Farsi, R., Furci, H., Brugger, J., & Boero, G. (2023). Fabrication and characterization of NbTi microwave superconducting resonators. *Micro and Nano Engineering*, 100203.

4 Clément, P., Ackermann, J., **Sahin Solmaz, N.**, Herbertz, S., Boero, G., Kruss, S., & Brugger, J. (2022). Comparison of electrical and optical transduction modes of DNA-wrapped SWCNT nanosensors for the reversible detection of neurotransmitters. *Biosensors and Bioelectronics*, *216*, 114642.

5 **Sahin Solmaz, N.**, Grisi, M., Matheoud, A. V., Gualco, G., & Boero, G. (2020). Single-chip dynamic nuclear polarization microsystem. *Analytical Chemistry*, *92*(14), 9782-9789.

6 Kabaoğlu, A., **Şahin Solmaz, N.**, İlik, S., Uzun, Y., & Yelten, M. B. (2019). Variability-aware cryogenic models of mosfets: validation and circuit design. *Semiconductor science and technology*, *34*(11), 115004.

7   İlik, S., Gencer, F. B., **Sahin Solmaz, N.**, Çağlar, A., & Yelten, M. B. (2019). Radiation tolerance impact of trap density near the drain and source regions of a MOSFET. *Nuclear Instruments and Methods in Physics Research Section B: Beam Interactions with Materials and Atoms*, *449*, 1-5.

8   Matheoud, A. V., **Sahin Solmaz, N.**, & Boero, G. (2019). A Low-Power Microwave HEMT LC Oscillator Operating Down to 1.4 K. *IEEE Transactions on Microwave Theory and Techniques*, *67*(7), 2782-2792.

9   Matheoud, A. V., **Sahin Solmaz, N.**, Frehner, L., & Boero, G. (2019). Microwave inductive proximity sensors with sub-pm/Hz$^{1/2}$ resolution. *Sensors and Actuators A: Physical*, *295*, 259-265.

10 Kabaoğlu, A., **Sahin Solmaz, N.**, İlik, S., Uzun, Y., & Yelten, M. B. (2018). Statistical MOSFET modeling methodology for cryogenic conditions. *IEEE Transactions on Electron Devices*, *66*(1), 66-72.

11 Matheoud, A. V., **Sahin, N.**, & Boero, G. (2018). A single chip electron spin resonance detector based on a single high electron mobility transistor. *Journal of Magnetic Resonance*, *294*, 59-70.

Conference Proceedings

1   **Sahin Solmaz, N.**, Matheoud, A. V., & Boero, G. (2021, June). A Low Power 35 GHz HEMT Oscillator for Electron Spin Resonance Spectroscopy. In *2021 IEEE Radio Frequency Integrated Circuits Symposium (RFIC)* (pp. 19-22). IEEE.

2   İlık, S., **Sahin Solmaz, N.**, Kabaoğlu, A., & Yelten, M. B. (2019, July). Comparison of ELTs with different shapes and a regular layout transistor in 180 nm CMOS process. In *2019 16th International Conference on Synthesis, Modeling, Analysis and Simulation Methods and Applications to Circuit Design (SMACD)* (pp. 21-24). IEEE.

3   **Sahin, N.**, & Yelten, M. B. (2017, September). A 0.18 µm CMOS X-Band Low Noise Amplifier for Space Applications. In *2017 New Generation of CAS (NGCAS)* (pp. 205-208). IEEE.

Conference Presentation

1   Oral presentation at *ENC 2023*. **Sahin Solmaz, N.**, Farsi, R., Boero, G., 200 GHz single chip dynamic nuclear polarization microsystem.

2   Poster presentation at *The 55th Annual International Meeting of the ESR Spectroscopy Group of the Royal Society of Chemistry 2022*, **Sahin Solmaz, N.**, Farsi, R., Boero, G., 175 GHz ESR detector for single chip DNP.

3   Oral presentation at *IEEE RFIC 2021*. **Sahin Solmaz, N.**, Matheoud, A. V., & Boero, G., A Low Power 35 GHz HEMT Oscillator for Electron Spin Resonance Spectroscopy.

4   Oral presentation at *EUROMAR 2020*. **Sahin Solmaz, N.**, Grisi, M., Matheoud, A. V., Gualco, G., & Boero, G., Single-chip dynamic nuclear polarization microsystem.